

ETH Zürich  
Master of Science ETH in Physics

---

# Search for decays of the 125 GeV Higgs boson into a photon and a $\phi$ , $\omega$ or $D^{*0}$ meson

---

## MASTER'S THESIS

**Author:**  
Martí Pedemonte Bernat

**Supervisors:**  
Prof. Dr. Günther Dissertori, ETH Zürich  
Prof. Dr. Christoph M. E. Paus, MIT  
Dr. Mariarosaria D'Alfonso, MIT

**Conducted at:**  
Particle Physics Collaboration, Massachusetts Institute of Technology

Cambridge MA, November 2023



Eidgenössische Technische Hochschule Zürich  
Swiss Federal Institute of Technology Zurich



Massachusetts  
Institute of  
Technology



# Acknowledgements

En primer lloc, m'agradaria agrair a tota la meva família el seu suport i la seva estima, no només durant el transcurs d'aquest projecte, sinó des que tinc memòria. Gràcies, Joan, Susanna, Ferran i Sara per estar sempre aquí al meu costat i motivar-me a treure el millor de mi.

Als amics de Sant Salvador, que tantes vegades us he avorrit i tantes vegades m'heu escoltat.

A tots els professors de l'escola i l'institut. A la Maria, la Maribel, en Juan Carlos, la Sagrario i en Jesús. Sense vosaltres mai hauria pres aquest camí, que estic tan satisfet d'haver recorregut.

A l'Íngrid i en Sergi, que després d'haver compartit moltes hores d'estudi, m'han aconsellat i animat durant tot el treball.

A la Blanca, la Marion, en Marc i en Toni, per tot el suport en els moments més complicats, i tot el que hem viscut i ens queda per viure junts.

To Andrea, for the countless discussions about Nature and the Universe at HIT and ASVZ.

To Etienne and Andrea, for the dinners and gatherings we have shared, and for making my stay here as joyful as I could have hoped.

To Günther, for granting me the opportunity to live the experience of a lifetime.

I would also like to thank the PPC group at CERN for their valuable feedback and comments on my presentations.

To all my friends from the office: Luca, Ludo, Pietro, Kyungseop, Julius, Chad and Zhangqier, thank you for the quality time we have spent together discussing physics, puzzles and Archi, and for your assistance when I needed it.

I want to thank Christoph for making this project possible. Thank you for all the coffee breaks, insights, and guidance you provided me.

Thank you, Mariarosaria. For the many hours invested, your patience, and expertise. For teaching me things I never thought I would understand. It has been a pleasure working alongside you. Thank you.

# Abstract

A search for the exclusive decays of the Higgs boson to a photon and either a  $\phi(1020)$ ,  $\omega(782)$  or  $D^*(2007)^0$  meson is presented. These decays have been suggested as a probe of the Higgs boson couplings to light quarks and as a test of potential deviations from the Standard Model prediction in these flavour interactions. The analysis is performed with a pp collision data sample corresponding to an integrated luminosity of  $39.54 \text{ fb}^{-1}$  collected at  $\sqrt{s} = 13 \text{ TeV}$  with the CMS detector at the Large Hadron Collider (LHC) in 2018 during Run 2. Four decay channels are explored:  $H \rightarrow \phi\gamma$  with further  $\phi \rightarrow \pi^+\pi^-\pi^0$ ,  $H \rightarrow \omega\gamma$  with further  $\omega \rightarrow \pi^+\pi^-\pi^0$ ,  $H \rightarrow D^{*0}\gamma$  with further  $D^{*0} \rightarrow D^0\pi^0/\gamma$ ,  $D^0 \rightarrow K^-\pi^+$  and  $H \rightarrow D^{*0}\gamma$  with further  $D^{*0} \rightarrow D^0\pi^0/\gamma$ ,  $D^0 \rightarrow K^-\pi^+\pi^0$ . Estimated upper limits at a 95% confidence level on the branching fractions of the four Higgs boson decay modes were obtained. These are  $2.40 \times 10^{-2}$ ,  $3.27 \times 10^{-3}$ ,  $6.50 \times 10^{-3}$  and  $1.29 \times 10^{-2}$ , respectively.

Aquesta tesi presenta un estudi sobre desintegracions del bosó de Higgs en un fotó i en un mesó  $\phi(1020)$ ,  $\omega(782)$  o  $D^*(2007)^0$ . Aquests decaïments han estat proposats com a mètode per mesurar les constants d'acoblament del bosó de Higgs amb els quarks lleugers i també com a prova de possibles desviacions en prediccions del model estàndard de física de partícules. L'anàlisi s'ha realitzat amb una mostra de dades de col·lisions protó-protó corresponent a una lluminositat integrada de  $39,54 \text{ fb}^{-1}$  recollida a  $\sqrt{s} = 13 \text{ TeV}$  amb el detector CMS al Gran Col·lisionador d'Hadrons (LHC) l'any 2018 durant la Run 2. S'han estudiat quatre canals de desintegració:  $H \rightarrow \phi\gamma$  amb posterior  $\phi \rightarrow \pi^+\pi^-\pi^0$ ,  $H \rightarrow \omega\gamma$  amb posterior  $\omega \rightarrow \pi^+\pi^-\pi^0$ ,  $H \rightarrow D^{*0}\gamma$  amb posterior  $D^{*0} \rightarrow D^0\pi^0/\gamma$ ,  $D^0 \rightarrow K^-\pi^+$  i  $H \rightarrow D^{*0}\gamma$  amb posterior  $D^{*0} \rightarrow D^0\pi^0/\gamma$ ,  $D^0 \rightarrow K^-\pi^+\pi^0$ . S'han obtingut estimacions dels límits superiors de les fraccions de desintegració per als quatre modes estudiats amb un nivell de confiança del 95%. Aquests són  $2.40 \times 10^{-2}$ ,  $3.27 \times 10^{-3}$ ,  $6.50 \times 10^{-3}$  i  $1.29 \times 10^{-2}$ , respectivament.

# Contents

|  |            |
|--|------------|
| <b>Introduction</b>  | <b>iii</b> |
| <b>1 Theory and Motivation</b>                                   | <b>1</b>   |
| 1.1 The Standard Model . . . . .                                 | 1          |
| 1.2 The Higgs boson . . . . .                                    | 7          |
| 1.2.1 Properties of the Higgs boson . . . . .                    | 7          |
| 1.2.2 Main production modes of the Higgs boson . . . . .         | 8          |
| 1.2.3 Main decay channels of the Higgs boson . . . . .           | 10         |
| 1.3 The Search for a model beyond the SM . . . . .               | 13         |
| <b>2 The CMS at the LHC</b>                                      | <b>18</b>  |
| 2.1 The Large Hadron Collider at CERN . . . . .                  | 18         |
| 2.2 The Compact Muon Solenoid . . . . .                          | 20         |
| 2.3 The discovery of the Higgs boson . . . . .                   | 24         |
| <b>3 Search for exclusive hadronic decays of the Higgs boson</b> | <b>26</b>  |
| 3.1 Analysis overview . . . . .                                  | 26         |
| 3.2 Samples and triggers . . . . .                               | 27         |
| 3.2.1 Data and triggers . . . . .                                | 28         |
| 3.2.2 Background simulation . . . . .                            | 28         |
| 3.2.3 Signal simulation . . . . .                                | 28         |
| 3.3 Object definitions . . . . .                                 | 29         |
| 3.3.1 Primary vertex . . . . .                                   | 29         |
| 3.3.2 Photons . . . . .  | 30         |
| 3.4 Meson reconstruction . . . . .                               | 30         |
| 3.4.1 Track selection . . . . .                                  | 31         |
| 3.4.2 Meson decay vertex . . . . .                               | 31         |
| 3.4.3 Isolation . . . . .  | 31         |
| 3.4.4 Photons from the neutral particle decays . . . . .         | 31         |
| 3.4.5 Ditrack mass hypothesis . . . . .                          | 32         |
| 3.4.6 Meson mass hypothesis . . . . .                            | 33         |
| 3.4.7 Full meson transverse momentum . . . . .                   | 34         |
| 3.4.8 Meson momentum regression . . . . .                        | 36         |
| 3.4.9 Meson selection criteria . . . . .                         | 41         |
| 3.5 Event selection . . . . .                                    | 42         |

|       |   |           |
|-------|---|-----------|
| 3.6   | MC-data comparison . . . . .              | 43        |
| 3.7   | Signal and background modelling . . . . . | 51        |
| 3.7.1 | Signal modelling . . . . .                | 52        |
| 3.7.2 | Background modelling . . . . .            | 54        |
| 3.8   | Estimated results . . . . .               | 60        |
| 3.9   | Future potential improvements . . . . .   | 62        |
|       | <b>Conclusions</b>                        | <b>65</b> |
|       | <b>Appendix</b>                           | <b>66</b> |
|       | <b>References</b>                         | <b>67</b> |

# Introduction

The ambition to comprehend and model the world is inherent to the human condition. In this pursuit, mathematical language has proven to be an invaluable tool, serving as the basis for any physical theory aiming to predict the outcome of a particular process. These physical theories have been refined, expanded, and perfected over the years. Today, there is a suggested theory seeking to predict and understand nearly every physical process.

However, at the end of the nineteenth century, some scientists believed that all known physical theories were sufficient to describe nature. As Lord Kelvin famously stated:

*“There is nothing new to be discovered in physics now. All that remains is more and more precise measurement.”*

– Lord Kelvin (1901)

As we know today, he could not have been more wrong, as the last century has been the most scientifically successful in all history. Notable examples of these successful theories are Quantum Mechanics (QM) and the Standard Model of Particle Physics (SM), the latter aiming to explain the behaviour of the most fundamental particles that are thought to constitute all matter.

Quantum Mechanics, born in the early decades of the last century, aimed to explain the wave-particle duality for light, among other observed and unexplained phenomena, like the photoelectric effect. Scientists like Max Planck, Albert Einstein, Erwin Schrödinger and Paul Dirac, along with many other brilliant minds, developed a theory capable of explaining the intricacies of the interaction between particles of light, photons, and matter particles. Quantum Mechanics was subsequently followed by Quantum Field Theory (QFT) when the idea of quantizing the electromagnetic field emerged in the late 1920s. QFT combined three major themes of modern physics: quantum mechanics, the field concept, and the principle of relativity. This set of theories gave rise to quantum electrodynamics (QED) in the 1950s, and its success and predictive power led to efforts to apply the same basic concepts to the other forces of nature. By the late 1970s, these efforts successfully crystallized into the modern Standard Model of Particle Physics, explaining both the strong and electroweak nuclear forces with a single theory. For further details on QFT, QED and the Standard Model, refer to Refs. [1–3].

The Standard Model assumed certain symmetries in nature, under which the laws of physics remain unchanged. Formally, these symmetry transformations form a group, called gauge symmetry group. The underlying gauge symmetry group governing the SM not only predicted three massive vector bosons — the  $W^\pm$  and the  $Z^0$ , proposed in 1968 by Sheldon Glashow, Steven Weinberg, Abdus Salam, and other scientists [4–6] —, but also a massive

scalar boson, named after Peter Higgs who, along with Robert Brout, François Englert, Gerald Guralnik, C. R. Hagen, and Tom Kibble, proposed it to explain how all massive particles acquire mass [7–9].

Only fifteen years after the prediction of the massive gauge vector bosons, in 1983, the  $W^\pm$  and  $Z^0$  bosons were discovered at CERN by the UA1 and UA2 collaborations [10, 11], establishing the SM as a successful theory combining the weak and electromagnetic interactions. However, the Standard Model was incomplete without the Higgs boson, yet there was no sign of its existence.

Thirty more years of work and technology development were necessary until, on July 4<sup>th</sup>, 2012, the final piece of the puzzle fell into place. On that day, the CMS and ATLAS collaborations jointly announced the discovery of the Higgs boson at CERN’s Large Hadron Collider (LHC) [12, 13]. Although a reassuring finding, this did not consolidate the SM as the ultimate, immutable theory but marked the beginning of understanding the properties of this newly discovered particle and an opportunity to test the SM to its limits.

One of the predictions of the Standard Model is that the Higgs boson interacts with massive particles with a strength related to the particle’s mass. This has been successfully tested with remarkable accuracy for heavy particles: the gauge vector bosons  $W^\pm$  and  $Z^0$ , the heavy members of the third family of fermions (top and bottom quarks, and the tau lepton, but not the neutrino), and even the second-generation muon lepton [14]. However, measuring this coupling becomes increasingly challenging as the particle becomes lighter, as it is less likely to interact with the Higgs boson. Testing the SM hypothesis for less massive particles could reveal discrepancies between the theory and experiments, hinting at new physics beyond the SM (BSM), such as the existence of new particles and processes not previously considered.

Currently, the couplings of light quarks — including up, down, charm and strange — to the Higgs boson are not well-constrained due to limited data on the Higgs boson’s total decay width, which is the rate at which the Higgs boson decays. The presence of a large multi-jet background at the LHC makes it challenging to study these couplings using inclusive Higgs decays into quark-antiquark pairs. To address this, rare exclusive decays of the Higgs boson into a light meson and a photon have been suggested. These exclusive decays serve as a valuable tool for investigating both flavor-conserving and flavor-violating Higgs boson couplings to light quarks. The ATLAS and CMS collaborations have made initial attempts to set upper limits on these hadronic two-body Higgs boson decays, including processes like  $H \rightarrow J/\psi + \gamma$  [15, 16],  $H \rightarrow \rho, \phi, \omega, K^{*0} + \gamma$  [17, 18], and  $H \rightarrow J/\psi, \rho, \phi + Z^0$  [19, 20].

The analysis presented in this Master’s Thesis ultimately aims to constrain the Higgs coupling constants by studying four exotic decays of the Higgs boson into a photon and a light vector meson, where the vector meson decays into a pair of charged scalar mesons along with neutral particles, specifically either pions or photons. It uses data from proton-proton collisions corresponding to an integrated luminosity of  $39.54 \text{ fb}^{-1}$  at  $\sqrt{s} = 13 \text{ TeV}$ , collected by the CMS detector at the LHC in 2018 during Run 2. The final states of interest consist of an isolated and energetic photon, a charged meson pair, and photons compatible with a third (and sometimes fourth) neutral meson. The mesons considered here are a  $\phi$ , a  $\omega$  and a  $D^{*0}$ , each further decaying into two charged particles and a third (and fourth) neutral one:

$$\begin{aligned}
H \rightarrow \phi\gamma, & \quad \phi \rightarrow \pi^+\pi^-\pi^0 \\
H \rightarrow \omega\gamma, & \quad \omega \rightarrow \pi^+\pi^-\pi^0 \\
H \rightarrow D^{*0}\gamma, & \quad D^{*0} \rightarrow D^0\pi^0/\gamma, D^0 \rightarrow K^-\pi^+ \\
H \rightarrow D^{*0}\gamma, & \quad D^{*0} \rightarrow D^0\pi^0/\gamma, D^0 \rightarrow K^-\pi^+\pi^0
\end{aligned}$$

This study aims to place an upper limit on the branching ratio of the four different Higgs boson rare decays under study. The large background at the LHC and the infrequent nature of the decays prevent an actual measurement of the decay rates, allowing only an upper bound to be computed. The expected upper limits are determined using simulated samples, not real data. This is a common practice in high-energy physics, where data can only be *unblinded* for actual measurements after completing the full analysis and ensuring the consistency of techniques.

Simpler decays of the same nature ( $H \rightarrow M + \gamma$ ) are currently being studied by the CMS collaboration. These decay channels are  $H \rightarrow \rho^0/\phi/K^{*0} + \gamma$ , but where the meson further decays only into a pair of charged scalar mesons. This analysis follows a similar approach, with a focus on reconstructing the additional neutral particles.

The thesis is structured as follows. The first chapter briefly presents the Standard Model of Particle Physics, with a special emphasis on the Higgs boson, its properties, and frequent production and decay modes. It also motivates the analysis, explaining in detail the decay channels under study and exploring how a significant discrepancy between the measurements of these decay modes and the SM predictions might lead to new physics beyond the SM.

Chapter 2 introduces CERN and its Large Hadron Collider, as well as the Compact Muon Solenoid (CMS) experiment. It covers CERN's most significant breakthroughs, with a particular emphasis on the discovery of the Higgs boson at the LHC in 2012 by the CMS and ATLAS collaborations.

Chapter 3 is entirely dedicated to the analysis. It begins with a general overview, followed by an explanation of the samples, triggers, and object definitions. A section discusses the meson reconstruction techniques, which are crucial to the analysis. It also covers the criteria used in event selection and provides a comparison between the simulated samples and real data of the most important kinematic variables, before explaining how the signal and background have been modelled. Finally, the expected upper limits of the branching ratio for each channel are presented. The chapter concludes by addressing the subsequent steps required before data unblinding, as well as suggesting ideas to improve the results.

The thesis ends with a summary and conclusions of the conducted study, along with an appendix containing supplemental technical analysis details.

# Chapter 1

## Theory and Motivation

This chapter aims to provide an overview of the Standard Model of Particle Physics (SM), with a specific focus on the important role played by the Higgs boson. It offers a brief introduction to the SM and its fundamental particles, discusses the Lagrangian that governs their behaviour, and explores their interactions represented by Feynman diagrams. Moreover, it will examine the characteristics of the Higgs boson — its properties, its most frequent production and decay modes, and the Yukawa couplings to the three different fermion families. Finally, the end of the chapter will concentrate on the decay channels subject to our analysis and explore how a significant discrepancy between the measurements of these decay modes and the SM predictions might lead to new physics beyond the SM.

### 1.1 The Standard Model

One of the traits that distinguishes humans from other life forms is our sense of curiosity. Since ancient times, we have been trying to explain what happens around us, enabling us to predict and potentially harness the laws of nature. An exceptional theory that has come very close to achieving this goal is the Standard Model of Particle Physics (SM). It stands as one of the most precise theories ever conceived by humanity, and is the most successful theory of particle physics to date [21]. The Standard Model serves as a theory capable of describing three of the four known fundamental forces in the Universe (electromagnetic, weak and strong forces, but not gravity). This is achieved by classifying a set of elementary particles and defining the interactions between them. Other more detailed summaries of the SM can be found in Refs. [1–3] among many others.

The SM is a quantum field theory (QFT) defined by an internal local  $SU(3)_C \times SU(2)_L \times U(1)_Y$  gauge symmetry. Each elementary particle has its corresponding field in the theory and is categorized as a fermion or a boson based on its spin (half-integer-spin particles are fermions, while integer-spin particles are bosons). There are twelve fermions organized into three families or generations of four members: a charged lepton (e.g., the electron), a neutral lepton (neutrino), an up-type quark, and a down-type quark. In addition, each particle has its own corresponding antiparticle. The SM particle content is summarized in Figure 1.

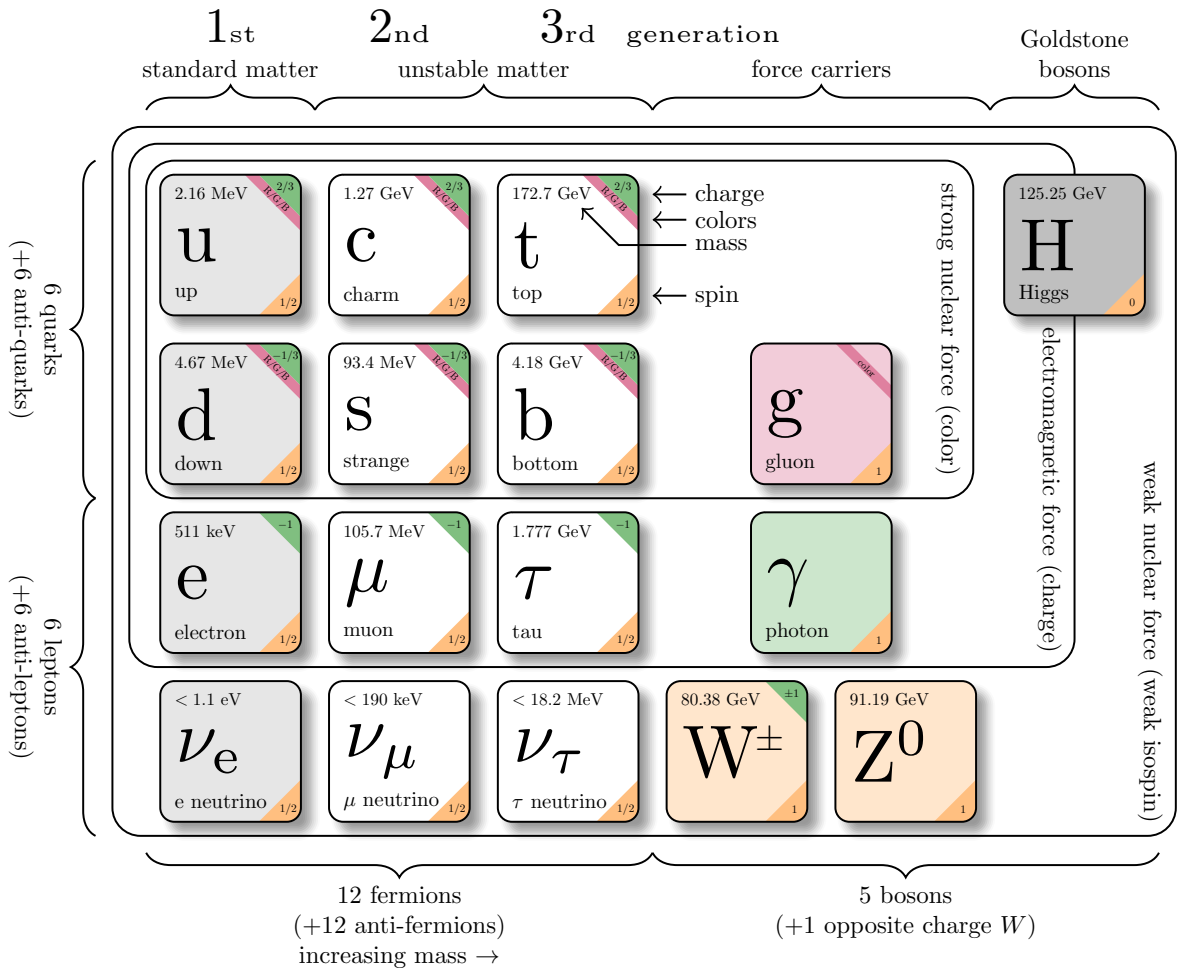


**Figure 1:** Elementary particles of the Standard Model. The electric charge, mass and spin of each particle are shown. Original figure from Ref. [22].

These three factors of the gauge symmetry group give rise to the three fundamental interactions between fermions, which are mediated by gauge bosons. To be precise, each generator of a local invariant gauge group induces a massless gauge boson. In the same way that in quantum electrodynamics (QED), the local gauge invariance of the theory under the  $U(1)$  group leads to the existence of a massless gauge field  $A_\mu$  (the photon field); in the SM, the process is analogous for each field.

The invariance of the SM under  $SU(3)_C$  postulates the existence of the gluon. More precisely, the eight generators of  $SU(3)_C$  introduce eight gluons that mediate the strong force between particles that possess colour charge (quarks and gluons). This is known as the quantum chromodynamics (QCD) sector of the Standard Model.

Similarly, the invariance of the second and third factors  $SU(2)_L \times U(1)_Y$  indicates the existence of the photon, the  $Z^0$  and the  $W^\pm$  bosons. In this case, unlike in QED or QCD, we cannot directly associate the photon with the generator of the hypercharge group  $U(1)_Y$  and the  $Z^0$ ,  $W^\pm$  bosons with the generators of the left weak isospin group  $SU(2)_L$ . Instead, the generators of  $SU(2)_L \times U(1)_Y$  give rise to four intermediate vector bosons ( $W_\mu^{1,2,3}$  for  $SU(2)_L$  and  $B_\mu$  for  $U(1)_Y$ ), which are then mixed through the weak mixing angle, or Weinberg angle,

$\theta_W$ , to produce the physical  $\gamma$  ( $A_\mu$ ),  $Z^0$ ,  $W^\pm$ . The physical bosons are then defined as:

$$W_\mu^\pm = \frac{1}{\sqrt{2}}(W_\mu^1 \mp iW_\mu^2)$$

$$\begin{pmatrix} A_\mu \\ Z_\mu^0 \end{pmatrix} = \begin{pmatrix} \cos \theta_W & \sin \theta_W \\ -\sin \theta_W & \cos \theta_W \end{pmatrix} \begin{pmatrix} B_\mu \\ W_\mu^3 \end{pmatrix}$$

By the definition of the groups  $SU(2)_L$  and  $U(1)_Y$ , the field  $W_\mu^{1,2,3}$  couples only to left-handed (negative helicity) particles, whereas the hypercharge field  $B_\mu$  couples to both left and right components with the same strength. Therefore, the intermediate boson mixing implies that  $W^\pm$  only couple to left-handed particles, but  $Z^0$  couples to both left and right-handed particles with different strengths, inducing (non-maximal) parity violation.

All gauge bosons that arise from the generators of gauge-invariant groups are expected to be massless; otherwise, the principle of local gauge invariance is spoiled, and the theory becomes unrenormalizable, leading to many divergences. Furthermore, this contradicts experimental observations, which confirm that the  $Z^0$  and  $W^\pm$  bosons are, in fact, massive. This breaking of gauge invariance when giving a mass to a particle is not restricted only to gauge bosons but also happens for fermions. In the SM, to allow for massive fields, all particles obtain their masses using spontaneous symmetry breaking (SSB) via the Brout-Englert-Higgs mechanism.

Spontaneous symmetry breaking is a fundamental principle of QFT used to explain how gauge bosons (and, in general, massive particles) can acquire non-vanishing mass while maintaining the theory gauge-invariant. This process describes systems where the Lagrangian obeys symmetries, but the lowest-energy vacuum solutions do not exhibit the same symmetries. In the case of the Higgs mechanism, it relies on the existence of an  $SU(2)$  doublet complex scalar field  $\phi$  with hypercharge  $Y = +1$ , which can be written as

$$\phi = \begin{pmatrix} \phi^+ \\ \phi^0 \end{pmatrix}$$

with  $(\phi^*)^* = \phi^-$  and  $(\phi^0)^* = \phi^0$ . This scalar field has a Lagrangian density given by  $\mathcal{L} = |D_\mu \phi|^2 - V(\phi)$  and a potential  $V(\phi) = \mu^2 \phi^\dagger \phi + \lambda (\phi^\dagger \phi)^2$ , where  $D_\mu$  is the covariant derivative determined by  $SU(2)_L \times U(1)_Y$ . When expanding the field  $\phi$  around a minimum of the potential  $V$ , one finds out that there are infinitely many values of  $\phi$  that minimize the potential. Suppose one expands  $\phi$  around

$$\phi_0 = \frac{1}{\sqrt{2}} \begin{pmatrix} 0 \\ v \end{pmatrix}, \quad \text{so} \quad \phi(x) = \frac{1}{\sqrt{2}} \begin{pmatrix} 0 \\ v + h(x) \end{pmatrix}.$$

Deciding to expand the field around a chosen minimum  $\phi_0$  spontaneously breaks the  $SU(2)_L \times U(1)_Y$  symmetry, which in turn generates mass terms for the weak bosons in the Lagrangian. To convince oneself of the last implication, it suffices to expand the  $|D_\mu \phi|^2$  term around the chosen vacuum expectation value  $v$ , which will produce terms of the form  $M_W^2 W_\mu^+ W^{-\mu}$  and  $M_Z^2 Z_\mu^0 Z^{0\mu}$  in the Lagrangian density. This scalar field is called the Higgs field.

With that, the Standard Model of Particle Physics is governed by the following Lagrangian density:

$$\begin{aligned}\mathcal{L}_{\text{SM}} = & -\frac{1}{4}G_{\mu\nu}^a G^{a\mu\nu} - \frac{1}{4}W_{\mu\nu}^i W^{i\mu\nu} - \frac{1}{4}B_{\mu\nu} B^{\mu\nu} \\ & + |D_\mu \phi|^2 - \mu^2 \phi^\dagger \phi - \lambda(\phi^\dagger \phi)^2 \\ & + i[\bar{L} \not{D} L + \bar{e} \not{D} e + \bar{Q} \not{D} Q + \bar{u} \not{D} u + \bar{d} \not{D} d] \\ & - [Y_e \bar{L} \phi e + Y_u \bar{Q} \phi^c u + Y_d \bar{Q} \phi d + \text{h.c.}]\end{aligned}\quad (1)$$

The used notation is the following:  $\phi$ ,  $Q$ ,  $u$ ,  $d$ ,  $L$ ,  $e$  are the SM Higgs, quarks and lepton fields. The left-handed doublets are denoted by capital letters as

$$Q_i = \begin{pmatrix} u_L^i \\ d_L^i \end{pmatrix} \text{ for quarks, and } L_\alpha = \begin{pmatrix} \nu_L^\alpha \\ e_L^\alpha \end{pmatrix} \text{ for leptons,}$$

whereas for the right-handed singlets, lowercase letters are used. We use the usual covariant derivative defined as

$$D_\mu = \partial_\mu - ig_s T^a G_\mu^a - ig \frac{\sigma^i}{2} W_\mu^i - ig' \frac{Y}{2} B_\mu$$

and where  $T^a$ ,  $\sigma^i$  (Pauli matrices) and  $Y$  (weak hypercharge) are the generators of SU(3), SU(2) and SU(1) respectively, and  $g_s$ ,  $g$  and  $g'$  are the coupling constants.  $\phi^c$  is the charge conjugate of  $\phi$  defined by  $\phi^c = i \frac{\sigma_2}{2} \phi^\dagger$ .

The first line in Equation (1) describes the kinetic energies and interactions of the gauge boson fields. The field strength tensors associated to  $G_\mu^a$  (gluons),  $W_\mu^i$  and  $B_\mu$  ( $W^\pm$ ,  $Z^0$ ,  $\gamma$ ) are defined by

$$\begin{aligned}G_{\mu\nu}^a &= \partial_\mu G_\nu^a - \partial_\nu G_\mu^a - g_s f^{abc} G_\mu^b G_\nu^c \\ W_{\mu\nu}^i &= \partial_\mu W_\nu^i - \partial_\nu W_\mu^i - g \epsilon^{ijk} W_\mu^j W_\nu^k \\ B_{\mu\nu} &= \partial_\mu B_\nu - \partial_\nu B_\mu\end{aligned}$$

where  $f^{abc}$  and  $\epsilon^{ijk}$  are the group structure constants of SU(3) and SU(2), respectively. Note that the strength tensor of the hypercharge field  $B_\mu$  does not have this extra term, since U(1) is Abelian. This is the origin of gluons and electroweak bosons self-interactions.

The second line in Equation (1) describes the Higgs field and generates the masses of the weak gauge bosons  $W^\pm$ ,  $Z^0$  and of the Higgs boson. In particular, the term  $|D_\mu \phi|^2$  generates all interactions between the gauge bosons and the Higgs field.

The third line in Equation (1) is responsible for fermion kinetic energies as well as their interactions with all bosons (gluons and electroweak bosons). We have five terms: left-handed lepton doublets, right-handed lepton singlets (only charged leptons since right-handed neutrinos do not couple in the SM), left-handed quark doublets, right-handed up-type quark singlets and right-handed down-type quark singlets. The covariant derivative terms relative to each group apply only to these fermions that transform under that group. For instance, the first term would expand as

$$i \bar{L} \not{D} L = i \bar{L} \gamma^\mu D_\mu L = i \begin{pmatrix} \bar{\nu}_L^\alpha & \bar{e}_L^\alpha \end{pmatrix} \gamma^\mu \left( \partial_\mu - ig \frac{\sigma^i}{2} W_\mu^i - ig' \frac{Y}{2} B_\mu \right) \begin{pmatrix} \nu_L^\alpha \\ e_L^\alpha \end{pmatrix},$$

since the leptons do not carry colour charge, but the fourth term would expand as

$$i\bar{u}\not{D}u = i\bar{u}\gamma^\mu D_\mu u = i\bar{u}_R^i \gamma^\mu \left( \partial_\mu - ig_s T^a G_\mu^a - ig' \frac{Y}{2} B_\mu \right) u_R^i,$$

because the right-handed quark is a singlet under  $SU(2)_L$ .

Finally, the couplings between the Higgs boson and the fermions, and in turn fermion masses, are generated by the fourth line in Equation (1). These terms are gauge invariant, but give rise to fermion masses after SSB. For example, for the leptons and taking the Higgs field expansion around  $\phi_0$ , the first term expands as

$$Y_e \bar{L} \phi e = \frac{Y_e^{\alpha\beta}}{\sqrt{2}} \begin{pmatrix} \bar{\nu}_L^\alpha & \bar{e}_L^\alpha \end{pmatrix} \begin{pmatrix} 0 \\ v + h(x) \end{pmatrix} e_R^\beta = \frac{Y_e^{\alpha\beta} v}{\sqrt{2}} [\bar{e}_L^\alpha e_R^\beta]$$

which in addition to its hermitian conjugate will ultimately yield the term

$$\frac{Y_e^{\alpha\beta} v}{\sqrt{2}} [\bar{e}_L^\alpha e_R^\beta + \bar{e}_R^\alpha e_L^\beta] = \frac{Y_e^{\alpha\beta} v}{\sqrt{2}} \bar{e}^\alpha e^\beta$$

after spontaneous symmetry breaking. One can easily identify the mass of the three charged leptons as

$$m_e = \frac{Y_e^{ee} v}{\sqrt{2}}, \quad m_\mu = \frac{Y_e^{\mu\mu} v}{\sqrt{2}} \quad \text{and} \quad m_\tau = \frac{Y_e^{\tau\tau} v}{\sqrt{2}}.$$

To generate mass terms for up-type like quarks, the Yukawa term involves the charge conjugate of the Higgs doublet, as in the second term of the fourth line in Equation (1).

The Standard Model Lagrangian in Equation (1) governs the interactions between all particles within the theory. These interactions are represented as vertices in Feynman diagrams. The vertices shown in Figure 2 are all possible interactions in the SM, and are derived from the terms in the SM Lagrangian. Terms that, after SSB, involve only two fields do not result in vertices as they are interpreted as mass terms. Consequently, only vertices with at least three fields occur.

For instance, to derive the QED vertex for the electron, one must expand the terms  $i(\bar{L}\not{D}L + \bar{e}\not{D}e)$  and keep the terms of the form  $\bar{e} \cdot \dots \cdot e$ . This expansion ultimately yields two contributions. The first one corresponds to the coupling of the electron to the photon field:

$$-\frac{gg'}{\sqrt{g'^2 + g^2}} \bar{e} \gamma^\mu e A_\mu = -g_e \bar{e} \gamma^\mu e A_\mu. \quad (2)$$

The constant  $g_e$  in the latter expression refers to the electrical charge, therefore connecting both couplings  $g$  and  $g'$  with the electrical charge and the weak mixing angle, yielding  $g_e = g' \cos \theta_W = g \sin \theta_W$ . The second term that arises corresponds to the  $Z^0$  boson:

$$\frac{1}{\sqrt{g'^2 + g^2}} \left( \frac{g'^2 - g^2}{2} \bar{e}_L \gamma^\mu e_L + g'^2 \bar{e}_R \gamma^\mu e_R \right) Z_\mu^0.$$

Therefore, the  $Z^0$  boson couples to both left-handed and right-handed components of the electron field, but with different strengths. Hence, by removing the fields from Equation (2)

and multiplying by  $i$ , the coupling of the electron to the photon associated with the QED vertex is

$$\begin{array}{c} e^- \\ \swarrow \\ \bullet \end{array} \gamma \begin{array}{c} \nearrow \\ \bullet \end{array} \mu = -ig_e\gamma^\mu. \quad (3)$$

$e^+$

Each of the vertices in Figure 2 has an associated factor that can be computed from the SM Lagrangian density in a similar manner. Thus, one can observe, for example, that the Higgs boson does not couple to the photon or the gluon field, and that there is no direct interaction between three fermions.

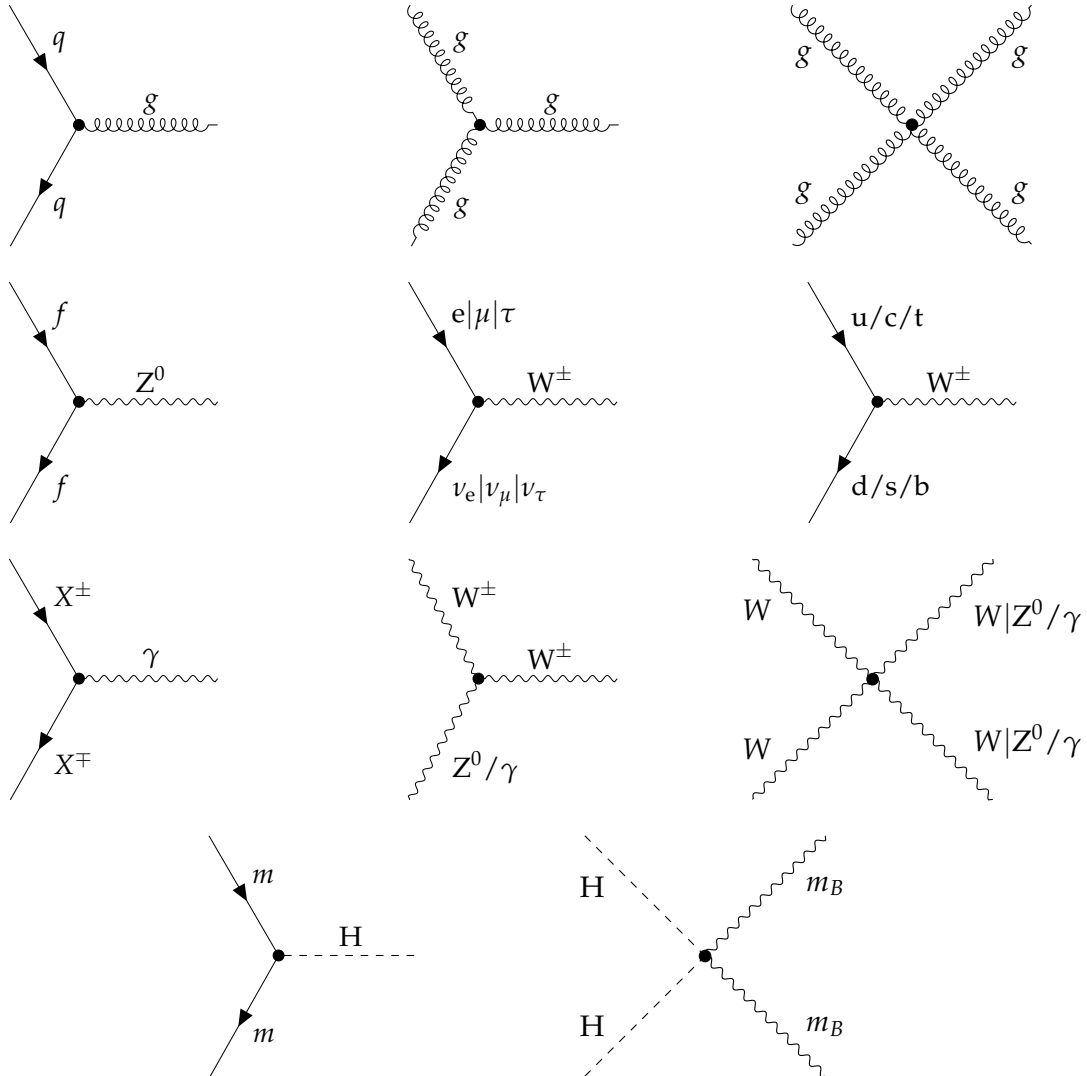


**Figure 2:** All possible interactions in the Standard Model, represented by Feynman diagrams.  $q$  is any quark,  $g$  is (any) gluon,  $X^\pm$  is any charged particle,  $\gamma$  is a photon,  $f$  is any fermion,  $m$  is any massive particle (except neutrinos),  $m_B$  is any massive boson. In diagrams with multiple particle labels separated by / one particle label is chosen. In diagrams with particle labels separated by | the labels must be chosen in the same order. For example, in the four electroweak boson case the valid diagrams are  $WWWW$ ,  $WWZ^0Z^0$ ,  $WW\gamma\gamma$  and  $WWZ^0\gamma$ .

The Standard Model has proven to predict numerous measurements with exceptional precision, like the electron magnetic moment [21]. Yet, the theory does not explain why the

masses of all particles are given by the values we measure. In fact, aside from the mass of the photon, which is protected by the unbroken U(1) gauge symmetry of QED, the SM does not predict any other mass value. All fermion masses (or equivalently, the Yukawa couplings) are free parameters of the theory.

While this theory has been remarkably successful, it cannot serve as the final theory of nature, as numerous unresolved puzzles persist. Many cosmological observations remain unaccounted for by the SM, such as the baryon-antibaryon asymmetry, the behaviour of gravity as described by General Relativity, the accelerated expansion of the Universe — potentially described by dark energy — and the absence of a suitable candidate for dark matter. Furthermore, the SM fails to explain the non-vanishing mass of the neutrinos as a consequence of neutrino flavour oscillation. In pursuit of a superior theory capable of encompassing the SM as well as these (and many other) discrepancies, the physics community is thoroughly trying to “break” the Standard Model to unveil hints towards an ultimate theory.

## 1.2 The Higgs boson

In 1964, Peter Higgs, along with Robert Brout, François Englert, Gerald Guralnik, C. R. Hagen, and Tom Kibble, proposed the Brout-Englert-Higgs mechanism to explain how certain particles (fermions and weak bosons) might acquire mass in local gauge theories [7–9]. If these ideas were correct, a spin-0 particle (namely the Higgs boson) should exist and possess some well-defined properties. Nearly 50 years later, on the 4<sup>th</sup> of July 2012, a scalar particle consistent with the Higgs boson was discovered at the LHC by the CMS and ATLAS collaborations [12, 13].

### 1.2.1 Properties of the Higgs boson

The Higgs boson is a weak isospin SU(2)<sub>L</sub> doublet, massive scalar neutral boson. Table 1 summarizes the SM predicted properties [23, 24] as well as the measured properties of the Higgs boson from the Particle Data Group (PDG) [25].

| Property        | SM prediction                              | Mesasured value                              |
|-----------------|--|--|
| Mass            | $m \lesssim 700$ GeV                       | $m = 125.25 \pm 0.17$ GeV                    |
| Spin            | $J = 0$                                    | $J = 0$                                      |
| Electric charge | $q = 0$                                    | $q = 0$                                      |
| Full width      | $\Gamma = 4.12 \pm 0.06$ MeV               | $\Gamma = 3.2^{+2.8}_{-2.2}$ MeV             |
| Lifetime        | $\tau = (1.60 \pm 0.02) \times 10^{-22}$ s | $\tau = 2.1^{+4.5}_{-1.0} \times 10^{-22}$ s |

**Table 1:** Properties of the Higgs boson. The SM prediction for the full width and the lifetime depend on the Higgs mass, which is assumed to be  $m = 125.25$  GeV.

As stated previously, the SM does not predict the mass of any particle (except for the photon), including the mass of the Higgs boson. Nevertheless, some theoretical arguments, such as radiative corrections and unitarity considerations, enabled theorists to establish upper bounds on the Higgs mass [23].

### 1.2.2 Main production modes of the Higgs boson

To understand the production and decay modes of the Higgs boson, it is important to recall that the Higgs boson couples to all the other massive particles of the SM. More precisely, it couples to the gauge bosons via the  $|D_\mu \phi|^2$  term in the Higgs part of the SM Lagrangian and to fermions via the Yukawa couplings, as well as to itself. Expanding the terms in the Lagrangian reveals that the coupling between the Higgs boson and any fermion is directly proportional to the particle's mass, while the coupling between the Higgs boson and any massive vector boson is directly proportional to the square of the particle's mass.

Collecting the relevant Feynman vertices, one determines the dominant production modes for the Higgs boson, as shown in Figure 3. Diagrams with heavy particles are dominant, since the Higgs couples through the particle's mass.

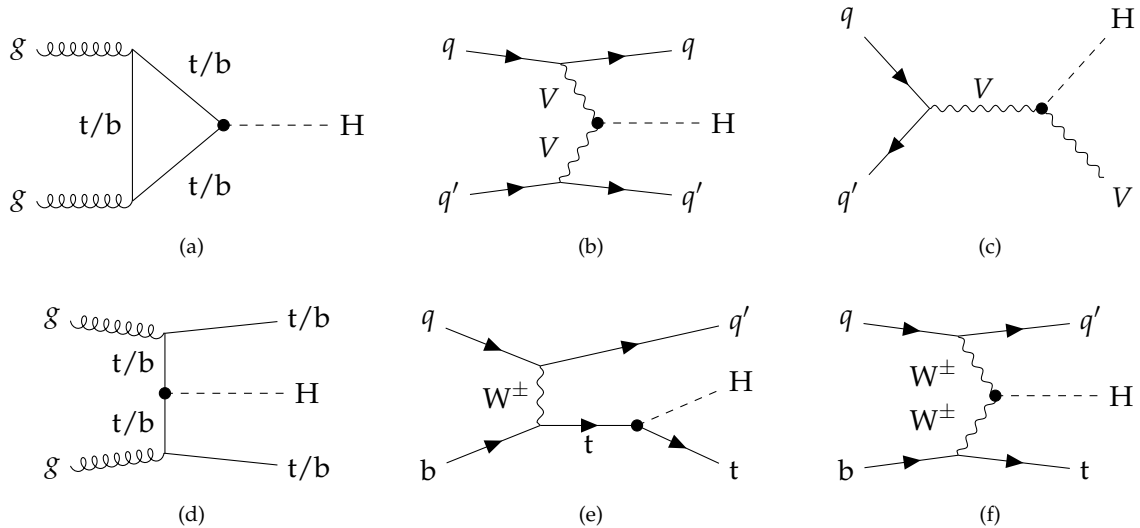


**Figure 3:** Higgs boson production in (a) gluon-gluon fusion ( $ggH$ ), (b) vector boson fusion (VBF), (c) associated production with a  $W^\pm$  or  $Z^0$  ( $V$ ) boson ( $VH$ ), also known as Higgsstrahlung, (d) associated production with a top or bottom quark pair ( $ttH$  or  $bbH$ ), or  $tt$  fusion, and (e, f) associated production with a single top quark ( $tH$ ).

In proton-proton collisions at LHC energies, the dominant process for Higgs boson production is gluon fusion ( $ggH$ ), despite being a second-order process. The second most important process at the LHC is vector boson fusion (VBF), where two fermions exchange a virtual vector boson that radiates a Higgs boson. The third contribution to Higgs boson production, and the first one at the Tevatron, a proton-antiproton collider, and at LEP, a lepton collider, is associated production with a vector boson or Higgsstrahlung (VH). In this production mode, a fermion and antifermion interact to form a virtual  $W^\pm$  or  $Z^0$  boson which, if it carries enough energy, emits a Higgs boson.

At particle colliders, Higgs boson production modes are tagged using the byproducts of the process. For instance, to identify the VBF production mode, the Higgs boson must be produced with two forward jets originating from the  $q$  and  $q'$  quarks, as shown in Figure 3 (b). Tagging Higgs boson production modes helps reduce background contamination, thereby enhancing the signal-to-background ratio.

To compare the different production cross sections with the SM predictions, it is useful to introduce some important quantities to describe interactions at particle colliders. The *center-*

*of-mass energy*  $\sqrt{s}$  describes the combined energy of the colliding particle beams and is defined as the square root of the Mandelstam variable

$$\sqrt{s} = \sqrt{(p_1 + p_2)^2},$$

where  $p_1$  and  $p_2$  are the four-momenta of the two particles. When colliding elementary particles (e.g.,  $e^+e^-$ ), the center-of-mass energy is approximately the available energy to produce particles in the collision (there is some energy spread due to synchrotron radiation). On the other hand, when colliding composite particles (e.g., protons), the available energy for particle production is substantially less due to the parton distribution functions within the proton. The *cross section*  $\sigma$  of a process describes the likelihood of a specific final state, as a measure of the effective area or target size for a particular interaction. It is measured in units of area, usually barns, defined as  $\text{barn} = 10^{-28} \text{ cm}^2$ . The number of events per unit time is expressed in terms of the *instantaneous luminosity*  $\mathcal{L}$  and the cross section of the studied event  $\sigma$  as

$$\frac{dN_{\text{events}}}{dt} = \mathcal{L}\sigma,$$

and the *integrated luminosity* is defined as

$$L = \int \mathcal{L} dt.$$

The *branching fraction* or *branching ratio*  $\mathcal{B}$  of a decay represents the fraction of particles undergoing a specific decay mode out of the total number of particles available for decay. Finally, the *signal strength*  $\mu$  expresses a measured cross section divided by the expected SM value.

Having established these fundamental concepts, it is interesting to compare the theoretical and measured cross sections for the production of the Higgs boson. This analysis uses 2018 data from the LHC, with a center-of-mass energy of  $\sqrt{s} = 13 \text{ TeV}$  and an integrated luminosity of  $L = 39.54 \text{ fb}^{-1}$ . According to the SM and assuming  $m_H = 125.25 \text{ GeV}$ , the total Higgs boson cross section at a center-of-mass energy of  $\sqrt{s} = 13 \text{ TeV}$  is  $\sigma = 55500 \pm 2800 \text{ fb}$  [24], with around 87% coming from gluon fusion, 7% from vector boson fusion and 4% from Higgsstrahlung. The predicted and measured cross section of the Higgs boson at  $\sqrt{s} = 13 \text{ TeV}$  from different production modes are shown in Table 2.

| Production mode | SM $\sigma$ [fb] | Measured $\sigma$ [fb] | Measured $\mu$  |
|-----------------|------------------|------------------------|-----------------|
| ggH             | $48400 \pm 2440$ | $47000 \pm 4500$       | $0.97 \pm 0.08$ |
| VBF             | $3774 \pm 81$    | $3020 \pm 460$         | $0.80 \pm 0.12$ |
| WH              | $1365 \pm 28$    | $2030 \pm 360$         | $1.49 \pm 0.26$ |
| $Z^0H$          | $879 \pm 36$     | $1130 \pm 220$         | $1.29 \pm 0.24$ |
| ttH + H         | $582 \pm 61$     | $660 \pm 130$          | $1.13 \pm 0.18$ |
| bbH             | $484 \pm 116$    | -                      | -               |

**Table 2:** Cross section of the Higgs boson's most frequent production modes at  $\sqrt{s} = 13 \text{ TeV}$ . SM values from Ref. [24], measured  $\mu$  values from Ref. [14], and measured  $\sigma$  from  $\sigma = \mu\sigma_{\text{SM}}$ . The bbH production channel has not been measured yet.

This analysis will not target specific production modes of the Higgs boson. Such an approach can help reduce background contamination, by individually studying and applying dedicated techniques to each mode, and could be part of further extensions of this analysis. Our approach considers then all production modes, which will be dominated by gluon fusion.

### 1.2.3 Main decay channels of the Higgs boson

The Higgs boson is a very short-lived particle, decaying almost instantaneously after its production into lighter particles. According to the couplings of the Higgs field to all other SM particles, at the first loop order, the Higgs boson predominantly decays to the most massive particles that are kinematically accessible. However, there are certain decay modes where the Higgs boson decays into massless particles, such as gluon or photon pairs, as the first-loop contributions are not negligible. Figure 4 shows the most relevant Feynman diagrams for the Higgs boson decay, while Table 3 presents the most frequent decay channels for the Higgs boson, comparing the SM predicted branching ratios to the measured ones for every decay mode.

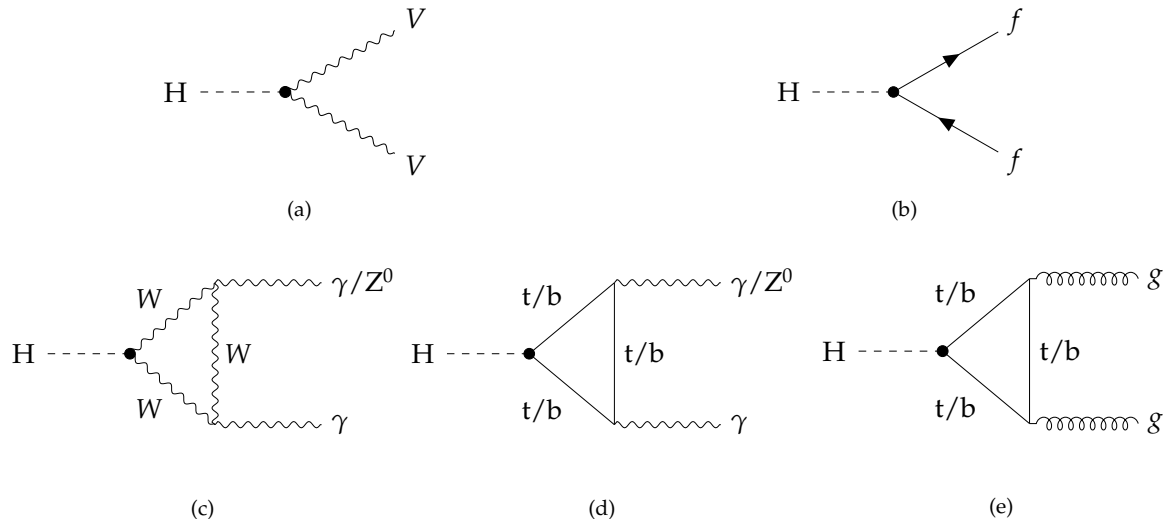


**Figure 4:** Higgs boson decays into (a) heavy vector boson pairs ( $V$  is  $Z^0/W^\pm$ ), (b) fermion-antifermion pairs, (c, d) photon pairs or  $Z^0\gamma$ , and (e) gluon pairs.

| Decay channel                | SM $\mathcal{B}$ (%) | Measured $\mathcal{B}$ (%) | Measured $\mu$       |
|------------------------------|----------------------|----------------------------|----------------------|
| $H \rightarrow b\bar{b}$     | $57.8 \pm 0.7$       | $60 \pm 12$                | $1.04 \pm 0.20$ [26] |
| $H \rightarrow WW^*$         | $21.8 \pm 0.3$       | $20.7 \pm 2.1$             | $0.95 \pm 0.09$ [27] |
| $H \rightarrow gg$           | $8.2 \pm 0.4$        | -                          | -                    |
| $H \rightarrow \tau^+\tau^-$ | $6.23 \pm 0.10$      | $6.1 \pm 1.1$              | $0.98 \pm 0.18$ [28] |
| $H \rightarrow c\bar{c}$     | $2.87 \pm 0.16$      | $< 40$                     | $< 14$ [29]          |
| $H \rightarrow ZZ^*$         | $2.68 \pm 0.04$      | $2.6 \pm 0.3$              | $0.97 \pm 0.12$ [14] |
| $H \rightarrow \gamma\gamma$ | $0.227 \pm 0.005$    | $0.254 \pm 0.021$          | $1.12 \pm 0.09$ [30] |
| $H \rightarrow Z^0\gamma$    | $0.155 \pm 0.009$    | $0.37 \pm 0.14$            | $2.4 \pm 0.9$ [31]   |
| $H \rightarrow s\bar{s}$     | $0.025 \pm 0.001$    | -                          | -                    |
| $H \rightarrow \mu^+\mu^-$   | $0.0216 \pm 0.0004$  | $0.026 \pm 0.009$          | $1.19 \pm 0.43$ [32] |

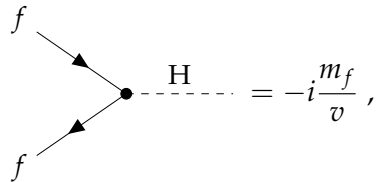
**Table 3:** Most frequent decay modes of the Higgs boson. SM values from Ref. [14, 24], and measured  $\mathcal{B}$  from  $\mathcal{B} = \mu \mathcal{B}_{\text{SM}}$ . The  $H \rightarrow gg$  and  $H \rightarrow s\bar{s}$  decay channels have not been measured yet.

The predicted values by the SM in Table 3 are of significant interest, and there are some remarks worth mentioning.

Firstly, it is observed that there is no decay  $H \rightarrow t\bar{t}$ . This is because the Higgs boson is

lighter than the top quark,  $m_H = 125 \text{ GeV} < m_t = 173 \text{ GeV}$ , making it not massive enough to produce a top-antitop quark pair. In fact, the Higgs boson can not even create one real top quark and one virtual top quark. Consequently, the presence of top quarks in the Higgs boson decays is limited to virtual loops, as the ones present in diagrams (d) and (e) of Figure 4.

Let us examine the branching ratios in Table 3 more closely, starting with the fermionic decays. The Higgs-fermion vertex has a factor of



$$f \quad f \quad H \quad = -i \frac{m_f}{v}, \quad (4)$$

thus at first approximation, the expected decay width at tree level can be estimated as proportional to

$$\Gamma(H \rightarrow f\bar{f}) \propto N_C m_f^2, \quad (5)$$

where  $N_C$  is the number of colours (3 for quarks, 1 for leptons). It is important to note that the mass to use in the above expression is the *running mass* of the particle at an energy scale of  $\mu = m_H$ , rather than the ones presented in Figure 1<sup>1</sup>. Using the running masses of the particles (for precise values of the running masses, see Ref. [33]) and the approximation presented above, we obtain the following relation of decay widths for the quarks, taking  $\Gamma(H \rightarrow s\bar{s}) = 1$ :

$$\Gamma(H \rightarrow b\bar{b}) : \Gamma(H \rightarrow c\bar{c}) : \Gamma(H \rightarrow s\bar{s}) \approx 2834 : 136 : 1,$$

while the full SM computation yields

$$\Gamma(H \rightarrow b\bar{b}) : \Gamma(H \rightarrow c\bar{c}) : \Gamma(H \rightarrow s\bar{s}) = 2312 : 115 : 1.$$

The approximation in Equation (5) is even better for leptons:

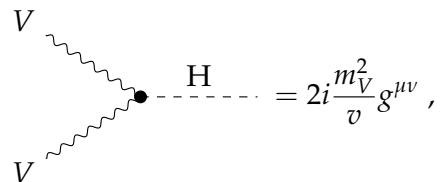
$$\Gamma(H \rightarrow \tau^+ \tau^-) : \Gamma(H \rightarrow \mu^+ \mu^-) \approx 288.53 : 1,$$

while the full SM computation is remarkably close, giving

$$\Gamma(H \rightarrow \tau^+ \tau^-) : \Gamma(H \rightarrow \mu^+ \mu^-) = 288.43 : 1.$$

The discrepancies between this initial approximation and the results from the SM in Table 3 arise from phase space factors, higher-order Feynman diagrams, and, in the case of quarks, QCD corrections.

For vector bosons, the vertex has a factor of



$$V \quad V \quad H \quad = 2i \frac{m_V^2}{v} g^{\mu\nu}, \quad (6)$$

<sup>1</sup>The masses of the quarks that are typically provided, for example, in Ref. [25], are  $m_u(\mu = 2 \text{ GeV})$ ,  $m_d(\mu = 2 \text{ GeV})$ ,  $m_s(\mu = 2 \text{ GeV})$ ,  $m_c(\mu = m_c)$ ,  $m_b(\mu = m_b)$ . The t-quark mass is determined from event kinematics, see Ref. [25]. The differences in the masses at the Higgs energy scale compared to the “usual” values are more pronounced for heavy quarks. For more information on running masses refer to Ref. [33].

and similarly, one can estimate the expected decay width at tree level as proportional to

$$\Gamma(H \rightarrow VV) \propto m_V^4. \quad (7)$$

When we compute the same relations as for the fermions we obtain

$$\Gamma(H \rightarrow WW^*) : \Gamma(H \rightarrow ZZ^*) \approx 0.604 : 1,$$

while the full SM computation differs by almost a factor of 14:

$$\Gamma(H \rightarrow WW^*) : \Gamma(H \rightarrow ZZ^*) = 8.134 : 1.$$

Despite the vertex in Equation (6) suggesting that  $\Gamma(H \rightarrow WW^*) < \Gamma(H \rightarrow ZZ^*)$  due to  $m_W < m_Z$ , other factors play a more significant role in the decay width than just the vertex factors in the boson decays. Foremost, the phase space of the decay into  $Z^0$  bosons includes an extra  $\frac{1}{2}$  symmetry factor due to the decay involving two identical particles. The remaining factor of 7 arises from the inclusion of higher-order Feynman diagrams and, most significantly, from the phase space contribution. The latter contribution quantifies the number of valid momentum and energy configurations for the outgoing particles while still obeying the conservation of energy and momentum.

Note that  $m_W, m_Z < m_H < 2m_W, 2m_Z$ , so for the Higgs boson to decay into two electroweak bosons, one of them must be *off-shell* or *virtual* (indicated with an asterisk). Off-shell or virtual particles do not need to satisfy the equation  $E^2 - p^2 = m^2$ , and are very short-lived. Therefore, for instance, the decay  $H \rightarrow WW^*$  means that the Higgs boson decays into a real  $W$  boson and a virtual  $W^*$  boson, which immediately decays into other particles. The phase factor for such a decay is intricate, as it involves the decay of a virtual boson into all possible channels, but is much smaller than it would be if the Higgs could decay to two real  $Z^0$  or  $W^\pm$  bosons. Additionally, the phase space contribution for the  $ZZ^*$  channel is much smaller than that for the  $WW^*$ . This is mainly because the  $Z^0$  boson is substantially heavier, and thus the available phase space is further reduced.

There are two decaying channels in Table 3 that have not yet been experimentally tested. The  $H \rightarrow s\bar{s}$  channel is extremely challenging to measure due to its low branching fraction, which is more than two orders of magnitude smaller than that of the  $c\bar{c}$  channel, for which only an upper bound is currently known. The other channel, accounting for approximately 8% of the Higgs boson decays, is the decay into a pair of gluons. Experimentally determining this branching ratio at the LHC is incredibly difficult because it involves QCD processes that are almost indistinguishable from the QCD background present at the Large Hadron Collider.

Additionally, the Higgs boson decays into massless particles (gluons and photons) account for one in 12 decays. This indicates that, despite being higher-order Feynman diagrams, heavy quark loops, mainly involving top and bottom quarks, are not negligible and compete with tree-level decays. The decay into a pair of photons is particularly interesting because its signature in hadron colliders is relatively clean compared to the hadronic background, and was used in the Higgs boson discovery at the LHC in 2012.

### 1.3 The Search for a model beyond the SM

If the Standard Model is correct, the coupling between the Higgs boson and each massive fermion (boson) is directly proportional to the fermion’s mass (the square of the boson’s mass), as shown in Equations (4) and (6). One can visualize these relationships by plotting the Higgs couplings against the masses of the particles. According to the SM, this should result in a linear relationship, as in Figure 5.

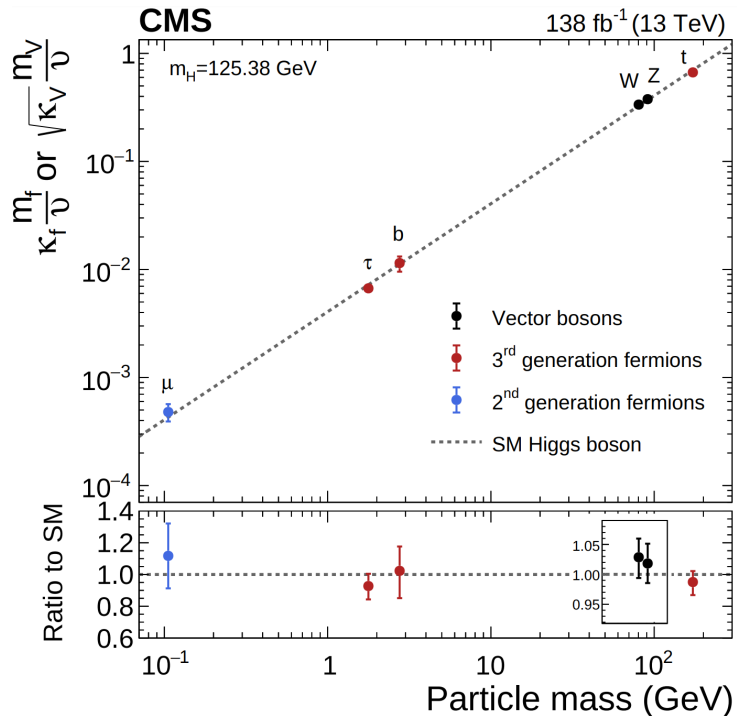


**Figure 5:** Relationship between the Yukawa couplings of the heavy members of the third generation of fermions, massive bosons, and the second-generation muon and its masses, from Ref. [14]. The dashed line in the upper plot represents the Standard Model prediction. The bottom plot shows the ratio between the measured values and the SM prediction.

As of the time of writing, the measured values for the massive weak bosons, the heavy members of the third generation of fermions (top and bottom quarks and the tau lepton), as well as the second-generation lepton (the muon), align remarkably well with the Standard Model predictions, as seen in Figure 5. This exceptional agreement with the predictions of the Higgs mechanism, spanning three orders of magnitude in mass, is a powerful test of the validity of the underlying physics.

To further test the validity of the SM, it is interesting to expand the plot to include lighter fermions, specifically the second-generation strange and charm quarks, as well as the first-generation fermions up and down quarks and the electron. Additionally, the non-vanishing masses of the neutrinos may suggest a Yukawa-type coupling for them as well.

Direct searches for Higgs boson decays into charm pairs have been conducted by both the ATLAS and CMS collaborations [29, 34–36]. Additionally, searches for  $H \rightarrow e^+e^-$  have been carried out to complete the picture [37, 38]. Furthermore, both collaborations have explored potential Beyond the Standard Model (BSM) couplings of the Higgs boson, including searches

for flavour-changing neutral currents via t-quark decays ( $t \rightarrow cH$  and  $t \rightarrow uH$ ), as well as lepton flavour-violating decays such as  $H \rightarrow e^\pm \mu^\mp$ ,  $H \rightarrow e^\pm \tau^\mp$  and  $H \rightarrow \mu^\pm \tau^\mp$  [37, 39, 40]. To date, no evidence supporting these couplings has been found.

Currently, the couplings of light quarks (up, down, charm and strange) to the Higgs boson remain loosely constrained by the existing data on the total Higgs boson width. The large multi-jet background at the LHC inhibits the study of such couplings with inclusive  $H \rightarrow q\bar{q}$ . Rare exclusive decays of the Higgs boson into a light meson and a photon have been proposed as a probe of both flavour-conserving and flavour-violating couplings of the Higgs boson to light quarks. Exclusive decays involving  $W^\pm$  and  $Z^0$  bosons are also a possibility [41].

Initial experimental upper limits on hadronic two-body Higgs decays have been established by the ATLAS and CMS collaborations (ATLAS-CMS:  $H \rightarrow J/\psi + \gamma$  [15, 16], ATLAS:  $H \rightarrow \rho, \phi, \omega, K^{*0} + \gamma$  [17, 18], CMS:  $H \rightarrow J/\psi, \rho, \phi + Z^0$  [19, 20]).

This analysis focuses on decays of the form  $H \rightarrow M\gamma$ , where  $M$  represents a light vector meson with a mass of approximately 1-2 GeV. It is important to note that, given that the Higgs boson has spin 0 and the photon has spin 1, the meson  $M$  must be a *vector* meson to conserve total angular momentum.

Table 4 presents exotic decays of this form. The first four rows involve similar processes in which the vector meson decays into a pair of lighter, charged scalar mesons. The processes

| Higgs boson rare decay   | Coupling                             |
|--|--------------------------------------|
| $H \rightarrow J/\psi\gamma$<br>└─→ $\mu^+ \mu^-$ ( $5.961 \pm 0.033\%$ )  | charm quark                          |
| $H \rightarrow \rho^0\gamma$<br>└─→ $\pi^+ \pi^-$ ( $\sim 100\%$ )   | up/down quark                        |
| $H \rightarrow \phi\gamma$<br>└─→ $K^+ K^-$ ( $49.1 \pm 0.5\%$ )   | strange quark                        |
| $H \rightarrow K^{*0}\gamma$<br>└─→ $K^\pm \pi^\mp$ ( $\sim 100\%$ )   | flavour-violating down/strange quark |
| $H \rightarrow \phi\gamma$<br>└─→ $\pi^+ \pi^- \pi^0$ ( $15.4 \pm 0.4\%$ )   | strange quark                        |
| $H \rightarrow \omega\gamma$<br>└─→ $\pi^+ \pi^- \pi^0$ ( $89.2 \pm 0.7\%$ )   | up/down quark                        |
| $H \rightarrow D^{*0}\gamma$<br>└─→ $D^0 + \pi^0/\gamma$ ( $\sim 100\%$ )<br>└─→ $K^- \pi^+$ ( $3.947 \pm 0.030\%$ )<br>└─→ $K^- \pi^+ \pi^0$ ( $14.4 \pm 0.5\%$ ) | flavour-violating up/charm quark     |

**Table 4:** Higgs rare decays of the form  $H \rightarrow M\gamma$ , where  $M$  is a vector meson containing light quarks. The top half of the table focuses on decays where the light neutral vector meson decays into a pair of charged mesons. The bottom half of the table focuses on similar decays, but where there are also one or two neutral particles involved in the decay of the primary meson. All these decays are currently being analysed by the CMS collaboration. The branching ratios of meson decays are shown in parenthesis, from the PDG [25].

involving a  $\rho^0$ ,  $\phi$  and  $K^{*0}$  meson are currently under analysis by the CMS collaboration as

of the writing of this document. However, this analysis focus specifically in the lower half of the table, where the vector meson decay involves a pair of charged scalar mesons along with neutral particles, specifically either pions or photons.

The current branching ratio information of these decays, both theoretical and experimental, is shown in Table 5. For the first four decays in Table 5, the measured upper limits are 67,

| Decay channel                | SM $\mathcal{B}$                      | Measured $\mathcal{B}$      |
|------------------------------|---------------------------------------|-----------------------------|
| $H \rightarrow J/\psi\gamma$ | $(2.99 \pm 0.16) \times 10^{-6}$ [42] | $< 2.0 \times 10^{-4}$ [15] |
| $H \rightarrow \rho^0\gamma$ | $(1.68 \pm 0.08) \times 10^{-5}$ [43] | $< 8.8 \times 10^{-4}$ [17] |
| $H \rightarrow \phi\gamma$   | $(2.31 \pm 0.11) \times 10^{-6}$ [43] | $< 4.8 \times 10^{-4}$ [17] |
| $H \rightarrow \omega\gamma$ | $(1.48 \pm 0.08) \times 10^{-6}$ [43] | $< 1.5 \times 10^{-4}$ [18] |
| $H \rightarrow K^{*0}\gamma$ | $< 10^{-11}$ [18]                     | $< 8.9 \times 10^{-5}$ [18] |
| $H \rightarrow D^{*0}\gamma$ | -                                     | -                           |

**Table 5:** Higgs rare decay branching fractions. Because of the very large hadronic background at the LHC, only upper limits on the branching ratios have been computed so far, which are around two orders of magnitude bigger than the SM prediction. The  $H \rightarrow D^{*0}\gamma$  channel has not been measured yet.

52, 208 and 95 times the expected SM values, respectively. For the  $H \rightarrow K^{*0}\gamma$  decay, only  $\mathcal{B}(H \rightarrow d\bar{s} + \bar{d}s)$  is available, with a value of  $\mathcal{B}(H \rightarrow d\bar{s} + \bar{d}s) = 1.19 \times 10^{-11}$  [44]. However,  $\mathcal{B}(H \rightarrow K^{*0}\gamma)$  is expected to be much smaller [18]. A similar situation occurs for the last decay, where only  $\mathcal{B}(H \rightarrow c\bar{u} + \bar{c}u)$  is available, with a value of  $\mathcal{B}(H \rightarrow c\bar{u} + \bar{c}u) = 5.00 \times 10^{-20}$  [44].

When studying Higgs boson decays of the form  $H \rightarrow M\gamma$ , which in essence are  $H \rightarrow q\bar{q}\gamma$ , there are different Feynman diagrams that contribute to the width. We can distinguish the contributions into two different vertices. On the one hand, we have the tree-level diagram, which provides the direct contribution and is shown in diagram (a) of Figure 6. On the other hand, we have all other higher-order diagrams joined as an effective indirect vertex, represented in diagram (b) of Figure 6.

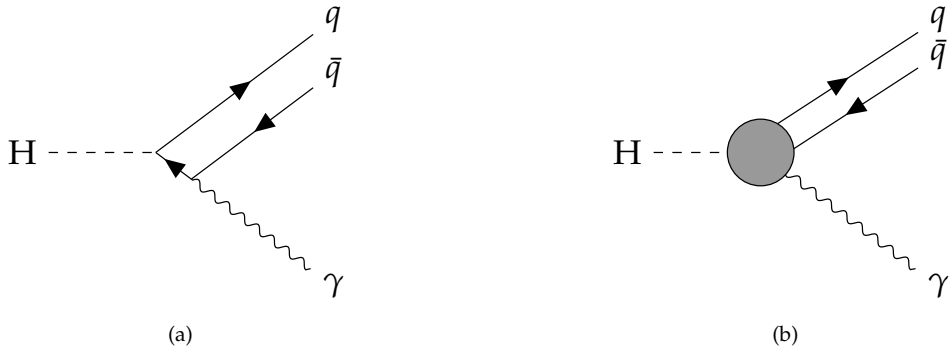


**Figure 6:** Direct (a) and indirect (b) contributions involved in the decays under analysis.  $q$  stands for any light quark.

According to the Standard Model, for light quarks  $q$  like the strange quark, the direct contribution is of the order of  $10^{-11}$ , while the indirect contribution is of the order of  $10^{-6}$ , which means that higher-order corrections dominate the behaviour of these type of decays.

A few examples of diagrams that contribute to the effective vertex are provided in Figure 7. In diagrams (a) and (c) the dotted-line loop can either be a heavy charged fermion loop or a  $W^\pm$  boson loop. To ultimately compute the Yukawa couplings to the lighter families of quarks,

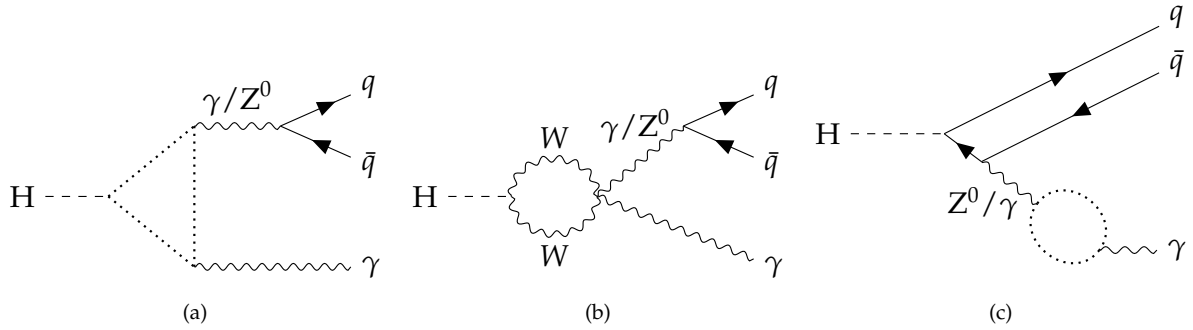


**Figure 7:** Some examples of the many one-loop diagrams accounted for in the effective vertex. The dotted-line loops are heavy charged fermion or  $W^\pm$  boson loops, and  $q$  stands for any light quark.

one has to take into consideration contributions from both the direct and the indirect vertex, since experimentally what is measured from the direct decay is the overall effect coming from both vertices.

The decays studied in this thesis (bottom half part of Table 4) share many similarities. In particular, the decays  $H \rightarrow \phi\gamma$  and  $H \rightarrow \omega\gamma$  will have many common features in the framework, as both further decay into three pions  $\phi/\omega \rightarrow \pi^+\pi^-\pi^0$ . Similarly, the decays involving a  $D^{*0}$  meson,  $H \rightarrow D^{*0}\gamma$ , also display many similarities. It is worth mentioning that although the analysis explicitly targets only  $H \rightarrow D^{*0}\gamma$ , the charge conjugate decay  $H \rightarrow \overline{D^{*0}}\gamma$  is implicit, as the analysis is entirely symmetric under charge conjugation. This will be considered when computing the final results.

The main difference between this analysis and the one studying the four decays presented in the top half of Table 4 lies in the fact that we are dealing with 3-body decays involving neutral particles, which are more challenging to reconstruct compared to charged ones. That is why we will focus most of our attention on accurately reconstructing the neutral particles.

The goal of this Master's Thesis is to compute an expected upper limit for the branching ratio of the aforementioned Higgs boson decays. Table 5 shows the order of magnitude of the branching fractions one would ultimately like to measure. Nevertheless, due to the large hadronic background at the LHC, analyses of this kind are targeting an upper limit rather than a precise measurement at this stage.

Deviations from the predictions of the Standard Model within the Higgs boson sector can serve as compelling indications of new physics beyond our current understanding of particle physics. The Higgs boson plays a central role in the SM by giving particles mass through the Higgs mechanism. Therefore, any discrepancies in its properties, including decay widths, could reveal hidden phenomena and particles that the SM fails to describe.

One possible scenario involves determining an upper limit on a Higgs decay branching ratio that significantly exceeds the SM prediction. Such a discrepancy would suggest the presence of additional particles and interaction processes not accounted for in the SM. These new BSM particles could contribute to the Higgs decay width in ways not initially anticipated.

Accurate measurements are essential in this context, as they allow probing the Higgs sector with the highest level of precision. Through the precise determination of the Higgs boson's properties, one can identify even the most subtle deviations from the SM, providing

clues about the nature of new physics. Consequently, the need for precision in Higgs boson measurements is of utmost importance, as it can not only further confirm the validity of the SM but also has the potential to illuminate the path towards a more comprehensive theory of particle physics, one that goes beyond the boundaries of the Standard Model.

The Future Circular Collider (FCC) project, with its proposed scenarios, including FCC-ee (electron-positron collisions) and FCC-hh (hadron-hadron collisions), presents a promising opportunity to advance our understanding of the Higgs boson and, by extension, the Standard Model [45]. The FCC-ee, with its high-energy lepton collisions, would enable us to conduct precise measurements of the Higgs boson's properties, including its interactions with other SM particles. This collider could provide an order of magnitude improvement in accuracy compared to current experiments, allowing for detailed studies of the Higgs,  $W^\pm$ , and  $Z^0$  bosons, as well as the top quark [46, 47]. Together with the FCC-hh, which would operate with hadron collisions at significantly higher energies (potentially up to 30 times that of the LHC [48]), these colliders within the FCC project hold the potential to shed light on dark matter, probe neutrino masses, and investigate other unexplained phenomena.

# Chapter 2

## The CMS at the LHC

This chapter provides a historical overview of the European Organization for Nuclear Research, commonly known by its acronym CERN (Conseil Européen pour la Recherche Nucléaire), along with the Large Hadron Collider (LHC) and the Compact Muon Solenoid (CMS) experiment. It goes through the most significant breakthroughs at CERN, with a particular emphasis on the discovery of the Higgs boson at the LHC in 2012 by the CMS and ATLAS collaborations [12, 13].

### 2.1 The Large Hadron Collider at CERN

The European Organization for Nuclear Research (CERN) is an intergovernmental organization composed of 23 member states that operates the world's largest particle physics laboratory. Established in 1954, CERN is situated on the Franco-Swiss border near Geneva, Switzerland, and is one of the largest and most influential research organizations in particle physics. The missions of CERN include world-class research in fundamental physics, sustainable and environmentally responsible accelerator facilities, global collaboration in science and technology advancement and the education and engagement of future scientists, engineers and the broader public.

CERN has been home to many accelerators, including the original linear accelerator Linac1 (in operation from 1959 until 1992), the Linac2 (1978 - 2018), the Super Proton-Antiproton Synchrotron (Sp $\bar{p}$ S) (1981-1991), the Large Electron-Positron Collider (LEP) (1989-2000), and the current Large Hadron Collider (LHC), which was constructed between 1998 and 2008 and achieved its first collisions in 2010. The Future Circular Collider (FCC) is proposed to be the successor of LHC at CERN [45].

During its nearly 70-year history since its creation, many important achievements in particle physics have been made through experiments at CERN, including:

- The discovery of neutral currents by studying neutrinos produced by the PS/SPS neutrino beam interacting in the Gargamelle bubble chamber in 1973 [49].
- The discovery of the  $W^\pm$  and  $Z^0$  bosons in the UA1 and UA2 experiments in 1983 [10, 11].
- The determination of the number of light neutrino families at LEP in 1989 [50].

- The discovery of direct CP violation in the NA48 experiment in 1999 [51].
- The discovery of the Higgs boson at LHC by the CMS and ATLAS collaborations in 2012 [12, 13].

Today, the main particle accelerator at CERN is the LHC. The Large Hadron Collider is a hadron collider primarily used for proton-proton (pp) collisions but also capable of heavy-ion collisions. It was designed to investigate the properties of the Standard Model, in particular the Higgs boson, and to study the physics Beyond the Standard Model by analysing discrepancies in the SM or via direct searches of particles. It has a circumference of 26.659 kilometres and is located underground at depths ranging from 50 to 175 meters, making it the world's largest and highest-energy particle collider [52, 53].

Two beams circulate in opposite directions within the LHC, guided by 9593 superconducting magnets. Operating at a center-of-mass energy of  $\sqrt{s} = 13$  TeV, protons from each beam have an energy of 6.5 TeV and complete about 11245 orbits around the collider's circumference every second. This is achieved by initially stripping hydrogen atoms of their electrons, leaving the protons. Several accelerators are used in sequence to accelerate these protons: first, the Linac4 accelerates them to 50 MeV, followed by the Proton Synchrotron Booster (PSB) accelerating them further to 1.4 GeV, the Proton Synchrotron (PS) to 25 GeV, and finally, the Super Proton Synchrotron (SPS), where they reach 450 GeV. The beams are then injected into the LHC, which takes them to 6.5 TeV using superconducting dipole magnets, cooled to 1.9 K with superfluid helium, producing a magnetic field of 8.3 T, and eight radio frequency (RF) cavities per beam. By tuning the energy of the protons that have a different timing than that of the RF cavity, the phase oscillations of the electromagnetic fields within these RF cavities divide the protons into 2808 bunches, each containing about  $1.15 \times 10^{11}$  protons. The collisions resulting from this process occur approximately every 25 ns, equivalent to a frequency of 40 MHz. These collisions take place at four interaction points, where the four major LHC experiments are located: ATLAS (A Toroidal LHC ApparatuS) [54], CMS (Compact Muon Solenoid) [55], ALICE (A Large Ion Collider Experiment) [56], and LHCb (Large Hadron Collider beauty) [57]. Of these four experiments, ATLAS and CMS are multipurpose detectors designed to study a wide range of physics phenomena. ALICE is specifically conceived to record the collisions of ion beams, while LHCb is optimized for studying  $b$ -physics. Moreover, several smaller experiments at the LHC focus on more specific physics goals. Figure 8 shows a diagram of CERN's Accelerator Complex.

One of the main advantages of LHC being a proton-proton collider, rather than an electron-positron collider like its predecessor LEP, is that it suffers much less from the effects of synchrotron radiation. This effect causes charged accelerated particles to lose energy, inversely proportional to the fourth power of the particle mass, making proton-proton collisions more energy efficient for a 13 TeV regime.

During Run 1 of the LHC, which spanned from 2010 to 2012, the center-of-mass energy ranged from 7 to 8 TeV, and CMS recorded a total integrated luminosity of  $29.45 \text{ fb}^{-1}$ . Run 2 took place from 2015 to 2018, with an energy of 13 TeV, and a total integrated luminosity of  $163.6 \text{ fb}^{-1}$ . In 2022, Run 3 began and is scheduled to conclude in 2026, with an energy of 13.6 TeV. In the first year of Run 3, the total integrated luminosity reached  $42 \text{ fb}^{-1}$ , and is expected to be around  $300 \text{ fb}^{-1}$  by the end of the Run [59]. The data that is going to be used in this

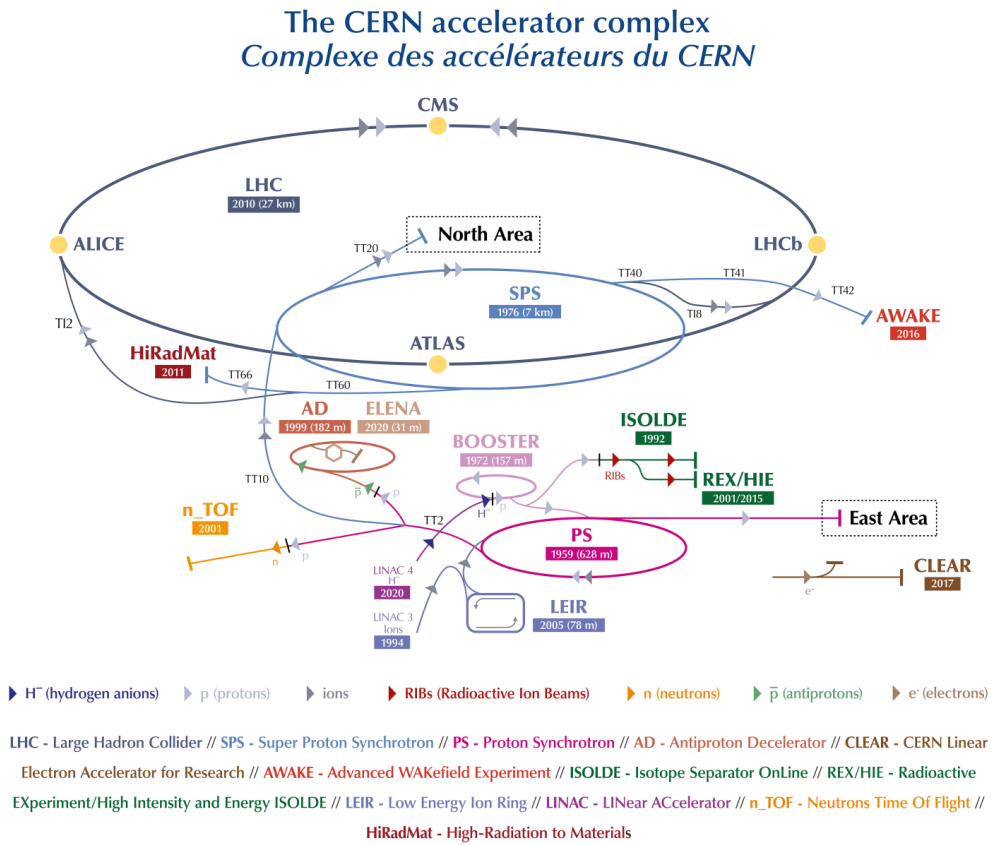


**Figure 8:** The CERN accelerator complex. The four main experiments can be seen in four different points around the LHC. Source: Ref. [58].

analysis is from the CMS collaboration and was taken in 2018 (Run 2), with  $\sqrt{s} = 13$  TeV and an integrated luminosity of  $39.54 \text{ fb}^{-1}$ .

## 2.2 The Compact Muon Solenoid

One of the four large particle detectors at the LHC is the Compact Muon Solenoid (CMS) detector. It is designed to optimize the muon detection system in proton-proton collisions, featuring a cylindrical geometry, measuring 21.5 m in length and 15 m in diameter, with a total weight of approximately 14000 tonnes. It is characterized by its solenoid magnet, which generates a 4 T magnetic field used to bend charged particles to measure their transverse momentum [55, 60].

Concentric layers of detector subsystems surround the collision point of the particle beams at the centre of the detector to measure particle trajectories and their properties. These subsystems, starting from the interaction point, include the silicon tracker, the electromagnetic calorimeter (ECAL), and the hadronic calorimeter (HCAL). Beyond the superconducting solenoid magnet there is another outer HCAL and the muon system, where another magnetic field of approximately 2 T bends the muons in the opposite direction of the first magnet. Each subdetector specializes in measuring certain particles, but they work together to reconstruct

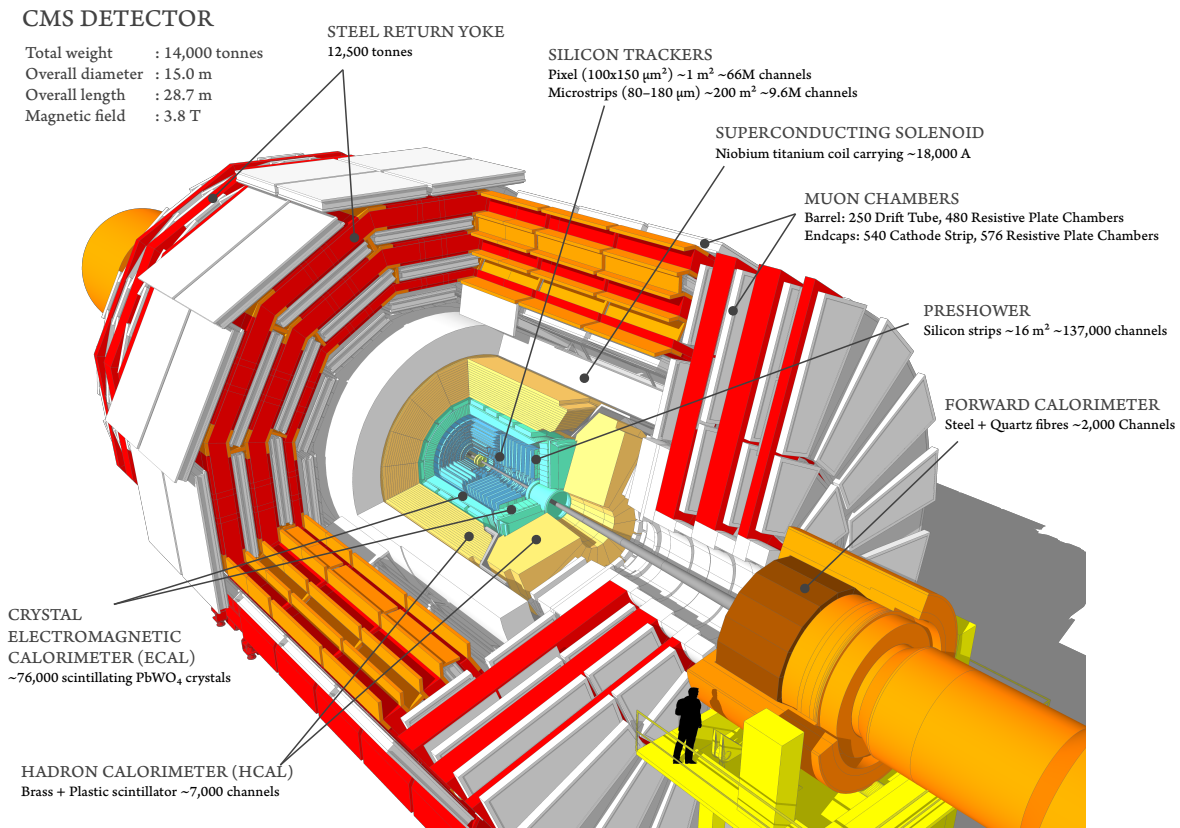


Figure 9: A cutaway view of the CMS detector. Figure from Ref. [61].

events. For more detailed information, refer to [62]. A full diagram of the structure of CMS is shown in Figure 9, while a cross section is presented in Figure 10.

The coordinate system in CMS has its origin centred at the nominal collision point within the detector. The  $z$ -axis follows the beam line, the  $y$ -axis points vertically upward, and the  $x$ -axis points radially inward toward the centre of the LHC ring. The azimuthal angle  $\phi$  is measured from the  $x$ -axis in the  $x - y$  plane, with the radial coordinate denoted as  $r$ , and the polar angle  $\theta$  is measured from the  $z$ -axis. However,  $\theta$  is not often used because it is not Lorentz invariant for boosts along the direction of the beam. Instead, the pseudorapidity is defined as  $\eta = -\ln(\tan \frac{\theta}{2})$ , which is Lorentz invariant. From this, it is possible to define the momentum orthogonal to the beam direction or transverse momentum, denoted as  $p_T$ . It is also worth defining the notion of angular distance between two directions as  $\Delta R = \sqrt{(\Delta\phi)^2 + (\Delta\eta)^2} = \sqrt{(\phi_1 - \phi_2)^2 + (\eta_1 - \eta_2)^2}$ , which will be useful throughout the analysis.

The silicon tracker is designed to measure the trajectory, charge and momentum of charged particles traversing it, as well as to reconstruct secondary vertices. It comprises two types of silicon detectors: the pixel detector (inner tracker) and the silicon strip tracker (outer tracker). They operate by measuring the ionization of charged particles. When a charged particle traverses the doped silicon wafer, it creates electron-hole pairs that move toward collection electrodes due to an applied electric field. These pairs are organized into silicon strips or pixels, providing a two-dimensional measurement. Multiple silicon wafers are arranged in different layers, and the hits measured in each layer are used to reconstruct the tracks of charged

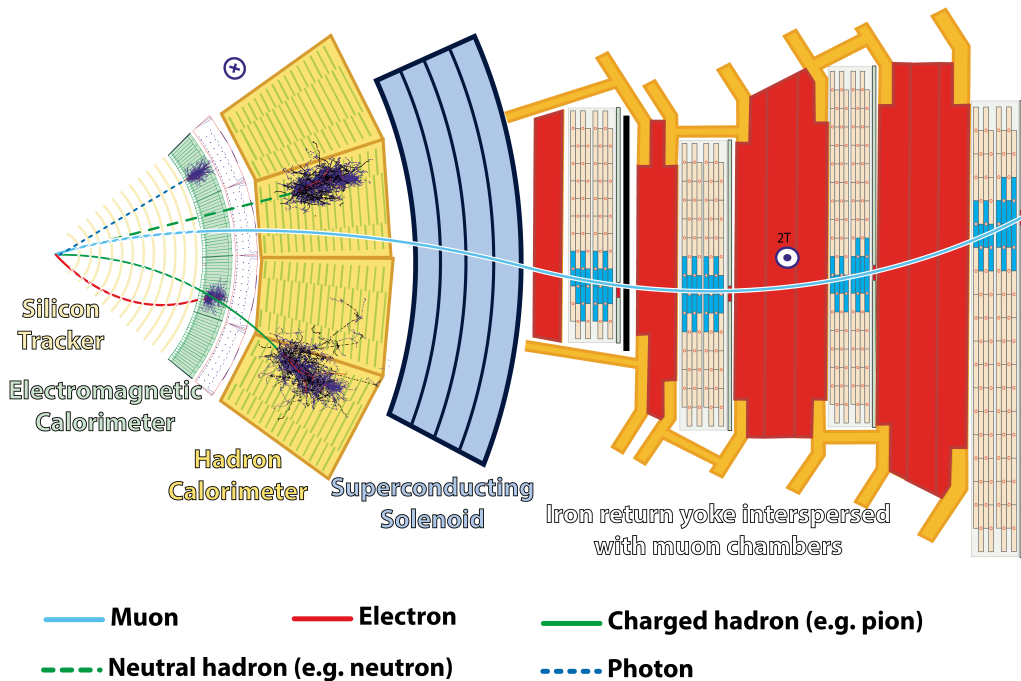


Figure 10: A slice of the CMS detector, with an illustration of the behaviour of different particles. Figure from Ref. [63].

particles through the detector. The pixel detector is the innermost component, consisting of four barrel layers and three endcap disks. The silicon strip tracker is positioned just outside, extending to a radius of 1.1 m and comprising 15148 strips arranged in ten barrel layers and twelve endcap disks.

The primary purpose of the electromagnetic calorimeter (ECAL) is to measure the energy and direction of electrons, positrons and photons. It is constructed with homogeneous lead tungstate ( $\text{PbWO}_4$ ) crystals that serve as both active scintillating material to detect the electromagnetic signal and absorbing material to initiate electromagnetic (EM) showers. Energy deposition is measured through crystal ionization, and their deexcitation photons are detected by dedicated photodetectors. The short radiation length of the crystals,  $X_0 = 0.89$  cm, ensures that the EM showers remain confined within a small region. The photodetectors are designed to withstand the high radiation and high magnetic field environment while being sufficiently fast compared to the LHC bunch crossing time. The ECAL consists of two main parts: the ECAL barrel (EB), covering  $|\eta| < 1.479$ , composed of 61200 crystals and which uses avalanche photodiodes, and the ECAL endcaps (EE), covering  $1.479 < |\eta| < 3.0$ , composed of 7324 crystals in each (lower granularity compared to the barrel) and which use vacuum phototriodes. To account for the reduced endcap granularity, preshower detectors are installed before the lead tungstate crystals, covering  $1.653 < |\eta| < 2.6$ , intended for identifying neutral pions, distinguish electrons against minimum ionizing particles, and improve position measurements. This design enables the ECAL to completely stop electrons and photons emerging from the tracker, allowing for accurate energy measurement.

Four hadronic calorimeters (HCAL) are positioned outside the ECAL. They are designed to generate hadronic showers when strongly interacting particles pass through their absorption material. These particles interact in the absorber layers, producing numerous secondary

particles and often showers, which are measured by the scintillators. The HCAL are bigger than the ECAL because the nuclear interaction length  $\lambda_{\text{int}}$  is also larger than the electromagnetic radiation length  $X_0$  (e.g., for iron,  $\lambda_{\text{int}} = 16.8$  cm, while  $X_0 = 1.76$  cm [64]). The HCAL barrel (HB) rests between the ECAL and the magnet ( $R = 1.77 - 2.95$  m), covering  $|\eta| < 1.4$ . The HCAL endcap (HE) covers  $1.3 < |\eta| < 3.0$ . Both the HB and the HE are made of brass and plastic scintillators. The HCAL outer detector (HO) is placed outside the magnet in the barrel region ( $|\eta| < 1.26$ ) to catch the tail of the shower, and it is made of iron and plastic scintillators. To ensure optimal efficiency in different pseudorapidity ranges, there is a fourth HCAL placed in the endcap regions after the muon systems. The HCAL forward detector (HF) covers  $3.0 < |\eta| < 5.0$  at  $|z| = 11.2$  m, where it is subject to much higher radiation. It is distinguished from the other HCAL sections because it is built with steel and quartz fibres, leading to shorter hadronic showers for better absorption of very forward hadron showers. Note that the ECAL already absorbs a fraction of the energy of the hadrons, but the HCAL design allows it to fully stop the hadrons and measure any remaining energy, which is later combined with the ECAL information to obtain a complete picture.

Muon identification was a focal point for CMS because muons produced in proton-proton collisions offer clear lepton signatures for a wide range of physics processes and helps with their reconstruction. The CMS muon system consists of several subdetectors dedicated to measure muons with high precision. To achieve accurate muon identification, the muon detectors were designed with extensive pseudorapidity coverage, up to  $\eta = 2.4$ . CMS's muon system uses three types of detectors: Drift Tubes, Resistive Plate Chambers and Cathode Strip Chambers. Muon Drift Tubes (DT) contain a wire and a gas mixture (85% Ar, 15% CO<sub>2</sub>) at atmospheric pressure that ionizes when traversed by a muon. The deexcitation electrons follow the electric field to reach the wire, recording the signal. By recording the distance from the wires and the location along the wires, the DT determine two coordinates of the muon's positions. Resistive Plate Chambers (RPC) are gaseous (95.2% C<sub>2</sub>H<sub>2</sub>F<sub>4</sub>, 4.5% i-C<sub>4</sub>H<sub>10</sub>, 0.3% SF<sub>6</sub>) parallel plate capacitors with high timing resolution. Cathode Strip Chambers (CSC) consist of positively charged anode wires crossed with negatively charged cathode panels within a gas volume (40% Ar, 50% CO<sub>2</sub>, and 10% CF<sub>4</sub>), which ionize when traversed by a muon: positive ions move toward the cathode and the electrons move toward the anode wires. In the CMS detector's barrel ( $|\eta| < 1.2$ ), the DT are arranged in four concentric layers interleaved with five layers of the iron magnet yoke and six layers of RPCs, as shown in Figure 10. In the endcap region, reaching  $\eta = 2.4$ , there are three RPC layers (up to  $\eta = 1.6$ ) and six CSC layers, chosen in this region for their ability to resist high non-uniform magnetic fields. Muons do not deposit much energy in matter at the working energy of the LHC, so they pass through both calorimeters with most of their momentum. The muon chambers then provide further information about the muon's trajectory, as they are the only particles with a clear signal in this section. These trajectories, combined with those of the trackers, allow for better muon identification and provide additional data on their momenta.

Storing all recorded events in the detector is impractical, so only events meeting specific conditions are preserved. The Level 1 (L1) Trigger uses local trigger information from all subdetectors, excluding the Inner Tracker, to determine whether to save an event. With the aid of custom hardware and firmware, it reduces the event rate from 40 MHz to 100 kHz. It considers information from the four highest  $E_T$  electrons, photons, central jets, forward jets,

tau-jets, the four highest  $p_T$  muons, the event's missing transverse energy (MET), and the scalar sum of the jet transverse momenta (HT). Subsequently, data is processed by the High-Level Trigger (HLT), a comparatively slower software, to further filter events based on trigger menus, reducing the rate to around 1 kHz. The CMS offline physics object reconstruction is achieved using the Particle Flow (PF) algorithm, which integrates information from all subdetectors to reconstruct all particles in the event.

The Compact Muon Solenoid experiment is one of the largest international scientific collaborations in history, involving more than 6000 particle physicists, engineers, technicians, students and support staff from 257 institutes in 59 countries as of October 2023 [65].

## 2.3 The discovery of the Higgs boson

Nearly 50 years after the Higgs boson had been proposed, in 2012, the CMS and ATLAS collaborations observed a new scalar boson with a mass of 125 GeV [12, 13]. The properties of this particle were compatible with those of the Higgs boson, including its spin and mass. In 2012, precision electroweak measurements and direct searches at LEP had constrained the mass of the Higgs boson to be in the interval  $114.4 \text{ GeV} < m_H < 152 \text{ GeV}$  at 95% confidence level (CL) [66, 67].

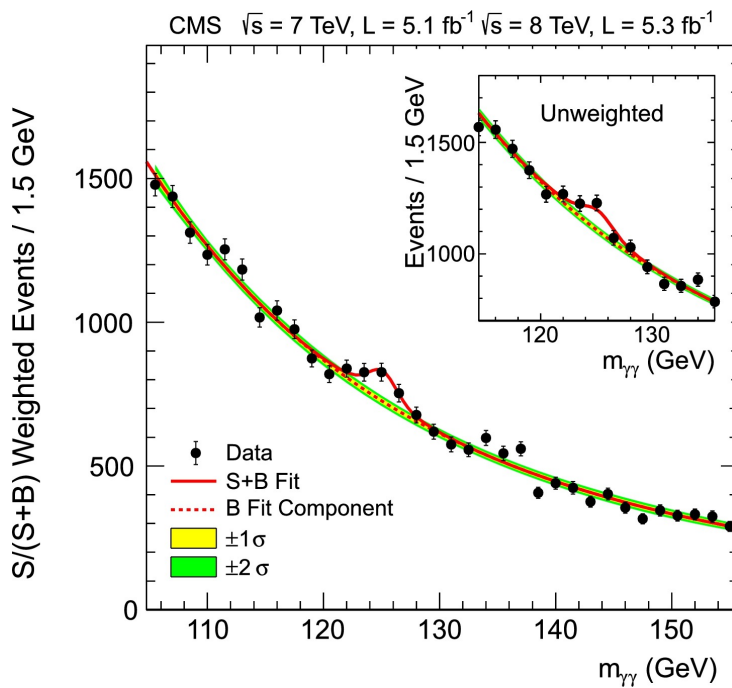


**Figure 11:** The diphoton invariant mass distribution computed by CMS, from Ref. [12]. The lines represent the fitted background and signal, and the coloured bands  $\pm 1 \sigma$  and  $\pm 2 \sigma$  in the background estimate.

The CMS experiment used data recorded at  $\sqrt{s} = 7$  and 8 TeV, with integrated luminosities of up to  $5.1 \text{ fb}^{-1}$  at 7 TeV and  $5.3 \text{ fb}^{-1}$  at 8 TeV. For the search, five decay modes were employed:  $H \rightarrow \gamma\gamma$ ,  $ZZ^*$ ,  $WW^*$ ,  $\tau^+\tau^-$  and  $b\bar{b}$ , which according to the SM is about 89% of all the decay modes of the Higgs boson (see Table 3). They reported an excess of events over the expected background, consistent with the production of a new particle with mass near 125 GeV, with an

observed local significance of 5.0 standard deviations ( $\sigma$ ). The strongest evidence came from the two final states with the best mass resolution, which are  $H \rightarrow \gamma\gamma$  with a significance of  $4.1\sigma$  and  $H \rightarrow ZZ^*$  with a significance of  $3.2\sigma$ . Moreover,  $H \rightarrow \gamma\gamma$  indicated that the new particle was a boson with spin different from one [12]. Figure 11 presents the diphoton invariant mass  $m_{\gamma\gamma}$  presented by CMS in 2012, where the excess at 125 GeV is evident in the weighted and unweighted distributions.

The confidence level of the combined result as a function of the Higgs boson mass is presented in Figure 12. The observed values are shown as the solid points, while the dashed line represents the median of the expected results for the background-only hypothesis. The green and yellow bands indicate the ranges where  $CL_s$  values are expected to lie in 68% and 95% of the experiments under the background-only hypothesis. The red horizontal lines indicate  $CL_s$  values of 0.05, 0.01, and 0.001. The mass regions where the observed  $CL_s$  values are below these lines are excluded with the corresponding  $(1 - CL_s)$  confidence levels. In the range  $121.5 < m_H < 128$  GeV a significant excess is observed, and the SM Higgs boson cannot be excluded at 95% CL. They also determined the Higgs boson mass by using the  $\gamma\gamma$  and  $ZZ^*$  decay modes, obtaining a value of  $m_H = 125.3 \pm 0.4$  (stat.)  $\pm 0.5$  (syst.) GeV =  $125.3 \pm 0.6$  GeV.

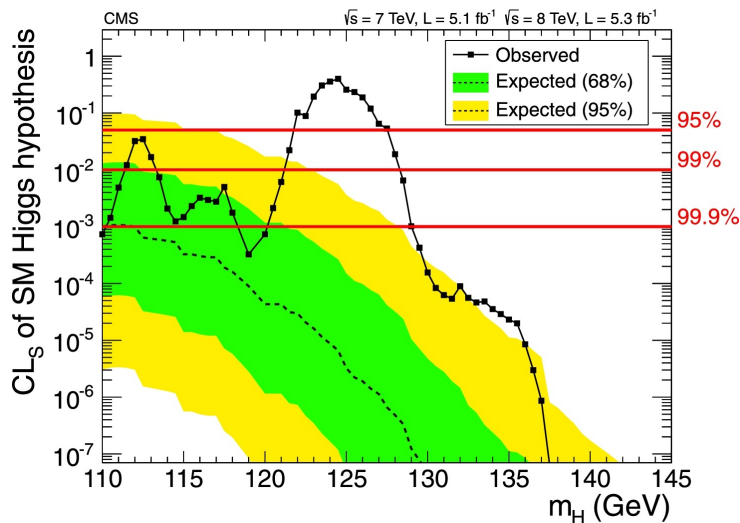


**Figure 12:** The  $CL_s$  values for the SM Higgs boson hypothesis as a function of the Higgs boson mass in the range 110-145 GeV, by CMS from Ref. [12].

In ATLAS's analysis [13], they reported a significance of  $5.9\sigma$  and a mass of  $m_H = 126.0 \pm 0.4$  (stat.)  $\pm 0.4$  (syst.) GeV =  $126.0 \pm 0.6$  GeV, compatible with CMS's results.

## Chapter 3

# Search for exclusive hadronic decays of the Higgs boson

This chapter constitutes the core of this dissertation. It explains the conducted analysis, beginning with a general overview, followed by an explanation of the samples, triggers, and object definitions. An entire section discusses the meson reconstruction techniques used, which are crucial to the analysis. Subsequently, it covers the criteria applied in event selection and describes how the signal and background have been modelled. Finally, it presents the expected upper limits of the branching ratio for each decay channel. These are  $H \rightarrow \phi\gamma$  with further  $\phi \rightarrow \pi^+\pi^-\pi^0$ ,  $H \rightarrow \omega\gamma$  with further  $\omega \rightarrow \pi^+\pi^-\pi^0$ ,  $H \rightarrow D^{*0}\gamma$  with further  $D^{*0} \rightarrow D^0\pi^0/\gamma$ ,  $D^0 \rightarrow K^-\pi^+$  and  $H \rightarrow D^{*0}\gamma$  with further  $D^{*0} \rightarrow D^0\pi^0/\gamma$ ,  $D^0 \rightarrow K^-\pi^+\pi^0$ .

This analysis represents an initial approach to compute these upper limits, and there are many more steps required to cross-check the methodology before attempting an actual measurement. Therefore, only an estimation using simulated data is computed. The chapter concludes by addressing the steps needed before data unblinding and obtaining the final experimental measurement, as well as suggesting ideas for optimizing and improving the results.

### 3.1 Analysis overview

This analysis uses data from proton-proton collisions corresponding to an integrated luminosity of  $39.54 \text{ fb}^{-1}$  at  $\sqrt{s} = 13 \text{ TeV}$ , collected by the CMS detector at the LHC in 2018 during Run 2. It does not target any specific production mode of the Higgs boson, but instead considers all production modes, which will be dominated mainly by gluon fusion ( $ggH$ ) with a minor contribution from vector boson fusion ( $VBF$ ). Nevertheless, it can be interesting to target specific production modes, as this can reduce background contamination by individually studying and applying dedicated techniques to each mode, and could be part of further extensions of this analysis. The decays under study are of the form  $H \rightarrow M\gamma$ , the mesons  $M$  are a  $\phi$ ,  $\omega$  and  $D^{*0}$ , each further decaying into two charged particles and a third (and fourth) neutral one, as shown in Table 6.

$$\begin{aligned}
H \rightarrow \phi\gamma, & \quad \phi \rightarrow \pi^+\pi^-\pi^0 \\
H \rightarrow \omega\gamma, & \quad \omega \rightarrow \pi^+\pi^-\pi^0 \\
H \rightarrow D^{*0}\gamma, & \quad D^{*0} \rightarrow D^0\pi^0/\gamma, D^0 \rightarrow K^-\pi^+ \\
H \rightarrow D^{*0}\gamma, & \quad D^{*0} \rightarrow D^0\pi^0/\gamma, D^0 \rightarrow K^-\pi^+\pi^0
\end{aligned}$$

**Table 6:** Higgs rare decays studied in this analysis.

Therefore, the final states of interest consist of an isolated and energetic photon, a charged meson pair, and photons compatible with a third (and sometimes fourth) neutral particle, with no additional leptons ( $e/\mu$ ).

The branching fractions of rare Higgs boson decays to a meson and photon can be computed using a factorization approach in QCD. The calculation considers both direct and indirect contributions, as explained in the first chapter and depicted in Figure 6. The interference between these components is significant, and in the SM, the indirect component dominates. Then, the Higgs boson couplings to light quarks are probed by searching for modifications in this branching fraction due to interference effects.

As previously explained, given the exotic nature of the decays under study, the theoretical decay widths being so small, and the large hadronic background at the LHC, we cannot aim for precise measurements of the branching fractions. Instead, the end goal of this thesis is to calculate expected upper limits on the branching ratios of the aforementioned Higgs boson decays, using Monte Carlo (MC) samples to model the SM expected signal. To obtain an actual measurement, this initial estimation requires further refinement and improvement, such as considering additional background sources or systematic uncertainties. A more extensive list is provided at the end of this chapter.

It is worth noting that this analysis and the one studying the three decays involving a  $\rho^0$ ,  $\phi$  and  $K^{*0}$  meson in the upper half of Table 4 are remarkably similar, and only differ by the consideration of neutral particles, which are more challenging to reconstruct than charged ones. The framework used for this analysis builds upon the existing framework for these simpler two-body decays currently under analysis by the CMS collaboration. To extend their study to include three-body decays involving neutral particles, our main focus has been on accurately recovering the missing neutral particles.

## 3.2 Samples and triggers

To develop this analysis, the data file format used is one designed by CMS, which is an extended version of NANO AOD. It is based on the official NANO AODv9 recipe and includes the reconstructed mesons, as described in Section 3.3, as additional objects. The NANO AOD format consists of an Ntuple-like structure used by CMS, which can be read using bare ROOT [68], and containing the per-event information that is needed in most generic analyses [69]. This analysis is performed using the ROOT data analysis framework, an open-source data analysis tool commonly used in high energy physics written mainly in C++.

### 3.2.1 Data and triggers

Events are selected from proton-proton collision data at a center-of-mass energy of  $\sqrt{s} = 13$  TeV and a bunch spacing of 25 ns, collected by the CMS experiment during the LHC’s Run 2 in 2018, corresponding to a total integrated luminosity of  $39.54 \text{ fb}^{-1}$ . Good run ranges and luminosity blocks are chosen based on criteria encoded in a golden JSON file.

To filter the events, a high-level trigger, named HLT\_Photon35\_TwoProngs35, is employed. This trigger selects a photon with  $p_T^\gamma > 35 \text{ GeV}$  and a ditrack system with  $p_T^{\text{jet}} > 35 \text{ GeV}$ , after passing through the L1 trigger, which also imposes rapidity restrictions of  $|\eta^\gamma| < 2.1$  and  $|\eta^{\text{jet}}| < 2.1$ . The trigger is applied to both data and MC. Introduced in 2018, this trigger recorded events enriched in gluon fusion production of the Higgs boson and VBF that were not registered by the dedicated trigger, providing an effective luminosity of  $39.54 \text{ fb}^{-1}$ . The datasets used in gluon fusion analysis, along with their integrated luminosities, are detailed in Table 7.

| Year | Dataset              | Integrated luminosity [ $\text{fb}^{-1}$ ] |
|------|----------------------|--|
| 2018 | /Tau/Run2018B-UL2018 | 0.67                                       |
| 2018 | /Tau/Run2018C-UL2018 | 6.94                                       |
| 2018 | /Tau/Run2018D-UL2018 | 31.93                                      |

Table 7: Datasets used in the gluon fusion analysis from the campaign MiniAODv2 of the MINIAOD data tier.

### 3.2.2 Background simulation

The background estimation will ultimately rely solely on data. However, in the early stage of this analysis, simulated samples are used to understand the background processes affecting the different selected final states. The main background process for the gluon fusion production mode is a single photon and jets, denoted as  $\gamma + \text{jets}$  throughout the analysis.

Every background event is generated at leading order (LO) precision using the MADGRAPH5 generator MG5\_aMC@NLO [70] and POWHEG [71], while PYTHIA8 [72] is used for the hadronization. For all simulations, the NNPDF 3.1 [73] next-to-next-to-leading-order (NNLO) parton distribution functions (PDFs) are used, while the modelling of the underlying event is generated using the CMS Pythia 5 (CP5) tunes [74]. The Run 2 legacy reconstruction algorithms [75] are used for all the MC and data samples. The campaign and global tag used to produce the background and signal MC samples are RunIIISummer20UL18MiniAODv2-106X and upgrade2018\_realistic\_v16\_L1v1, respectively. Table 8 summarizes the list of datasets used for the study along with their cross sections [76].

### 3.2.3 Signal simulation

The Higgs boson production modes used, ggH and VBF, are generated at next-to-leading order (NLO) using the POWHEGv2 event generator extended with the MiNLO procedure [78]. The production rates and kinematic distributions for the Higgs boson with  $m_H = 125 \text{ GeV}$  are assumed throughout. In particular, the cross section for ggH and VBF are computed at NNLO

| Monte Carlo name                                    | Cross section [pb]       |
|---|--------------------------|
| GJets_HT-40To100_TuneCP5_13TeV-madgraphMLM-pythia8  | 18540 (LO) $\times$ 1.26 |
| GJets_HT-100To200_TuneCP5_13TeV-madgraphMLM-pythia8 | 8644 (LO) $\times$ 1.26  |
| GJets_HT-200To400_TuneCP5_13TeV-madgraphMLM-pythia8 | 2183 (LO) $\times$ 1.26  |
| GJets_HT-400To600_TuneCP5_13TeV-madgraphMLM-pythia8 | 260.2 (LO) $\times$ 1.26 |
| GJets_HT-600ToInf_TuneCP5_13TeV-madgraphMLM-pythia8 | 86.58 (LO) $\times$ 1.26 |

**Table 8:** MC samples used to generate the  $\gamma + \text{jets}$  background. The normalization of  $\gamma + \text{jets}$  is scaled by 1.26 to account for higher-order contributions [77].

in QCD and NLO in electroweak accuracy, resulting in 48.58 pb and 3.78 pb, respectively, as provided by the LHC Higgs Cross Section Working Group in Ref. [24].

The decay of the Higgs boson is handled by Pythia, and it does not simulate direct and indirect effective vertices. The expected SM branching fractions of the Higgs rare decays are previously shown in Table 5. In the analysis, however, the branching ratios are set to

$$\mathcal{B}(\text{H} \rightarrow \phi\gamma) = \mathcal{B}(\text{H} \rightarrow \omega\gamma) = \mathcal{B}(\text{H} \rightarrow \text{D}^{*0}\gamma) = 1.$$

This is because when computing the upper limit, the obtained value is directly the measured upper limit of the branching ratio itself. If we were to set the branching fractions to the SM values, the measured quantities would be the signal strengths, i.e., the factors by which the observed fractions exceed the SM values. The branching fractions of the meson decays used are also shown in Table 4, but further detailed in Table 9.

| Meson decay channel                             | SM $\mathcal{B}$ (%) |
|---|----------------------|
| $\phi \rightarrow \pi^+ \pi^- \pi^0$            | $15.4 \pm 0.4$       |
| $\omega \rightarrow \pi^+ \pi^- \pi^0$          | $89.2 \pm 0.7$       |
| $\text{D}^{*0} \rightarrow \text{D}^0 \pi^0$    | $64.7 \pm 0.9$       |
| $\text{D}^{*0} \rightarrow \text{D}^0 \gamma$   | $35.3 \pm 0.9$       |
| $\text{D}^0 \rightarrow \text{K}^- \pi^+$       | $3.947 \pm 0.030$    |
| $\text{D}^0 \rightarrow \text{K}^- \pi^+ \pi^0$ | $14.4 \pm 0.5$       |

**Table 9:** Meson decay branching ratios used throughout the analysis, from the PDG [25].

### 3.3 Object definitions

This analysis primarily relies on photons and charged tracks to extract the final state signature of exclusive hadronic decays, while also making use of other physics objects such as additional leptons (or the lack thereof). All used objects, except the mesons, are discussed in this section, with the next section dedicated solely to meson reconstruction.

#### 3.3.1 Primary vertex

To consider an event, it must contain at least one primary vertex (PV), which is regarded as the vertex of the hard interaction. There should be a minimum of four tracks associated

with the selected primary vertex (from the Higgs boson, the photon and the ditrack system). For events with multiple selected vertices, the PV is chosen to be the vertex corresponding to the hardest scattering in the event, determined using tracking information alone, as described in Ref. [79].

### 3.3.2 Photons

Photon candidates are reconstructed as SuperCluster objects in the ECAL with  $E_T > 38$  GeV and  $|\eta^\gamma| < 2.1$  in both the barrel and endcap regions. In addition, photons have to satisfy the multivariate analysis (MVA) based selection identification (mvaID) criteria following the Fall117IsoV2 recipe [80]. For the production mode used, the mvaID provides 80% (90%) signal selection efficiency for the endcap (barrel) region. The mvaID criteria include photon isolation, charged hadron isolation, and requires photons to pass shower shape preselection cuts [81]. The photon's ECAL cluster must be inconsistent with charged particle tracks reconstructed in the silicon tracker to reject electrons faking photons, achieved using a conversion safe electron veto. Residual  $E_T$ -dependent photon energy scale and smearing corrections are applied. Additional photons with looser requirements ( $E_T > 20$  GeV and the WP90 version of the photonID) are also vetoed to reduce the potential contribution of diphotons. Table 10 summarizes the criteria for photon selection.

| Selection criteria ( $\gamma$ from PV) |           |
|--|-----------|
| $p_T^\gamma$                           | > 38 GeV  |
| $ \eta^\gamma $                        | < 2.1     |
| mvaID                                  | WP90/WP80 |
| electron Veto                          | Yes       |

Table 10: Selection criteria applied to the photon from the primary vertex.

An additional correction was attempted, involving shifting the photon's origin to that of the PV of the meson. This slight adjustment to the initial coordinates led to a minor change in the four-momentum variables of the photon, but it did not consistently reduce the discrepancy with the generation-level particle values. Consequently, it was discarded and not used.

## 3.4 Meson reconstruction

The  $\phi$ ,  $\omega$  and  $D^{*0}$  mesons decay products are reconstructed using charged particle tracks measured in the tracker, as well as energy deposited in the ECAL compatible with neutral particles coming also from the PV. For the  $\phi$  and  $\omega$  mesons, the targeted charged ditrack is  $\pi^\pm\pi^\mp$ , while for the  $D^{*0}$  meson the charged ditrack is  $K^-\pi^+$ .

In the following sections, the term *ditrack system* will refer to the system of the two charged tracks. Even though they not form a real particle, notions like ditrack mass will be used (understood as the mass component of the sum of the four-momenta of both tracks). To refer to the meson originating from the PV, namely  $\phi$ ,  $\omega$  and  $D^{*0}$ , terms like *meson* or *full meson* will be used, emphasizing that the neutral particles have been accounted for. Some

considerations have been made to precisely reconstruct the full meson, as described in the following subsections.

### 3.4.1 Track selection

To be selected, the tracks need to satisfy a “high purity” reconstruction criteria, which considers the number of tracker layers with hits, track fit quality, and the impact parameter values relative to their uncertainties. For a detailed description of the algorithm, refer to Ref. [82].

### 3.4.2 Meson decay vertex

The meson decay vertex is determined using the standard CMSSW [83] kinematic vertex fitting package, as described in Ref. [84]. Using the candidate’s decay vertex and its associated momentum, a newly fitted transient track is constructed to represent the meson candidate. Then, for each primary vertex, the track is extrapolated to the nearest point in 3D space. The meson vertex’s longitudinal distance is required to be within 24 cm from the centre of the detector.

### 3.4.3 Isolation

To ensure good track selection, a dedicated isolation criterion of the candidate based on the tracks is used. This dimensionless isolation parameter ( $\text{Iso}$ ) is determined from the meson’s momentum and other tracks within a cone of radius  $\Delta R = 0.3$  around the ditrack system’s direction. Only tracks with  $p_T > 0.9$  GeV associated with the same meson vertex are considered, excluding the charged-hadron candidates that define the ditrack. The definition is as follows:

$$\text{Iso} = \frac{p_T^{\text{meson}}}{p_T^{\text{meson}} + \sum_{\text{trk}} |p_T^{\text{trk}}|}$$

A high isolation value will be required to consider a meson candidate (over 0.9).

### 3.4.4 Photons from the neutral particle decays

For each selected ditrack, up to two photons with  $p_T > 5$  GeV are recovered in a small cone of  $\Delta R = 0.05$  ( $\Delta R = 0.10$  for  $D^{*0}$  three-body channel) around the ditrack direction. These photons account for the recovery of neutral particles, as  $\pi^0 \rightarrow \gamma\gamma$  in  $\sim 98.8\%$  with  $c\tau = 25$  nm [25], so their origin can be considered the same as that of the meson decay. Generation-level MC reveals that photons coming from neutral particle decays that in turn come from the three-body decays are very collimated with the ditrack system. In the case of the  $\phi/\omega$  channels and the  $D^{*0}$  channel when  $D^0$  decays into three bodies, these photons directly originate from the  $\pi^0$  of the three-body decay. In the case of the  $D^{*0}$  channel, additional photons come either directly from  $D^{*0} \rightarrow D^0\gamma$  or from the decay of the  $\pi^0$  from  $D^{*0} \rightarrow D^0\pi^0$ . Unlike the photons described in Section 3.3.2, these photons are not corrected for discrepancies between data and MC. This adjustment is necessary for precise measurements.

### 3.4.5 Ditrack mass hypothesis

The invariant mass of the refitted ditrack system is also used to reduce contamination from background events. The mass of the pair, assuming the charged-pion hypothesis for the two tracks, is coherent with the charged components of the  $\phi$  and  $\omega$  mesons. Since the ditrack system is not a real resonance, its mass is very wide but consistent and useful for reducing background events. In the case of the  $D^{*0}$  channel, two scenarios are considered. On the one hand, when  $D^0$  decays into a pair of charged particles (kaon-pion) the ditrack system's invariant mass is a real narrow resonance (i.e.,  $D^0$ ) consistent with the mass of that meson. On the other hand, when  $D^0$  decays into a pair of charged particles and a neutral pion, one finds the same scenario as for the  $\phi/\omega$  decay channels.

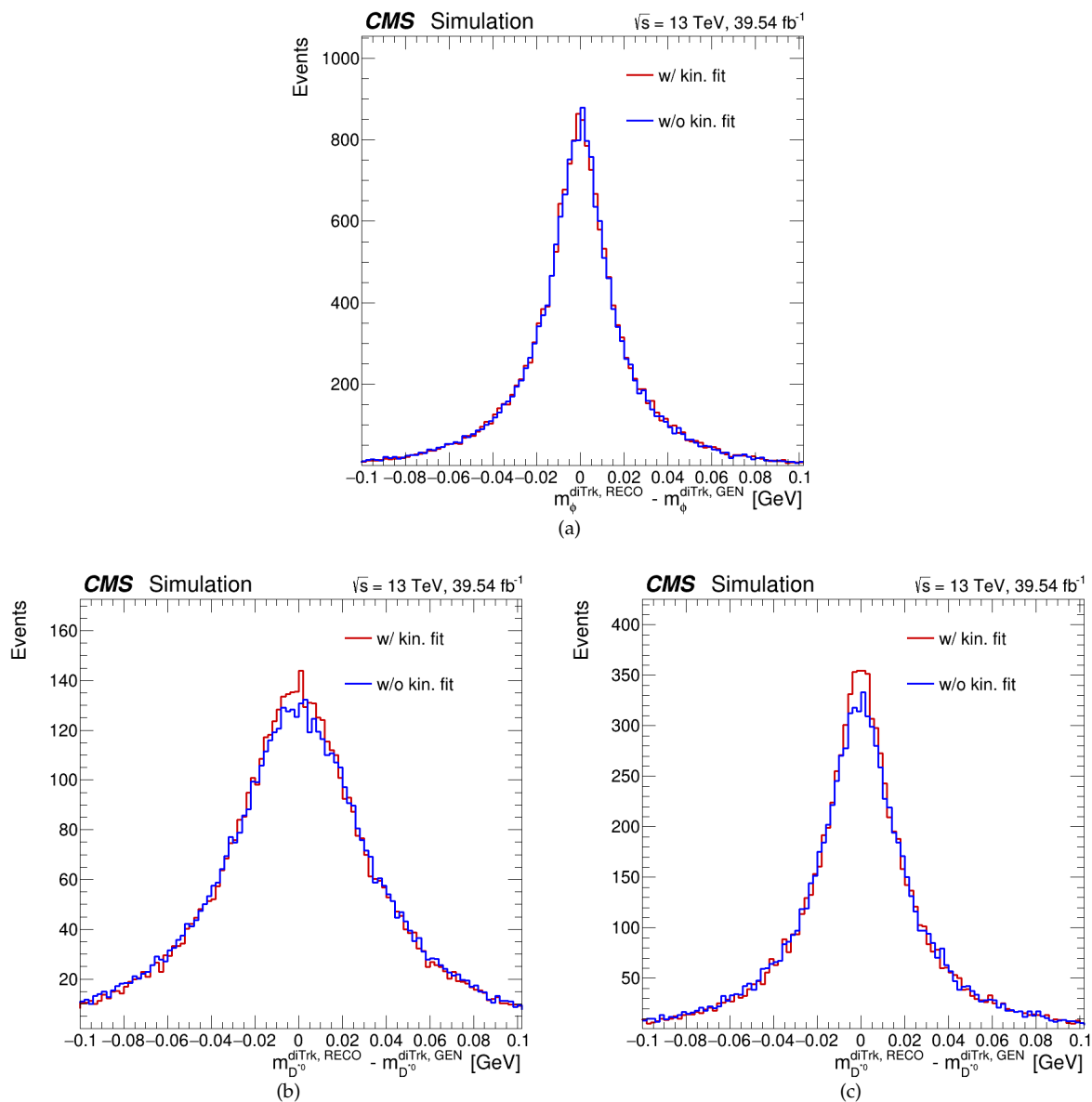


**Figure 13:** Ditrack mass residuals with (red) and without (blue) kinematic fits for the different decay channels. (a) is for  $\phi$ , (b) is for  $D^{*0}$  2-body, and (c) is for  $D^{*0}$  3-body.

The exact used selection criteria will be presented at the end of this section, but it is worth noting that for the  $\phi/\omega$  three-body decays involving a  $\pi^0$ , the mass of the ditrack is approximately two-thirds of the full meson's mass (each pion carries roughly a third of the energy).

Furthermore, instead of recovering the ditrack invariant mass by only retrieving the mass component of the sum of both four-momenta, the CMSSW [83] kinematic fit has been employed. To study the performance of this fit, it is useful to define the *residual* as the difference between the reconstructed values and the corresponding generation-level ones. Figure 13 displays the residual of the ditrack invariant mass reconstruction with (red) and without (blue) the kinematic fits with vertex constraint for the decay modes involving  $\phi$  or  $D^{*0}$  mesons. Table 11 shows the root mean squared errors (RMSE) with respect to generation-level, both with and without the kinematic fit, for each channel involving  $\phi$  or  $D^{*0}$  mesons. Applying the kinematic fit improves the reconstructed ditrack invariant mass values for all channels. The  $\omega$  decay channel behaves identically to the  $\phi$  channel.

| Decay channel   | RMSE without kinematic fit | RMSE with kinematic fit |        |
|-----------------|----------------------------|-------------------------|--------|
| $\phi$          | 37.4 MeV                   | 33.3 MeV                | (-11%) |
| $D^{*0}$ 2-body | 51.7 MeV                   | 49.8 MeV                | (-4%)  |
| $D^{*0}$ 3-body | 50.3 MeV                   | 40.8 MeV                | (-19%) |

**Table 11:** Root mean squared errors (RMSE) with and without the kinematic fit for each decay mode. In all decay modes the kinematic fit improves the reconstructed ditrack mass value.

### 3.4.6 Meson mass hypothesis

The simplest way to reconstruct the four-momentum of the full meson is by summing the four-momenta of the ditrack system and those from the photons compatible with the decay of neutral particles. This approach was initially used for all channels. Nevertheless, for the  $\phi$ ,  $\omega$  and  $D^{*0}$  3-body decay channels, additional corrections were applied.

Consider that the photons in the  $\Delta R$  cone come from the  $\pi^0 \rightarrow \gamma\gamma$  decay. When only one photon is recovered, either both photons ended up in the same ECAL crystal, or that one of them was too soft to be measured ( $p_T < 5$  GeV) and therefore only one is detected. Following the first hypothesis, one can interpret the energy deposited in the same ECAL cell as the energy from the full pion. To account for this, whenever only one photon is recovered, we assign this object a non-zero mass (the pion's mass) before adding the four-momenta. This correction is of very low energy, and thus the changes in  $p_T$ ,  $\eta$  or  $\phi$  of the full meson are imperceptible, but its mass is visibly affected. Figure 14 and Table 12 show the residual of the full meson invariant mass reconstruction and the RMSE, respectively, with (red) and without (blue) the  $\pi^0$  mass correction for the  $\phi$  and  $\omega$  decay modes.

This slight improvement will enable us to narrow the selection cuts and reduce more background events, ultimately improving the final result. It will also contribute to the modelling of the signal, as explained in Section 3.7, where the mass of the full meson will play a pivotal role.

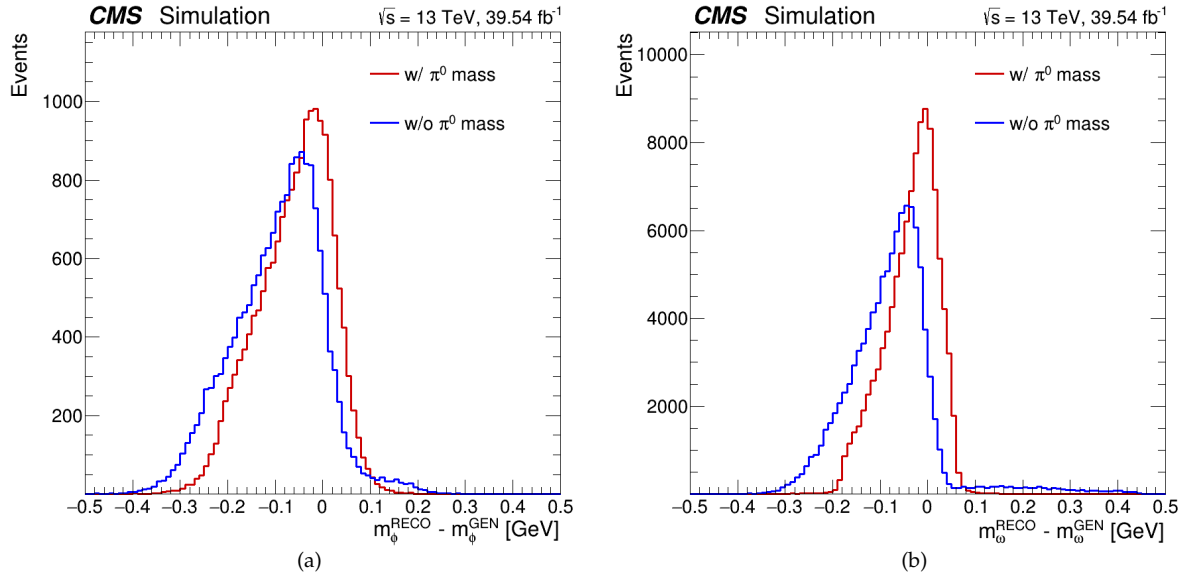


**Figure 14:** Full meson mass residuals for the different decay channels. (a) is for  $\phi$ , (b) is for  $\omega$ . The residuals shown in red are including the  $\pi^0$  mass, and in blue without the correction.

| Decay channel   | RMSE without $m_{\pi^0}$ correction | RMSE with $m_{\pi^0}$ correction |
|-----------------|-------------------------------------|----------------------------------|
| $\phi$          | 95.4 MeV                            | 78.7 MeV (-17%)                  |
| $\omega$        | 95.2 MeV                            | 55.7 MeV (-42%)                  |
| $D^{*0}$ 3-body | 120.4 MeV                           | 97.2 MeV (-19%)                  |

**Table 12:** Root mean squared errors with and without the  $m_{\pi^0}$  correction for the  $\phi$  and  $\omega$  decay modes.

An additional correction was attempted. The idea was to reconstruct the neutral particle by summing the recovered photons, and then forcing the reconstructed neutral particle to have the  $\pi^0$ 's mass while maintaining the energy and direction ( $\eta$  and  $\phi$ ) unchanged. This required a slight modification of the neutral particle's transverse momenta, as given by

$$p_T = \sqrt{(E^2 - m^2)(1 - \tanh^2 \eta)} .$$

When adding this neutral particle to the ditrack, the full meson's  $p_T$  remained effectively unchanged, and the full meson's mass was very similar (and slightly worse) compared to using the previous technique. Therefore, this adjustment was not used.

### 3.4.7 Full meson transverse momentum

To calculate the upper limits of the branching ratios of the decays, the Higgs boson invariant mass  $m_{\gamma,M}^H$  is computed. This is done by extracting the mass component of the sum of the four momenta of the photon and the full meson. If  $m_{\gamma,M}^H$  exhibits a narrow peak around the Higgs boson mass ( $m_H = 125$  GeV), it is a strong indication that these particles were produced from the Higgs boson. To achieve a good resolution on  $m_{\gamma,M}^H$ , it is crucial to recover the two involved objects, i.e., the photon and the full meson, with utmost precision.

There are seven variables in play: the components of the four-momenta, four of which belong to the meson and three to the photon. The accuracy of the Higgs boson's invariant

mass relies mainly on the accuracy of the transverse momenta of both particles involved. The other five variables ( $\eta$  and  $\phi$  of both particles and the mass of the full meson) are either already well measured or, in the case of the mass, too low in energy to significantly impact the computation. The corrections on the photon's transverse momentum of the photon are already discussed in Section 3.3.2. Thus, the main emphasis should be on recovering the  $p_T$  of the full meson as precisely as possible.

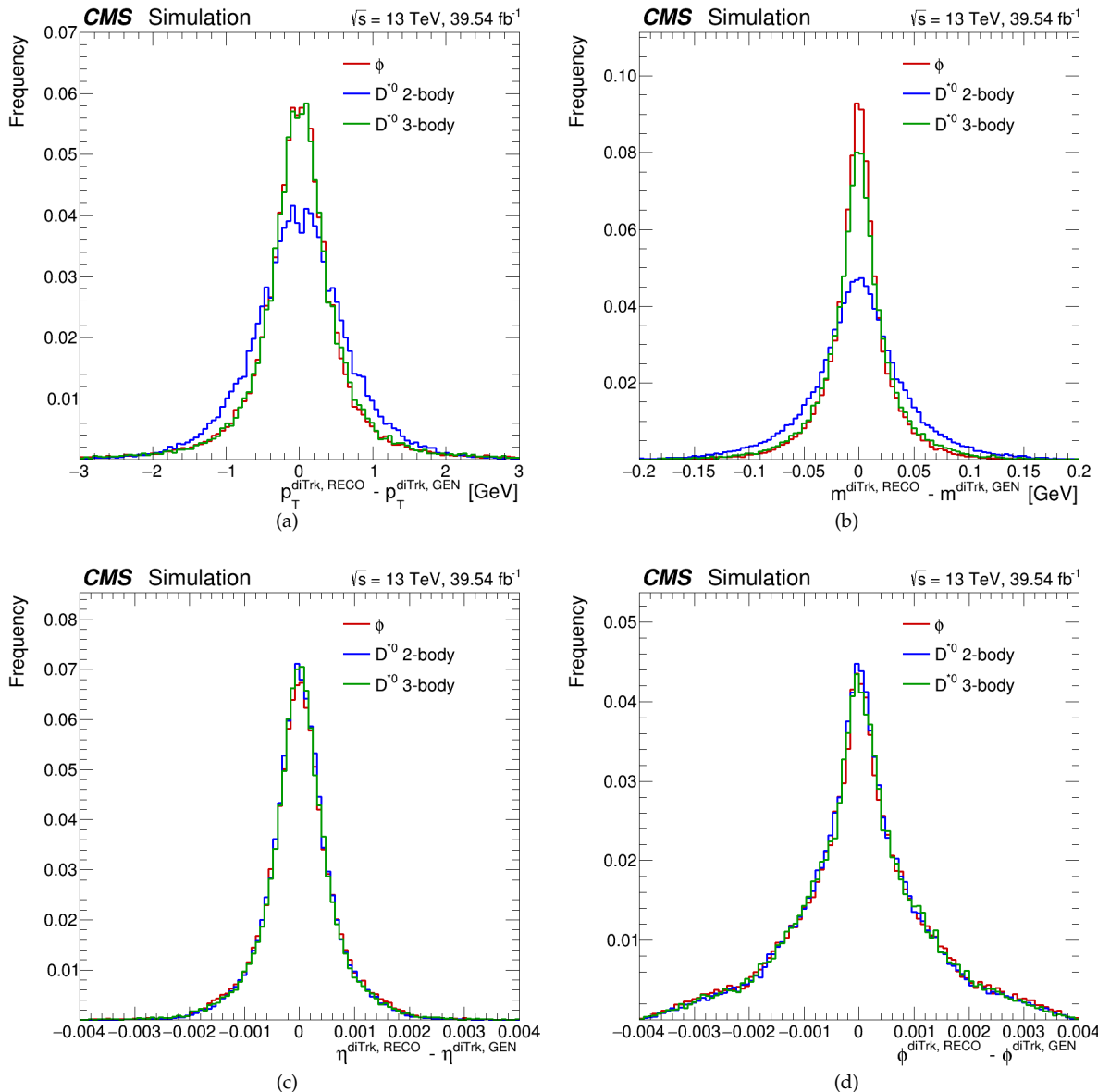


**Figure 15:** Ditrack residuals for the different four-momentum components of each decay channel. (a) is for  $p_T$ , (b) is for the ditrack mass, (c) is for  $\eta$ , and (d) is for  $\phi$ . Three decay modes are shown: the  $\phi$  in red, the  $D^{*0}$  2-body in blue, and the  $D^{*0}$  3-body in green. The  $\omega$  ditrack residuals behave the same as the  $\phi$  channel. All the residuals have been normalized to the same area to ease the comparison.

In each decay channel, the ditrack system variables are measured with remarkable accuracy. Figure 15 displays the residuals of the ditrack transverse momentum, mass,  $\eta$  and  $\phi$  with respect to their generation-level MC value for every decay mode.

All histograms are normalized to the same area for comparing the various channels. It is worth noting that, as the ditrack consists of a pair of charged tracks that can be precisely determined thanks to the silicon tracker, the direction –  $\eta$  and  $\phi$  – is accurately measured for all channels.

The initial approach to reconstruct the full meson's transverse momentum is to sum the four-momenta of the ditrack system and those from the photons compatible with the decay of neutral particles. The main source of discrepancy between the full meson's transverse momenta and their generation-level MC values arises from the poorly reconstructed neutral particles. Given that the pions decay into softer photons that are hard to recover, many events exhibit missing energy, resulting in the full meson's  $p_T$  being generally less energetic than expected. Figure 16 shows the residuals of the full meson's transverse momentum with respect to their generation-level MC value for each decay mode. Both the  $\phi$  and  $\omega$  channels exhibit an

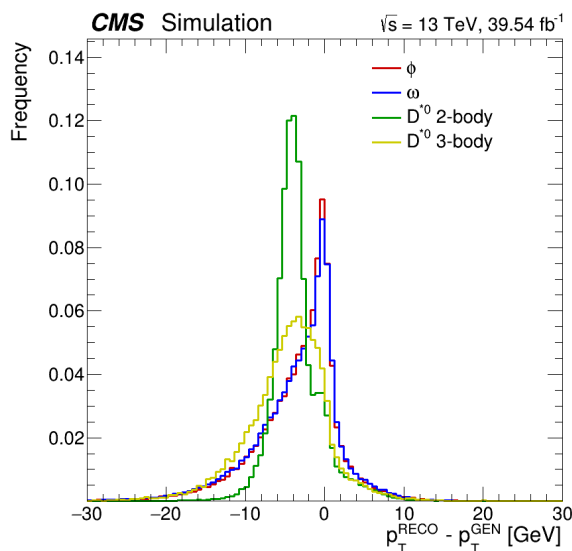


**Figure 16:** Transverse momentum residuals for the full meson for each decay channel. All studied decay modes are shown: the  $\phi$  in red, the  $\omega$  in blue, the  $D^{*0}$  2-body in green, and the  $D^{*0}$  3-body in yellow. All the residuals have been normalized to the same area to ease the comparison.

asymmetric left shoulder, consistent with the hypothesis of missing energy from the neutral particle. The  $D^{*0}$  2-body, on the other hand, is more symmetric but displaced about 5 GeV, since the soft  $\pi^0/\gamma$  from  $D^{*0} \rightarrow D^0\pi^0/\gamma$  typically carries around  $\sim 5$  GeV in energy. The right shoulder results from events in which one photon compatible with this missing neutral particle is reconstructed, which is only around  $\sim 13\%$  of events. The  $D^{*0}$  3-body combines characteristics from all previous channels, and since it is missing two neutral particles, it is noticeably shifted towards the lower end of the axis.

### 3.4.8 Meson momentum regression

To address this issue, dedicated Boosted Decision Trees (BDTs) have been implemented for each channel using the Toolkit for Multivariate Data Analysis for ROOT [68], also known as TMVA [85]. This machine learning (ML) technique will correct for the full meson's  $p_T$ . A boosted decision tree is a ML binary classifier or regressor algorithm based on a flowchart-like

structure in which each internal node represents a test on an attribute, each branch signifies the test's outcome, and each leaf node denotes a class level. For more detailed information, refer to Refs. [85,86].

The variables used in all models are presented in Table 13. The variables labelled by  $\gamma_1$

| Regression input variables                     |                         |   |
|--|-------------------------|---|
| Dimensionless                                  | Dimensionful            | Normalised                                |
| $\Delta R^{\gamma_1, \text{diTrk}}$            | $p_T^{\gamma_1}$        | $p_T^{\text{meson}} / p_T^{\gamma}$       |
| $\Delta R^{\gamma_2, \text{diTrk}} (*)$        | $p_T^{\gamma_2} (*)$    | $p_T^{\text{meson}} / p_T^{\text{diTrk}}$ |
| $\eta^{\text{diTrk}}$                          | $m^{\text{diTrk}}$      |   |
| $\Delta R^{\text{diTrk}}$                      | $m^{\text{meson}} (**)$ |   |
| $\Delta(\eta^{\gamma_H}, \eta^{\text{diTrk}})$ |                         |   |
| $\Delta(\phi^{\gamma_H}, \phi^{\text{diTrk}})$ |                         |   |

**Table 13:** Input variables for the BDTs.  $\gamma_1$  and  $\gamma_2$  represent photons from neutral particle decay,  $\gamma_H$  stands for the Higgs boson decay photon. The single asterisk denotes exclusion for the  $\phi/\omega$  decay channels. The double asterisk denotes exclusion for the  $D^{*0}$  2-body decay channel.

and  $\gamma_2$  refer to the recovered photons compatible with the decay of the neutral particles, while  $\gamma_H$  refers to the photon originating in the Higgs boson decay. The dimensionless variables  $\Delta R^{\gamma_1, \text{diTrk}}$  and  $\Delta R^{\gamma_2, \text{diTrk}}$  reference the angular separation between each photon and the ditrack system.  $\Delta R^{\text{diTrk}}$  is the angular separation within the track pair. It is worth defining  $\Delta(\eta^{\gamma_H}, \eta^{\text{diTrk}})$  and  $\Delta(\phi^{\gamma_H}, \phi^{\text{diTrk}})$ ,

$$\begin{aligned}\Delta(\eta^{\gamma_H}, \eta^{\text{diTrk}}) &= \eta^{\text{diTrk}} - \eta^{\gamma_H} \\ \Delta(\phi^{\gamma_H}, \phi^{\text{diTrk}}) &= (\phi^{\text{diTrk}} - \phi^{\gamma_H}) \bmod 2\pi \in [0, 2\pi] .\end{aligned}$$

The definition of  $\Delta(\phi^{\gamma_H}, \phi^{\text{diTrk}})$  takes this form due to the periodic nature of the angular variable  $\phi$ . The single asterisk (\*) next to the variables related to the  $\gamma_2$  indicates that they are not used for the  $\phi/\omega$  decay channels, as the required selection criteria for these decay modes specify only one photon. Similarly, the double asterisk (\*\*) next to the full meson's mass indicates that this variable is not included for the  $D^{*0}$  2-body decay, as in this channel,  $m^{\text{meson}}$  is not very precisely determined. The variables in Table 13 have been selected after many model iterations, ensuring low correlation between them and with the Higgs boson invariant mass, while maintaining reasonable predictive power.

All the models have been trained to predict not the correct value of the full meson's transverse momentum, but a scale factor  $p_T^{\text{meson, GEN}} / p_T^{\text{meson, RECO}}$  instead. This scale factor represents the adjustment needed for the reconstructed  $p_T$  to match its generation-level MC value. The motivation for this approach is to avoid biasing the model by predicting a dimensionless variable.

We implemented the BDTs using the TMVA framework, specifically the

```
TMVA::Factory.BookMethod(dataloader, TMVA::Types::kBDT, "modelName", "<options>");
```

method, with the ML regressor `TMVA::Types::kBDT`. To prevent overtraining, we employed cross-validation by rotating the training and testing samples. Specifically, the signal MC was divided into three subsets: A, B, and C. Three models with identical hyperparameters were

trained on A+B (B+C / C+A) and tested on C (A / B). This approach ensures all the available data is used to train the models, while testing them on signal MC that was not used for training. To recover all the signal events, these three models were then applied to their respective testing subsets. Afterward, all the subsets were combined once more, resulting in a complete set of events.

The hyperparameters for each model are available in Table 22 in the Appendix. Figures 17 and 18 compare the generation-level MC transverse momentum with the reconstruction values, both with and without regression, and show the residuals for each channel.

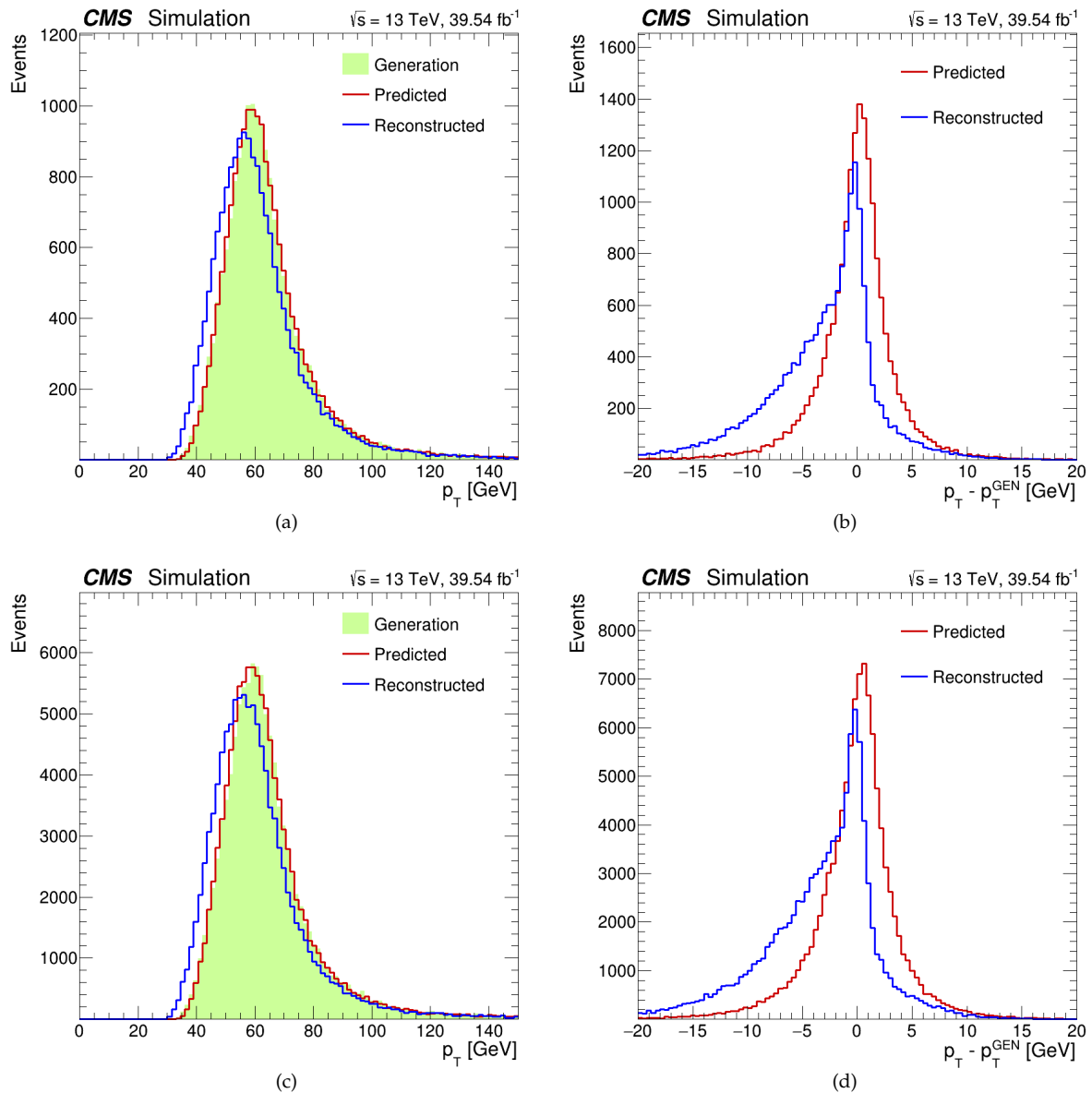


**Figure 17:** Transverse momentum of the  $\phi$  and  $\omega$  mesons. (a/c) Display the generation-level MC transverse momenta in green, the prediction by the BDT in red, and the recovery by the initial approach in blue, for the  $\phi/\omega$  mesons, respectively. (b/d) Show the residuals with (red) and without (green) the BDT prediction, for the  $\phi/\omega$  mesons, respectively.

Both  $\phi/\omega$  channels displayed in Figure 17 are quite similar. For both full mesons, the predicted transverse momentum spectrum aligns well with the generation-level one. Addi-

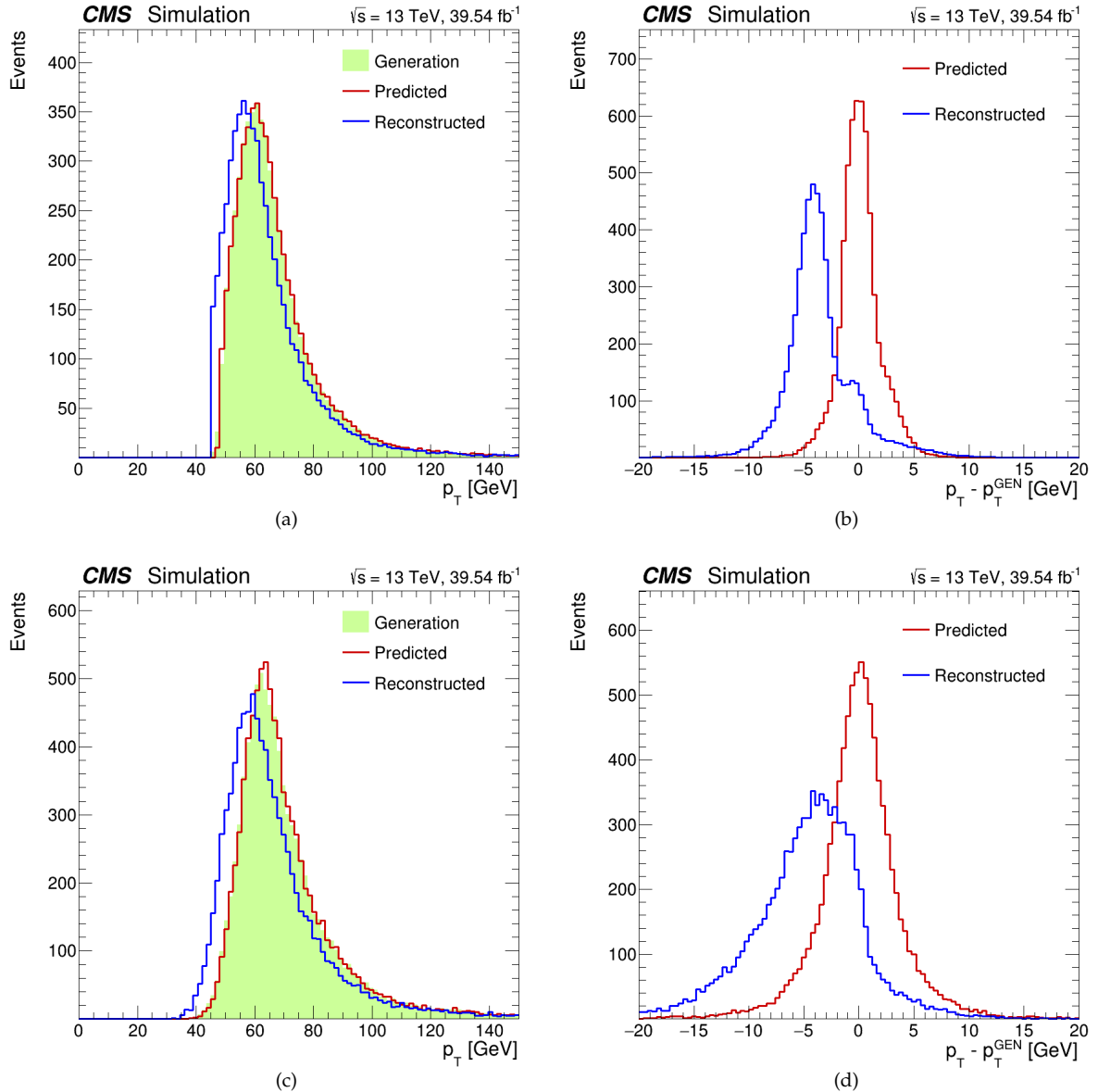


**Figure 18:** Transverse momentum of the  $D^{*0}$  meson in both the 2-body and 3-body decay channels. (a/c) Display the generation-level MC transverse momenta in green, the prediction by the BDT in red, and the recovery by the initial approach in blue, for the 2/3-body decay channel, respectively. (b/d) Show the residuals with (red) and without (green) the BDT prediction, for the 2/3-body decay channel, respectively.

tionally, the residuals for the predicted values are centred around the origin and symmetric, indicating that the predicted  $p_T$  no longer exhibits missing energy. They are also higher around the origin than the reconstructed residuals, meaning that the predicted values are closer to the generation-level ones than the reconstructed  $p_T$ 's. The 2-body decay channel presented in Figure 18 shows that the model accurately shifts the full meson transverse momentum by around 5 GeV, as the residuals are narrow around 0 GeV instead of around -5 GeV, and it is also more symmetric than the initially reconstructed  $p_T$ . The 3-body decay channel shown in Figure 18 has the poorest transverse momentum reconstruction before the BDT, but shows a significant improvement after applying the regression. Similar to the other channels,

the residuals are centred, symmetric and with a higher maximum near the origin.

Table 14 quantifies these improvements and shows the root mean squared errors with respect to generation-level transverse momentum, both with and without the BDT regression, for each channel. Applying the transverse momenta regression noticeably improves the  $p_T$  values and reduces the error for all channels by around 20% - 40%. The applied BDTs not

| Decay channel   | RMSE without $p_T$ regression | RMSE with $p_T$ regression |        |
|-----------------|-------------------------------|----------------------------|--------|
| $\phi$          | 4.908 GeV                     | 3.641 GeV                  | (-26%) |
| $\omega$        | 5.014 GeV                     | 3.890 GeV                  | (-22%) |
| $D^{*0}$ 2-body | 3.216 GeV                     | 1.927 GeV                  | (-40%) |
| $D^{*0}$ 3-body | 4.846 GeV                     | 3.769 GeV                  | (-22%) |

**Table 14:** Root mean squared errors of the full meson's transverse momentum with and without the BDT regression for each decay mode.

only significantly reduce the error in the transverse momentum of the full meson for every channel but also restore the symmetric residual shape of the variable. This indicates that the estimated  $p_T$  values are as likely to be underestimated as to be overestimated, accounting for the missing energy from the undetected neutral particles. This reduction in the width of the residuals will directly lead to an improved, lower upper limit on the Higgs boson branching fraction.

A crucial consideration in developing any ML model is overtraining, and this case is no exception. This is the primary reason a dimensionless scale factor was predicted rather than the direct value of the momentum. In this situation, overtraining can be directly detected by examining the background shape after applying the regression. If the model learns that, regardless of the input, the predicted value should lead to a peak around 125 GeV when constructing the Higgs invariant mass variable, we know it is overtrained and biased and needs to be rejected. To address this potential issue, a *background shaping function* (BSF) was introduced, providing a dimensionless metric that increases as the model becomes more biased. The developed BSF for measuring each model is defined to be

$$BSF \propto -A \log(\mu - 125)^2 + BN + C\sqrt{b},$$

where  $A$ ,  $B$ , and  $C$  are constants,  $\mu$  is the peak of a fitted double-sided Crystal Ball<sup>2</sup> (CB) to the Higgs boson's invariant mass constructed from background MC events,  $N$  is the normalization constant of the Crystal Ball, and  $b$  is the number of events in the interval (117, 133) GeV of the Higgs boson's invariant mass. Note that the BSF depends only on background events, more particularly in reconstructing the Higgs boson's invariant mass. The first factor penalizes the model more when the background Higgs boson's invariant mass shape peaks around  $m_H = 125$  GeV, because the background should be flat or asymptotically falling near that value. The remaining two factors account for the number of background events near the expected signal peak. More background events result in a smaller and thus worse signal-to-background ratio, a quantity to maximize for improving the computation of upper limits.

<sup>2</sup>A double-sided Crystal Ball function, named after the Crystal Ball Collaboration [87], is a probability density function (PDF) commonly used in high-energy physics (HEP). It is built from a Gaussian centre and two asymmetric tails modelled by power-law functions. Additional details about this PDF and its implementation in ROOT can be found in Ref. [88].

Figure 19 shows the BSF as a function of the RMSE of different models applied to reconstruct the transverse momentum of the  $\phi$  meson. The studied models follow an expected

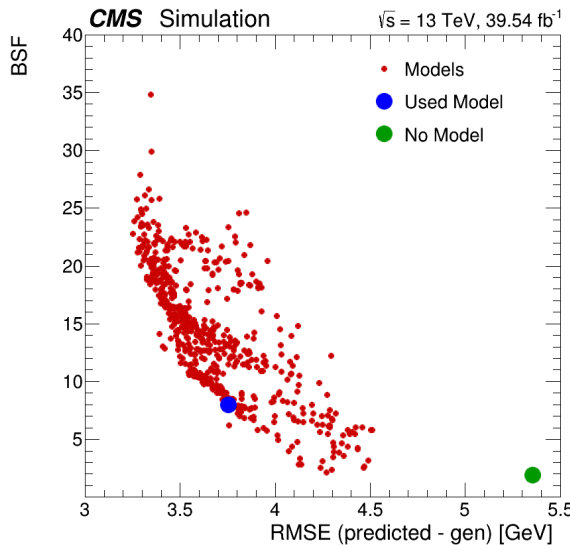


**Figure 19:** Background shaping function (BSF) as a function of the root mean squared error (RMSE) of the  $p_T$  for various models of the  $\phi$  decay channel. The reconstructed and the explored and used model's values are shown in blue, green and red, respectively. The explored models follow an expected trend: as the BSF increases (the model becomes more biased), the RMSE decreases, a sign of overtraining.

trend: as the BSF increases, and consequently, the model becomes more biased, the RMSE decreases. All decay channels have a similar behaviour, so only the  $\phi$  channel is shown. To select one model from the many tens of thousands that were tested, compromises must be made, as there is a trade-off between not shaping the background and significantly improving the error. Different BSF thresholds for each decay channel were identified, considering that each decay involves a different number of events, directly related to the BSF values. Thus, it is not meaningful to compare BSF values across channels; it is only relevant to compare them within a single channel. For the  $\phi$  decay channel, a value of around 8 was found to be optimal by directly examining the shape of the background Higgs boson's invariant mass.

### 3.4.9 Meson selection criteria

After having presented all the techniques for reconstructing the meson, some selection cuts can be applied. These aim to preserve the maximum number of signal events while rejecting as many background events. Tables 15 and 16 summarize the meson candidate selection criteria used for each decay channel, where  $\gamma^{\text{diTrk}}$  are the photons from neutral particle decays, and  $\gamma_H$  refers to the photon originating from the Higgs boson decay.

In most of the events the full meson and the photon are back-to-back, so  $\Delta(\phi^{\text{diTrk}}, \phi^{\gamma_H})$  is centred around  $\pi$ . We select highly isolated particles as this significantly reduces background contribution.

| Variable                                       | $\phi(\pi^\pm\pi^\mp\pi^0)$ | $\omega(\pi^\pm\pi^\mp\pi^0)$ |
|--|-----------------------------|-------------------------------|
| Meson mass                                     | 0.80 – 1.08 GeV             | 0.60 – 0.84 GeV               |
| Ditrack mass                                   | 0.37 – 0.82 GeV             | 0.33 – 0.62 GeV               |
| $p_T^{\text{diTrk}}$                           | $> 25 \text{ GeV}$          | $> 25 \text{ GeV}$            |
| $p_T^{\text{leadTrk}}$                         |                             |                               |
| $p_T^{\text{subLeadTrk}}$                      |                             |                               |
| # $\gamma^{\text{diTrk}}$                      | $> 0$                       | $> 0$                         |
| $\Delta(\phi^{\text{diTrk}}, \phi^{\gamma_H})$ | $\pi \pm 2.44$              | $\pi \pm 2.44$                |
| $\Delta(\eta^{\text{diTrk}}, \eta^{\gamma_H})$ | $0 \pm 1.8$                 | $0 \pm 1.8$                   |
| Iso  | $> 0.95$                    | $> 0.95$                      |

**Table 15:** Selection criteria applied to the  $\phi$  and  $\omega$  mesons used in the analysis.

| Variable                                       | $D^{*0}(K^-\pi^+(\pi^0/\gamma))$ | $D^{*0}(K^-\pi^+\pi^0(\pi^0/\gamma))$ |
|--|----------------------------------|---------------------------------------|
| Meson mass                                     |                                  | 1.60 – 2.00 GeV                       |
| Ditrack mass                                   | 1.82 – 1.91 GeV                  | 0.60 – 1.75 GeV                       |
| $p_T^{\text{diTrk}}$                           | $> 45 \text{ GeV}$               | $> 25 \text{ GeV}$                    |
| $p_T^{\text{leadTrk}}$                         |                                  |                                       |
| $p_T^{\text{subLeadTrk}}$                      | $> 10 \text{ GeV}$               | $> 6 \text{ GeV}$                     |
| # $\gamma^{\text{diTrk}}$                      |                                  | $> 0$                                 |
| $\Delta(\phi^{\text{diTrk}}, \phi^{\gamma_H})$ | $\pi \pm 2.44$                   | $\pi \pm 2.44$                        |
| $\Delta(\eta^{\text{diTrk}}, \eta^{\gamma_H})$ | $0 \pm 1.8$                      | $0 \pm 1.8$                           |
| Iso  | $> 0.95$                         | $> 0.95$                              |

**Table 16:** Selection criteria applied to each channel of the  $D^{*0}$  meson decay used in the analysis.

## 3.5 Event selection

The analysis described here searches for the Higgs boson decaying to a photon and to either a  $\phi$ ,  $\omega$  or  $D^{*0}$  meson. The signal features narrow peaks in the ditrack's mass (for the  $D^{*0}$  2-body decay), the full meson's mass (for the  $\phi$ ,  $\omega$  and  $D^{*0}$  3-body decays), and the photon-meson invariant mass  $m_{\gamma,M}^H$  distributions over the SM backgrounds. These resonances can be fully reconstructed thanks to the excellent resolution of the CMS detector in measuring of the photon energy and track momentum. Nevertheless, the accuracy of these three-body decays is not as good as in other exotic Higgs boson decays of the same type, but where the vector meson decays only into a pair of charged tracks.

The  $\phi\gamma$ ,  $\omega\gamma$  and  $D^{*0}\gamma$  exclusive final states are very similar. Meson candidates are paired with photon candidates to form  $M\gamma$  candidates. When multiple photon candidates meeting the selection criteria outlined in Section 3.3 are present, the one with the highest transverse momentum is chosen. Similarly, when multiple meson candidates satisfying the selection criteria described in Section 3.4.9 are found, the one with a mass closest to the theoretical mass value of the meson is chosen.

The  $\phi\gamma$  and  $\omega\gamma$  channels in particular closely resemble each other, both decaying into  $\pi^+\pi^-\pi^0$  and having similar masses and decay widths. The  $D^{*0}$  2-body decay can effectively

be treated as a three-body decay,  $D^{*0} \rightarrow K^- \pi^+ \pi^0 / \gamma$ , due to its short lifetime. The main difference between this channel and the  $\phi/\omega$  channel is that in the  $\phi/\omega$  case, the three pions carry, on average, approximately the same energy, while for  $D^{*0}$  the neutral particle is very soft, carrying only around 5 GeV. Finally, the  $D^{*0}$  3-body decay can effectively be treated as a 4-body decay for the same reason, with 2 charged tracks, one soft neutral particle, and one neutral pion. This last case shares similarities with the previous ones.

To reduce the number of background events while maintaining a lot of events from ggH and VBF, only the lepton veto was applied, discarding events with additional charged leptons with  $p_T > 10$  GeV.

Table 17 reports the signal cut flow. The product of signal selection efficiency and acceptance ( $\epsilon A$ ) corresponds to the fraction of MC simulated signal events that pass the selection. The efficiencies for the  $\phi$  and  $\omega$  channels are consistently similar throughout the selection

| Selection               | $H \rightarrow \phi\gamma$ | $H \rightarrow \omega\gamma$ | $H \rightarrow D^{*0}\gamma$ (2-body) | $H \rightarrow D^{*0}\gamma$ (3-body) |
|-------------------------|----------------------------|------------------------------|---------------------------------------|---------------------------------------|
| trigger                 | 24%                        | 23%                          | 17%                                   | 19%                                   |
| 1 good $\gamma$         | 89%                        | 90%                          | 89%                                   | 90%                                   |
| 1 good meson            | 33%                        | 36%                          | 55%                                   | 25%                                   |
| 0 leptons               | 99%                        | 98%                          | 99%                                   | 99%                                   |
| Cumulative $\epsilon A$ | 7.0%                       | 7.4%                         | 8.2%                                  | 4.2%                                  |

Table 17: Signal selection efficiency for all decay channels.

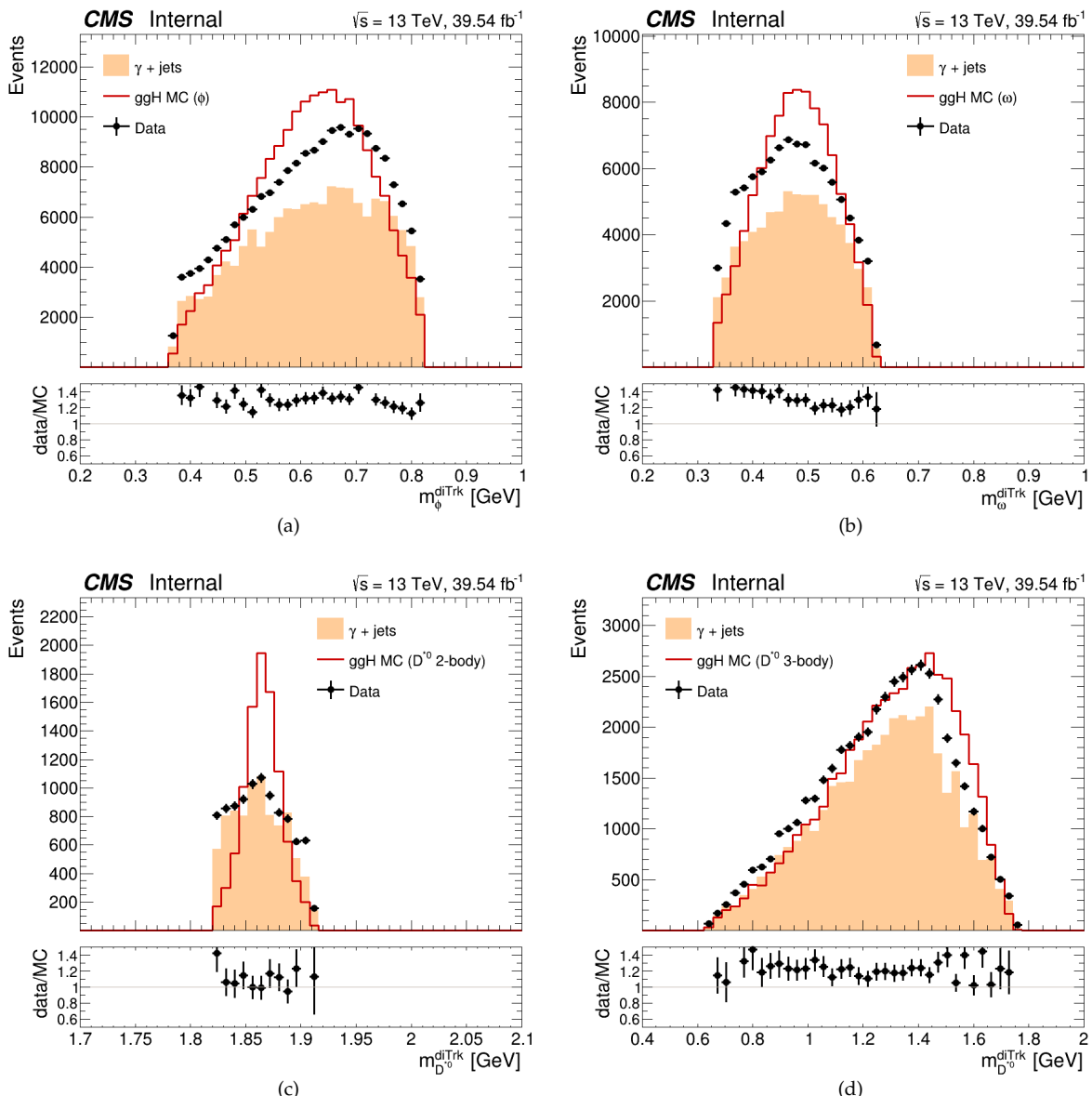
flow. It can be observed that the high-level trigger is less efficient for the  $D^{*0}$  decay mode compared to the other channels, resulting in a lower cumulative acceptance.

These strict cuts (selecting approximately only one in eleven signal events) will eliminate most of the background events, which for the ggH enriched channel, it dominantly consists of  $\gamma +$  multijet process, with a smaller contribution arising from QCD multijet. The 2-body  $D^{*0}$  decay is expected to have less background compared to the  $\phi$ ,  $\omega$  and 3-body  $D^{*0}$  decays, as in the 2-body case the very well-measured ditrack is a real resonance with a narrow width. Additionally, the  $\omega$  channel is expected to have also less background than the  $\phi$  and 3-body  $D^{*0}$  decays due to its sharper decay width.

## 3.6 MC-data comparison

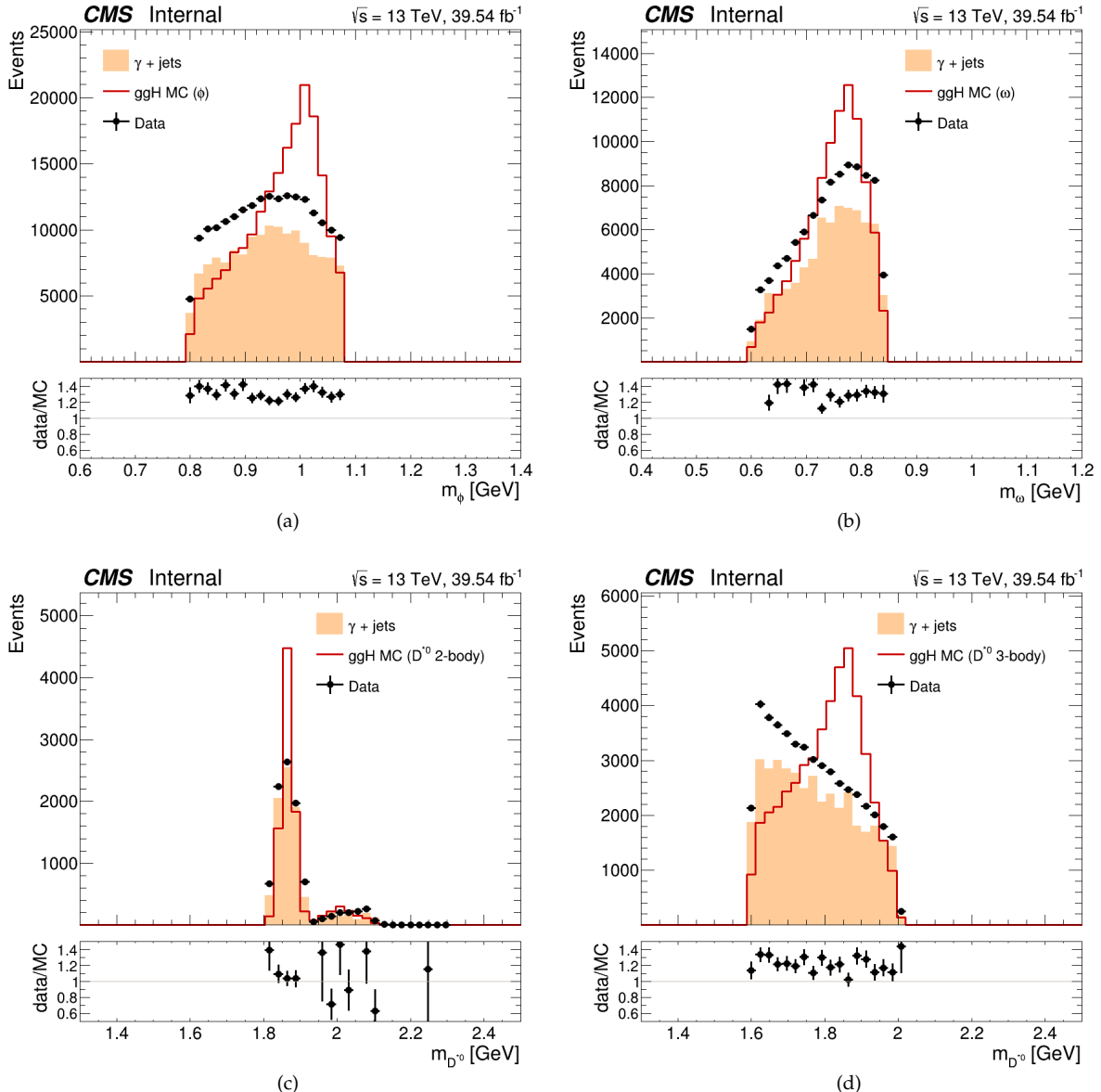
This section will provide a comparison between the signal MC, the background MC, and real data of the most important kinematic variables involved in these processes. The MC signal in all figures has been normalized to the same area as the data to improve the visualization. Each figure also provides the ratio between data and MC background, which consists of  $\gamma +$  jets. In all plots, the MC background underestimates the data as it only considers the dominant contribution (i.e.,  $\gamma +$  jets) at LO, and thus the number of background events from real data is a factor of around 30% larger than MC. This is not a concern, since the estimated limits are ultimately calculated using the data for the background fit. The MC background serves the purpose of helping us comprehend the behaviour of the involved processes.

Figure 20 displays the invariant mass of the ditrack system. For the  $\phi$ ,  $\omega$  and  $D^{*0}$  3-body decay channels, depicted in Figure 20 (a), (b), and (d), respectively, the ditrack mass is very wide, since the ditrack system does not form a real particle. In contrast, the ditrack mass for the  $D^{*0}$  2-body decay channel, shown in Figure 20 (c), exhibits a sharper resonance around 1.86 GeV. This is because in this case, the ditrack system is a real  $D^0$  meson. This distinctive feature will be exploited when modelling the signal. Moreover, it is seen that the MC background is consistent with the data across all decay modes.



**Figure 20:** Ditrack mass of the different studied decay modes. (a)  $\phi$  channel, (b)  $\omega$  channel, (c)  $D^{*0}$  2-body channel, and (d)  $D^{*0}$  3-body channel. The MC background is shown in orange, scatter points represent real data, and the signal, in red, is normalized to the data for better visualization.

Figure 21 displays the mass of the full meson. This variable is sharper than the ditrack system's mass in all channels because it consists of a real meson. However, for the  $D^{*0}$  2-body decay mode, it is not well reconstructed. Figure 21 (c) presents two peaks, one around 1.86



**Figure 21:** Full meson's mass of the different studied decay modes. (a)  $\phi$  channel, (b)  $\omega$  channel, (c)  $D^{*0}$  2-body channel, and (d)  $D^{*0}$  3-body channel. The MC background is shown in orange, scatter points represent real data, and the signal, in red, is normalized to the data for better visualization.

GeV, and another much more subtle around 2 GeV. This is because in approximately  $\sim 87\%$  of events, no photon compatible with the decay of a neutral particle is recovered, and therefore the computed full mass of the  $D^{*0}$  is the same as the ditrack system's mass. This is why this variable is not used in the BDT for regressing the transverse momentum (see Section 3.4). All other channels full meson mass, shown in Figures 21 (a), (b) and (d), consist of one sharp asymmetric peak. This asymmetric left shoulder is a sign of missing energy. It is worth noting that for the  $D^{*0}$  3-body decay mode, the peak of the full meson's mass is around

1.85 GeV instead of around the theoretical value of the  $D^{*0}$ 's mass, which is 2.007 GeV. The reason for this is that in most of the events, the recovered photons are from the decay of the more energetic  $\pi^0$  of the decay  $D^0 \rightarrow K^- \pi^+ \pi^0$ . Therefore, the full meson reconstructed mass resembles more the  $D^0$ 's mass rather than the  $D^{*0}$ 's mass. These singular peaks, that differ from the shape of the background, will also be exploited when modelling the signal, as done for the  $D^{*0}$  2-body decay mode with its ditrack mass. Additionally, the MC background is consistent with the data across all decay modes.

It is worth noting that the background and data also show subtle peaks in the same position as the signal for certain mass variables, as seen in Figure 20 (c) and Figure 21 (a) and (b). These peaks arise from real mesons present in the background, unrelated to the signal under study. In future analysis iterations, they could be accounted for by making the background model more complex, as explained in Section 3.9.

Figure 22 presents the transverse momentum of the primary photon originating directly from the Higgs boson decay. The signal peaks at around 60 GeV for all channels, which is roughly half of the Higgs boson's mass. This is consistent with Figure 23, which shows the transverse momentum of each meson. In every channel, the signal also peaks around 60 GeV, which with the transverse momentum of the photon adds up to the 125 GeV of the Higgs boson's mass. In these two figures, the MC background is compatible with the data across all decay modes.

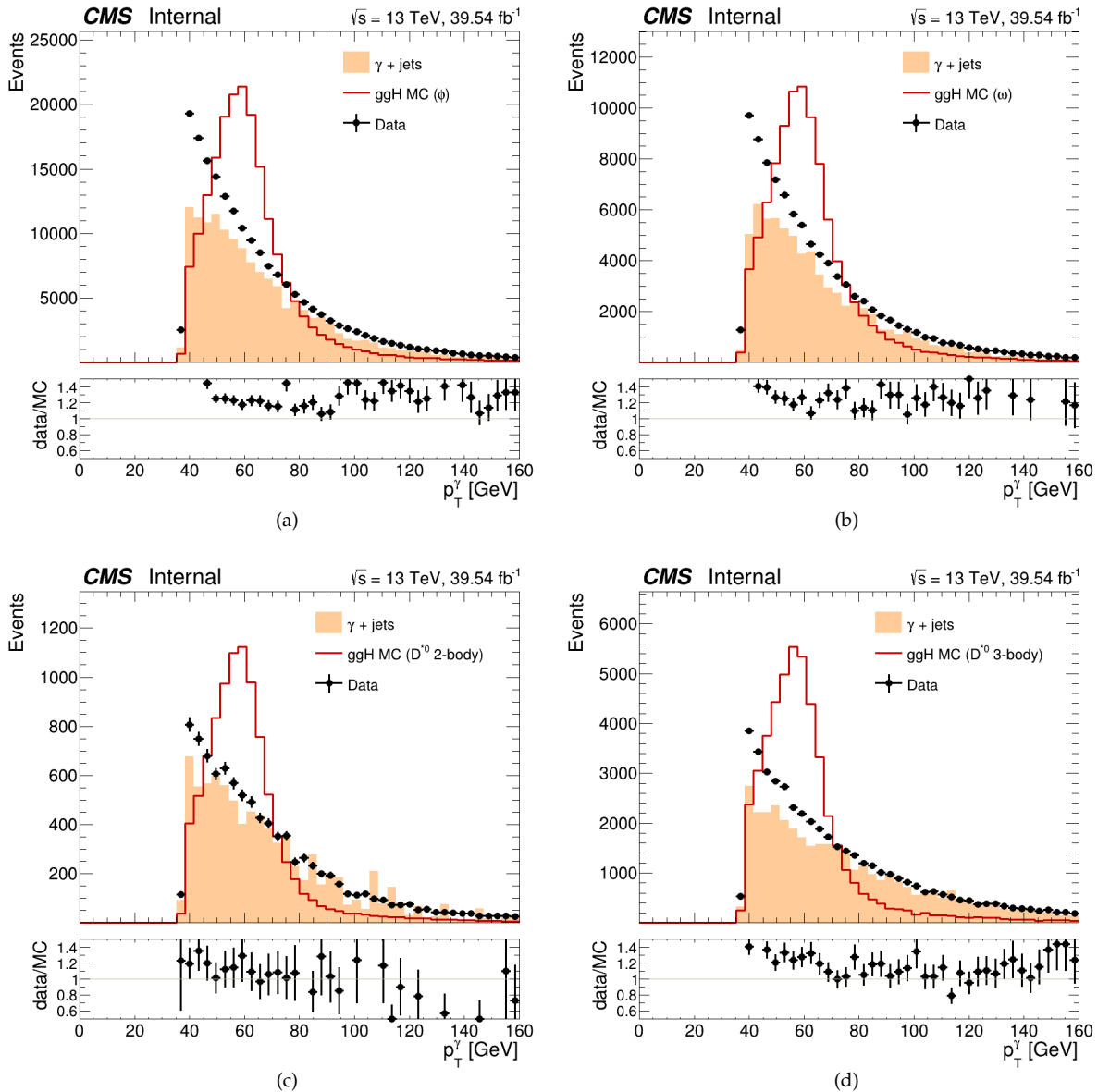


**Figure 22:** Transverse momentum  $p_T$  of the primary photon from the Higgs boson decay, for the different studied decay modes. (a)  $\phi$  channel, (b)  $\omega$  channel, (c)  $D^{*0}$  2-body channel, and (d)  $D^{*0}$  3-body channel. The MC background is shown in orange, scatter points represent real data, and the signal, in red, is normalized to the data for better visualization.

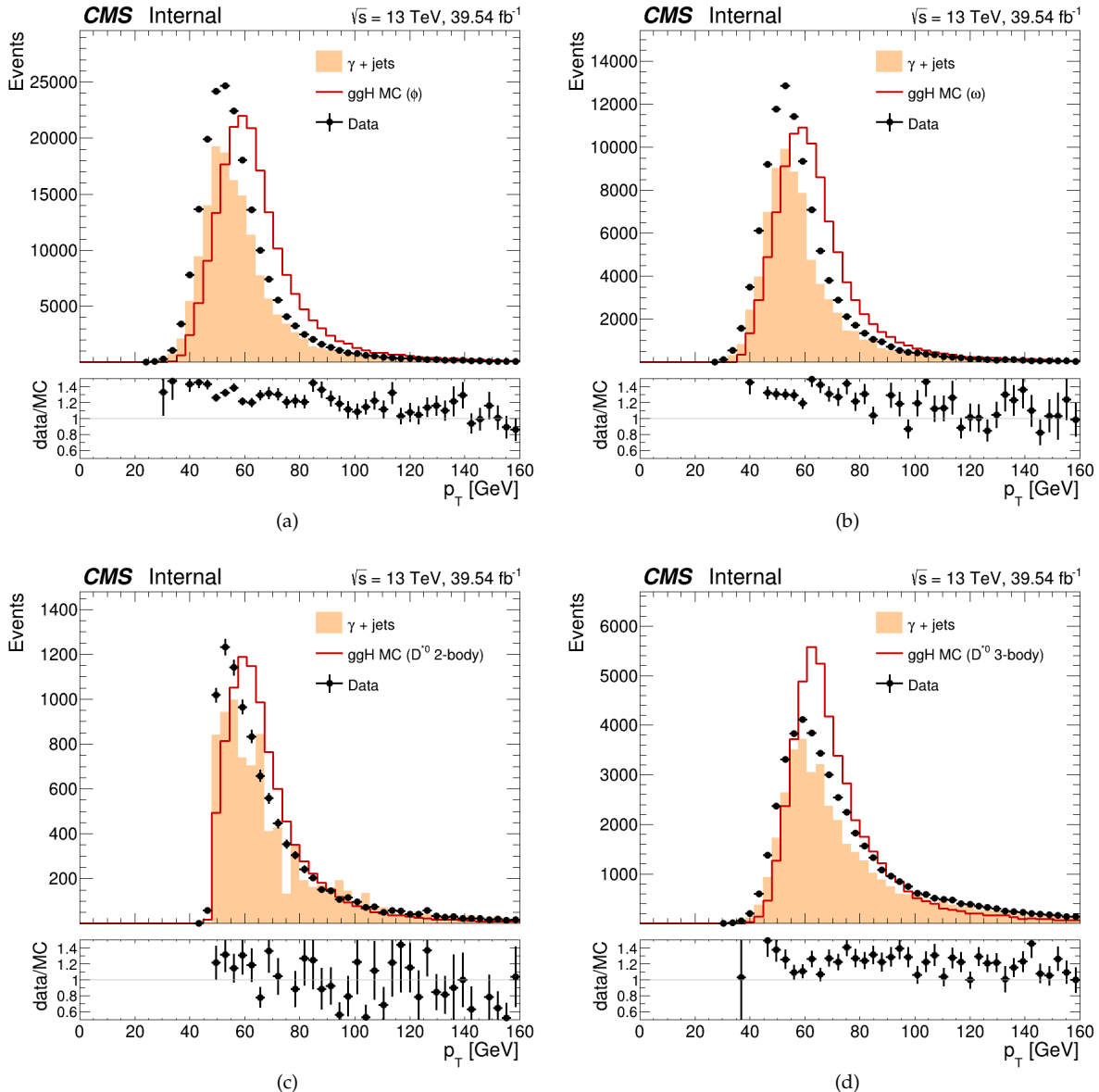


**Figure 23:** Transverse momentum  $p_T$  of the full meson for the different studied decay modes. (a)  $\phi$  channel, (b)  $\omega$  channel, (c)  $D^{*0}$  2-body channel, and (d)  $D^{*0}$  3-body channel. The MC background is shown in orange, scatter points represent real data, and the signal, in red, is normalized to the data for better visualization.

Figures 24 and 25 illustrate the transverse momentum of the charged leading and subleading tracks for each decay mode. All channels show a similar shape for the signal. However, it is worth noting that in the  $D^{*0}$  2-body decay, both the leading and subleading tracks are more energetic, as this is the only scenario where  $D^0$  decays into just two charged tracks (the neutral particle from  $D^{*0} \rightarrow D^0\pi^0/\gamma$  typically carries around  $\sim 5$  GeV in energy). As with all other figures in this section, the data-MC background comparison appears compatible across all decay modes.

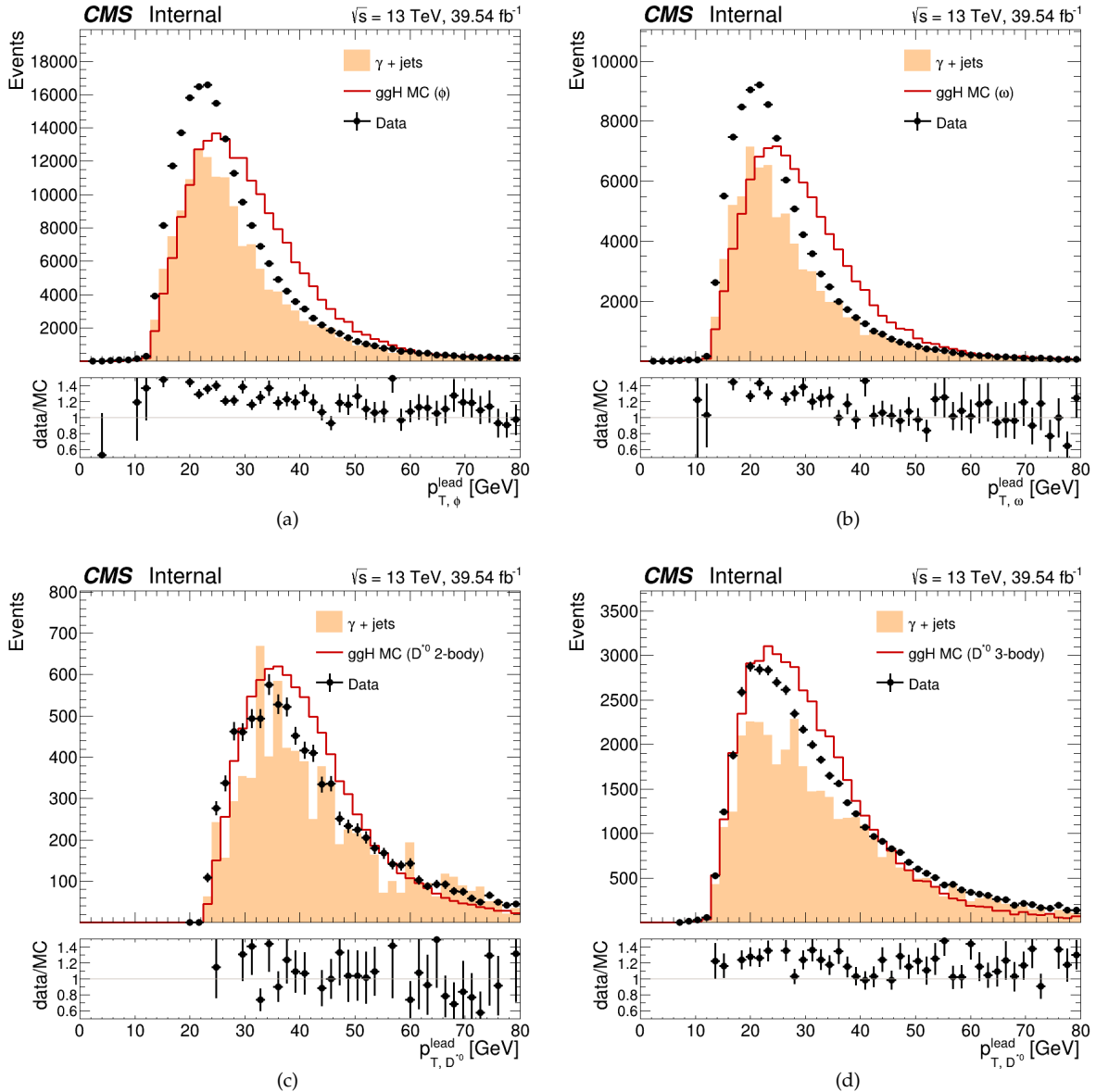


**Figure 24:** Transverse momentum  $p_T$  of the leading charged track for the different studied decay modes. (a)  $\phi$  channel, (b)  $\omega$  channel, (c)  $D^{*0}$  2-body channel, and (d)  $D^{*0}$  3-body channel. The MC background is shown in orange, scatter points represent real data, and the signal, in red, is normalized to the data for better visualization.

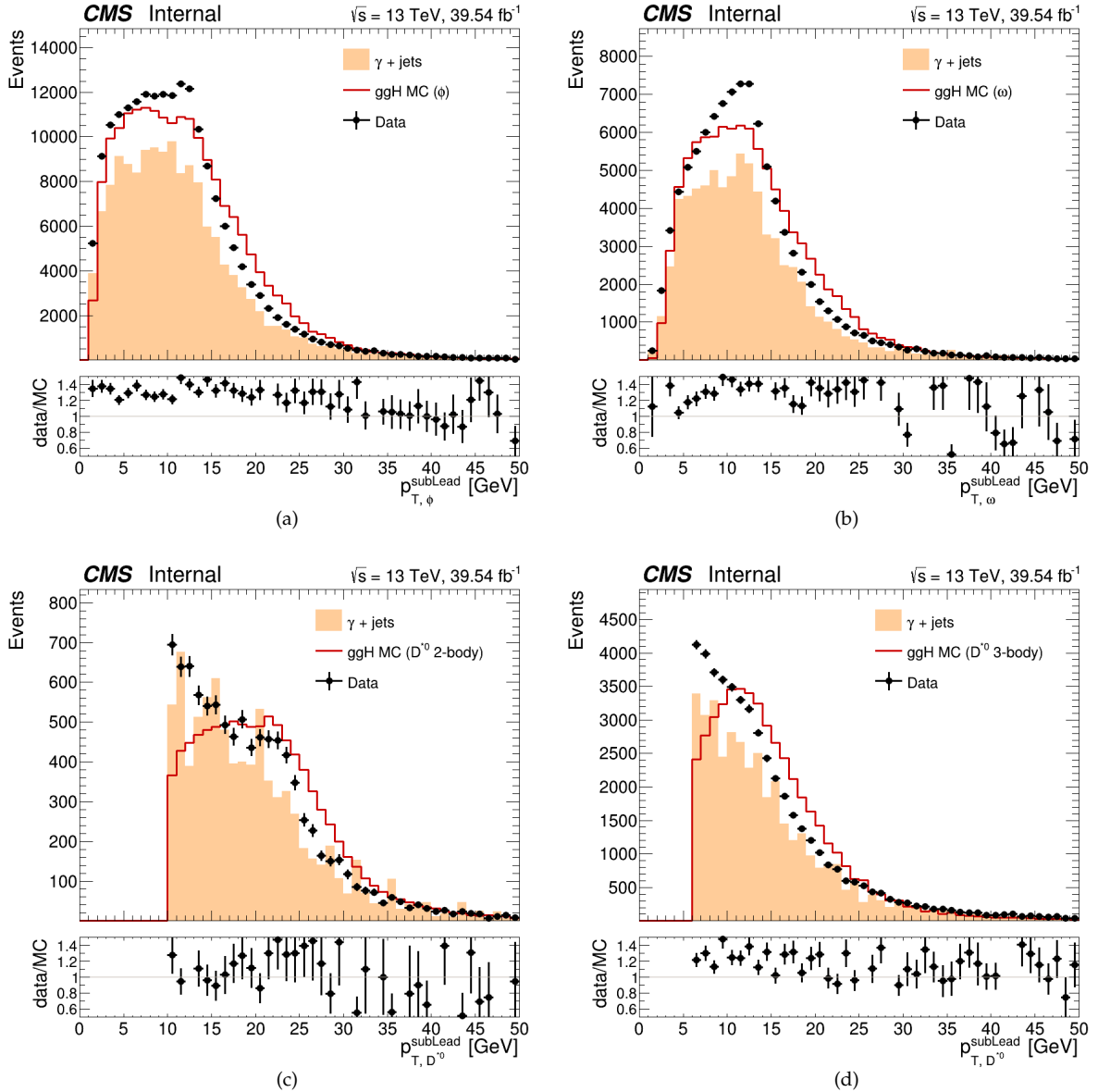


**Figure 25:** Transverse momentum  $p_T$  of the subleading charged track for the different studied decay modes. (a)  $\phi$  channel, (b)  $\omega$  channel, (c)  $D^{*0}$  2-body channel, and (d)  $D^{*0}$  3-body channel. The MC background is shown in orange, scatter points represent real data, and the signal, in red, is normalized to the data for better visualization.

### 3.7 Signal and background modelling

The first approach to extract the potential Higgs boson signal is done by fitting the invariant mass distribution  $m_{\gamma,M}^H$  for each decay mode separately, since the signal is expected to show a peak over a monotonous background. Both the signal and background are directly estimated from MC (signal) or data (background) by fitting the photon-meson invariant mass spectrum with analytical functions in the region  $100 < m_{\gamma,M}^H < 160$  GeV. The RooFit framework [89], a toolkit provided within the ROOT module for modelling the expected event distribution, is used for this purpose, and a binned maximum likelihood fit is conducted.

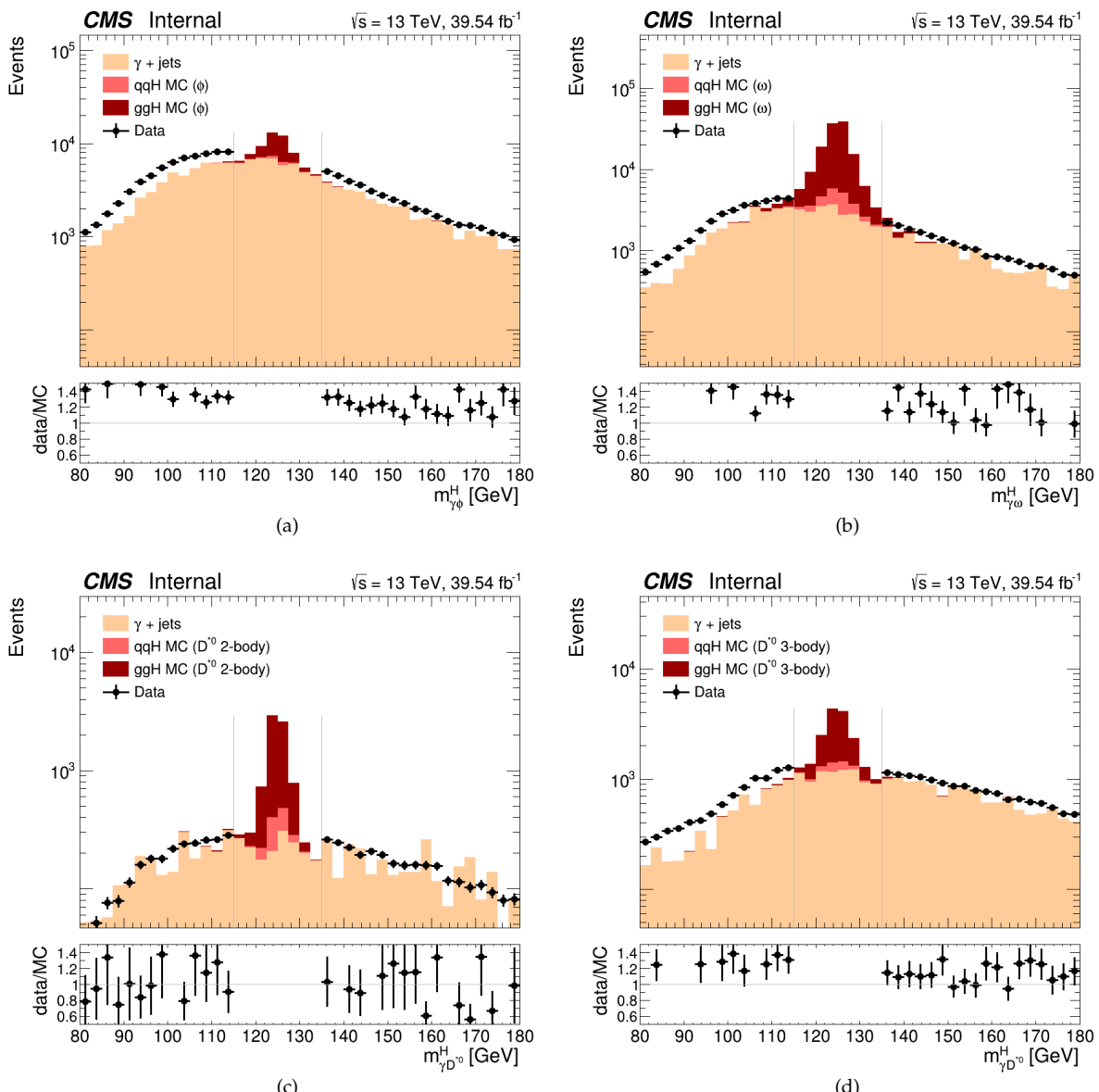


**Figure 26:** Higgs invariant mass distribution  $m_{\gamma,M}^H$  for the different studied decay modes. (a)  $\phi$  channel, (b)  $\omega$  channel, (c)  $D^{*0}$  2-body channel, and (d)  $D^{*0}$  3-body channel. The MC  $\gamma + \text{jets}$  background is shown in orange, scatter points represent real data, the ggH MC signal in crimson and the qqH MC signal in light coral. The total MC signal is scaled so that  $\mathcal{B}(H \rightarrow \phi\gamma)$ ,  $\mathcal{B}(H \rightarrow \omega\gamma)$  or  $\mathcal{B}(H \rightarrow D^{*0}\gamma)$  is set to 1 for better visualization. The data is blinded in the region of interest.

Figure 26 displays the photon-meson invariant mass distribution  $m_{\gamma,M}^H$  for each channel. The data in the region of interest is not shown, it is still *blinded*. Only after completing the full analysis and ensuring the consistency of the techniques used can the data be unblinded to enable actual measurements. This approach is commonly employed in high-energy physics to maintain an unbiased study.

Based on the earlier discussed selection criteria, the shape of the data and background exhibit a turn-on structure in  $m_{\gamma,M}^H$ . This turn-on varies for each decay mode due to the kinematic constraints of the events and the imposed selection cuts.

As shown in Figure 26, for all decay modes, the signal presents a sharp peak around the mass of the Higgs boson,  $m_H = 125$  GeV, while the background is either flat or monotonically decreasing. The primary contribution comes from ggH, but VBF (also denoted as qqH) shows a non-negligible contribution. By not focusing on a single production mode, events from both ggH and VBF are reconstructed, enhancing the signal-to-background ratio.

After performing this one-dimensional fit to  $m_{\gamma,M}^H$ , a two-dimensional fit has been considered. This 2D model simultaneously fits both the photon-meson invariant mass  $m_{\gamma,M}^H$  and the full meson mass  $m_M$ . In the case of the  $D^{*0}$  2-body decay mode, the ditrack mass  $m_M^{\text{diTrk}}$  is used instead of the full meson mass, due to the incomplete recovery of the latter. This strategy is the one ultimately adopted.

### 3.7.1 Signal modelling

Although previously discussed, it is worth emphasizing that the analysis sensitivity relies on the resolution of the photon-meson mass  $m_{\gamma,M}^H$ , which strongly depends on the kinematics, especially the transverse momentum of the photon and meson.

The first natural iteration of the two-dimensional fit is to consider the two variables as uncorrelated and independent. Under this assumption, the two-dimensional PDF becomes the product of two one-dimensional PDFs. Figure 27 shows the Higgs boson invariant mass for four different intervals of the meson mass for each decay mode. Each slice includes events where the recovered meson mass is within a certain interval, normalized to the same area. The values for the selected slices shown in Figure 27 are displayed in Table 18. In light red, the total photon-meson invariant mass is displayed. It can be observed that this approximation is reasonably good, particularly for the  $D^{*0}$  2-decay mode, given its precise mass reconstruction. For each channel, every slice has the same shape and the same maximum position, with only slight differences in width. To address this, in further iterations, one should either consider this as an uncertainty of the used model or account for this variation by modifying the 2D function, possibly by adding a correction factor. The 2D-PDF is then fitted to the MC signal, instead of doing two one-dimensional fits.

The expected photon-meson mass candidate distribution in signal events, for each decay mode, is modelled using a double-sided Crystal Ball. This function, named after the Crystal Ball Collaboration [87], is a probability density function (PDF) commonly employed in high-energy physics (HEP). It consists of a Gaussian centre and two asymmetric tails modelled by power-law functions, and it is  $C^1$ , i.e., continuous with a continuous derivative. This functional form simultaneously offers a robust description of the Higgs boson mass spectrum

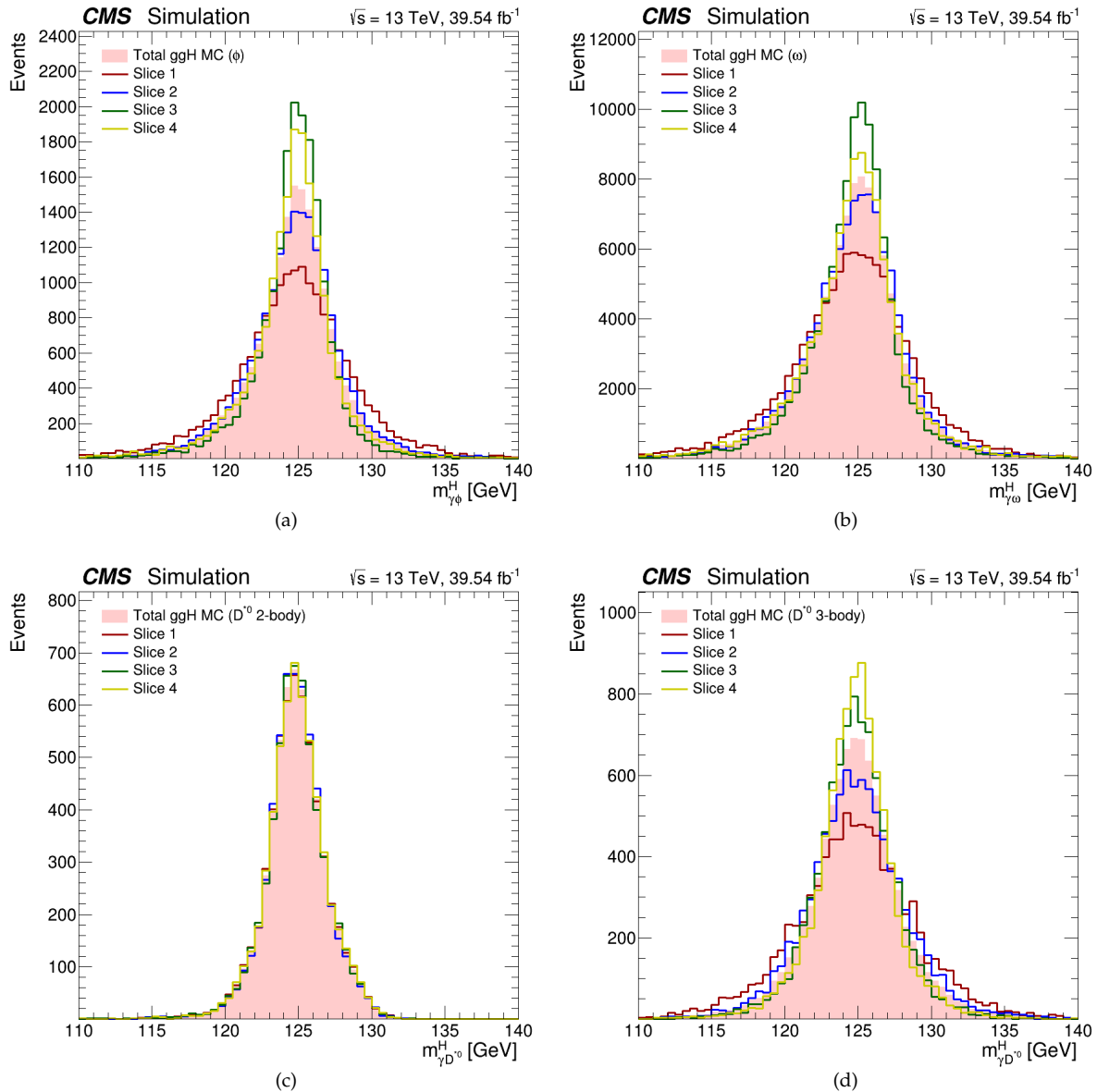


**Figure 27:** MC signal photon-meson invariant mass  $m_{\gamma M}^H$  for each decay channel, sliced for different meson mass intervals. (a)  $\phi$  channel, (b)  $\omega$  channel, (c)  $D^{*0}$  2-body channel, and (d)  $D^{*0}$  3-body channel. The values for the selected slices are displayed in Table 18. The total photon-meson invariant mass is displayed in light red.

| Decay channel   | Slice 1 (MeV) | Slice 2 (MeV) | Slice 3 (MeV) | Slice 4 (MeV) |
|-----------------|---------------|---------------|---------------|---------------|
| $\phi$          | [800, 920]    | [920, 990]    | [990, 1030]   | [1030, 1150]  |
| $\omega$        | [600, 720]    | [720, 760]    | [760, 800]    | [800, 900]    |
| $D^{*0}$ 2-body | [1805, 1854]  | [1854, 1865]  | [1865, 1876]  | [1876, 1925]  |
| $D^{*0}$ 3-body | [1500, 1710]  | [1710, 1800]  | [1800, 1870]  | [1870, 2100]  |

**Table 18:** Intervals selected to slice the mass of the meson, used in Figures 27 and 28.

and a straightforward way to incorporate shape uncertainties, as it has only one parameter associated with the peak and two with the width of the lineshape. The tails are necessary to account for the non-Gaussian response of the photons and meson. Further information about

this PDF and its implementation in ROOT is available in Ref. [88]. The full (ditrack) meson's mass is also modelled with a double-sided Crystal Ball for the same reasons.

### 3.7.2 Background modelling

The same independence assumption for the two variables has been applied to background modelling. Figure 28 displays the sliced Higgs invariant mass variables for the MC background for each decay channel. In this case, it is safe to conclude that the variables are entirely independent, and the assumption is well-founded.

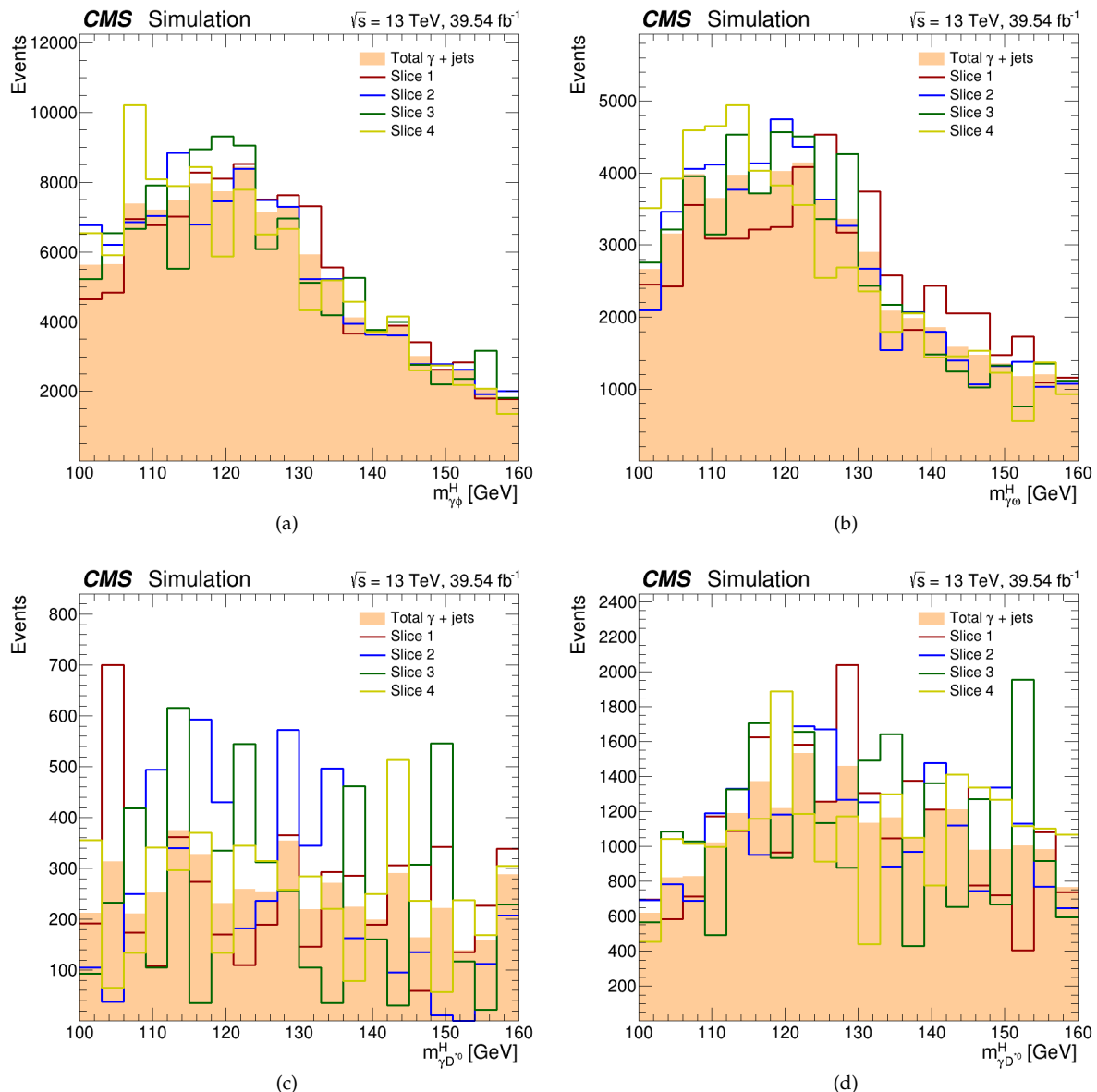


**Figure 28:** MC background photon-meson invariant mass  $m_{\gamma M}^H$  for each decay channel, sliced for different meson mass intervals. (a)  $\phi$  channel, (b)  $\omega$  channel, (c)  $D^{*0}$  2-body channel, and (d)  $D^{*0}$  3-body channel. The values for the selected slices are displayed in Table 18. The total photon-meson invariant mass is displayed in light orange.

The monotonous  $m_{\gamma,M}^H$  background distribution is estimated by fitting the photon-meson mass spectrum in the signal fit region ( $100 < m_{\gamma,M}^H < 160$  GeV) using analytic functions. Two sidebands,  $100 < m_{\gamma,M}^H < 115$  GeV and  $135 < m_{\gamma,M}^H < 160$  GeV, are used to constrain the background fit. Multiple functions are used to address the incomplete model knowledge. These will be part of the final fit to take into account the uncertainty in the background model choice and to estimate the bias from selecting a specific background parameterization. The same functions are also used to model the full (ditrack) meson's mass. The set of functions consists of degree 3 and 4 Bernstein and Chebyshev polynomials, resulting in four different combinations. [TODO: Add the gaussian pdf in the D02body background accounting for real mesons]

No prior knowledge of the parameters of the fit functions (in both shape and normalization) is assumed, i.e. they are allowed to vary freely in the data fit. Table 19 reports the degrees of the used polynomials, as well as the  $\chi^2/\text{dof}$  for each decay mode and for both polynomial classes and variable modelled (integrated over the other variable). Polynomials that are of third (fourth) degree have four (five) degrees of freedom (dof). It is worth noting

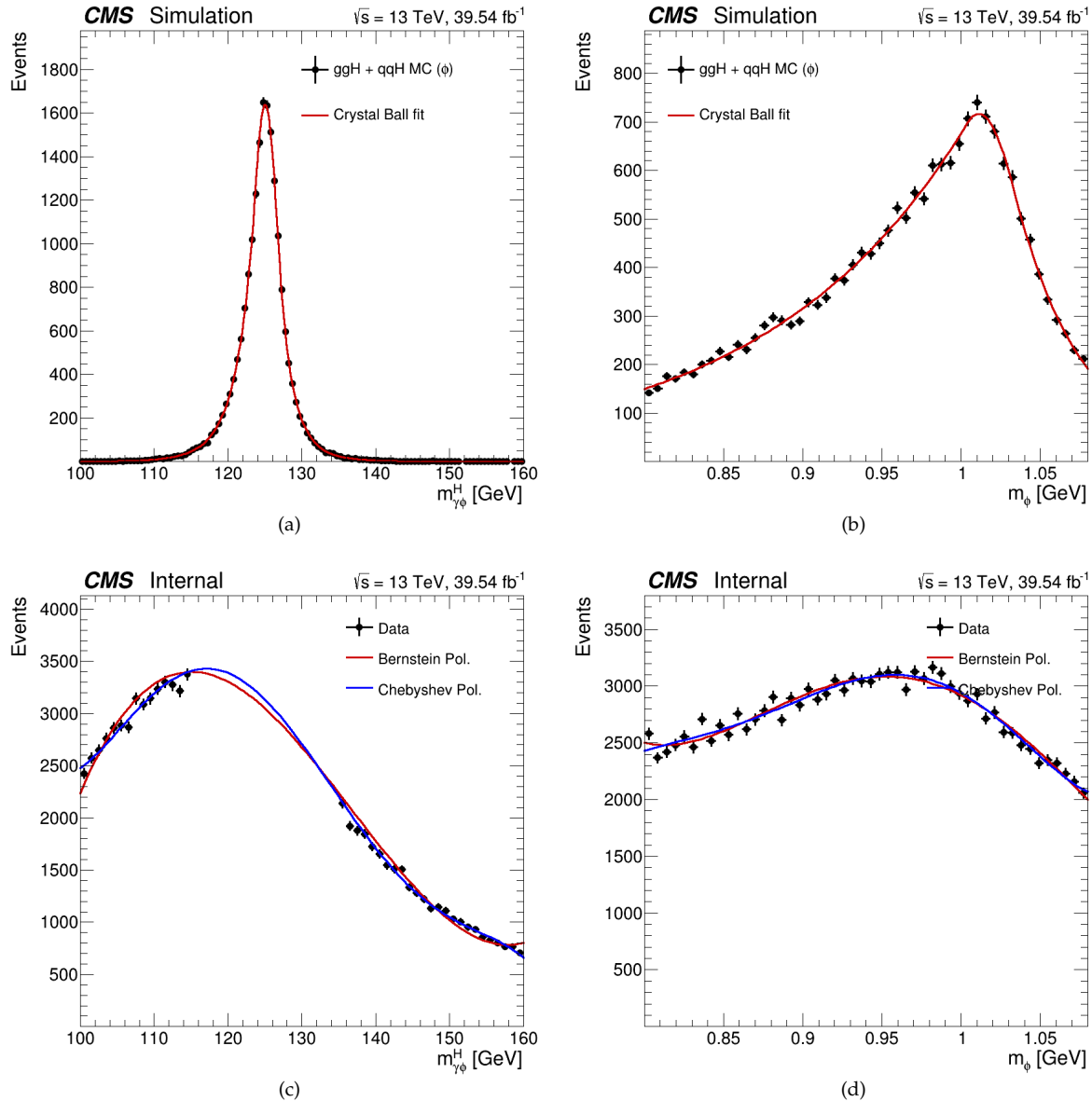
| Decay mode      | Bernstein ( $m_{\gamma,M}^H$ ) |                     | Chebyshev ( $m_{\gamma,M}^H$ ) |                     | Bernstein ( $m_M$ ) |                     | Chebyshev ( $m_M$ ) |                     |
|-----------------|--------------------------------|---------------------|--------------------------------|---------------------|---------------------|---------------------|---------------------|---------------------|
|                 | dof                            | $\chi^2/\text{dof}$ | dof                            | $\chi^2/\text{dof}$ | dof                 | $\chi^2/\text{dof}$ | dof                 | $\chi^2/\text{dof}$ |
| $\phi$          | 5                              | 5.31                | 5                              | 1.84                | 5                   | 2.56                | 5                   | 2.54                |
| $\omega$        | 5                              | 6.21                | 5                              | 2.13                | 5                   | 4.11                | 5                   | 3.68                |
| $D^{*0}$ 2-body | 4                              | 1.06                | 4                              | 0.95                | 6                   | 0.95                | 6                   | 0.92                |
| $D^{*0}$ 3-body | 4                              | 1.19                | 4                              | 1.07                | 4                   | 1.41                | 4                   | 1.37                |

**Table 19:** Degrees of the used polynomials and quality of the background fit in terms of  $\chi^2/\text{dof}$  for each decay mode and polynomial type used for each of the two variables modelled ( $m_{\gamma,M}^H$  and  $m_M$ ). When reporting the  $\chi^2/\text{dof}$  of a polynomial used to model a variable, the other has been integrated out.

that, for instance, a model Bernstein-Bernstein and a model Bernstein-Chebyshev (where the first polynomial models  $m_{\gamma,M}^H$  and the second models  $m_M$ ) have the same  $\chi^2/\text{dof}$  for the first variable since integrating out the second variable projects the model to one dimension.

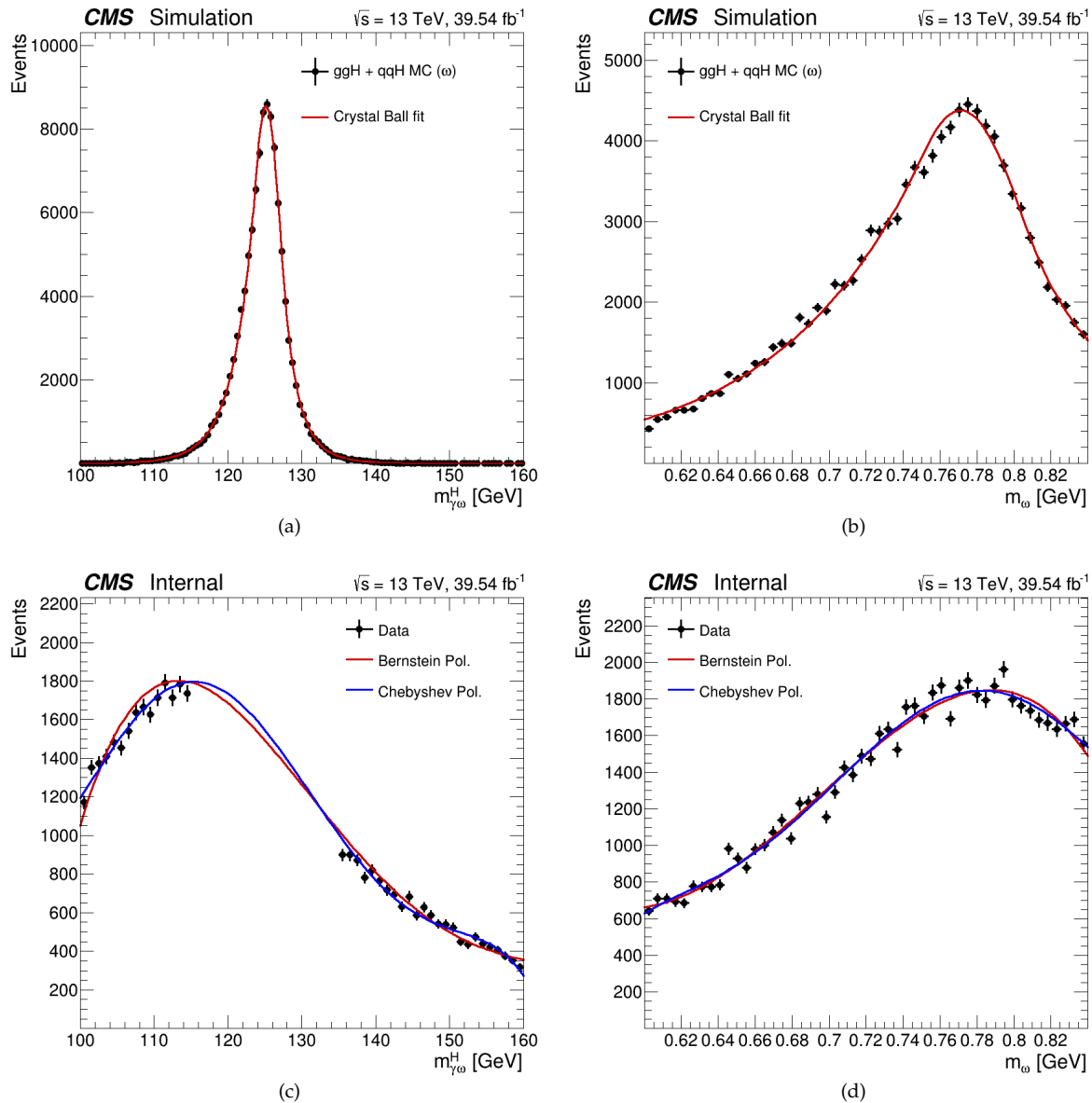
Figures 29, 30, 31 and 32 show the invariant photon-meson mass  $m_{\gamma,M}^H$  and the meson mass  $m_M$ , for both MC signal and data (for the background estimation) for each channel, with the projection of the fitted models. The data is blinded in the region  $115 < m_{\gamma,M}^H < 135$  GeV for the Higgs boson invariant mass in all decays. All background subfigures show the projection of the two fitted polynomials. Recall that the signal is scaled so that  $\mathcal{B}(H \rightarrow \phi\gamma) = \mathcal{B}(H \rightarrow \omega\gamma) = \mathcal{B}(H \rightarrow D^{*0}\gamma) = 1$ .

Figure 29 displays the models used for the  $\phi$  decay channel. Figures 29 (a) and (b) exhibit pronounced peaks for the signal, and the Crystal Ball fit effectively describes both kinematic variables. Additionally, the polynomials used to fit the background accurately model the data. Figures 29 (b) and (d) clearly motivate the two-dimensional fit, as the difference in behaviour between signal and background will contribute to enhance signal extraction.



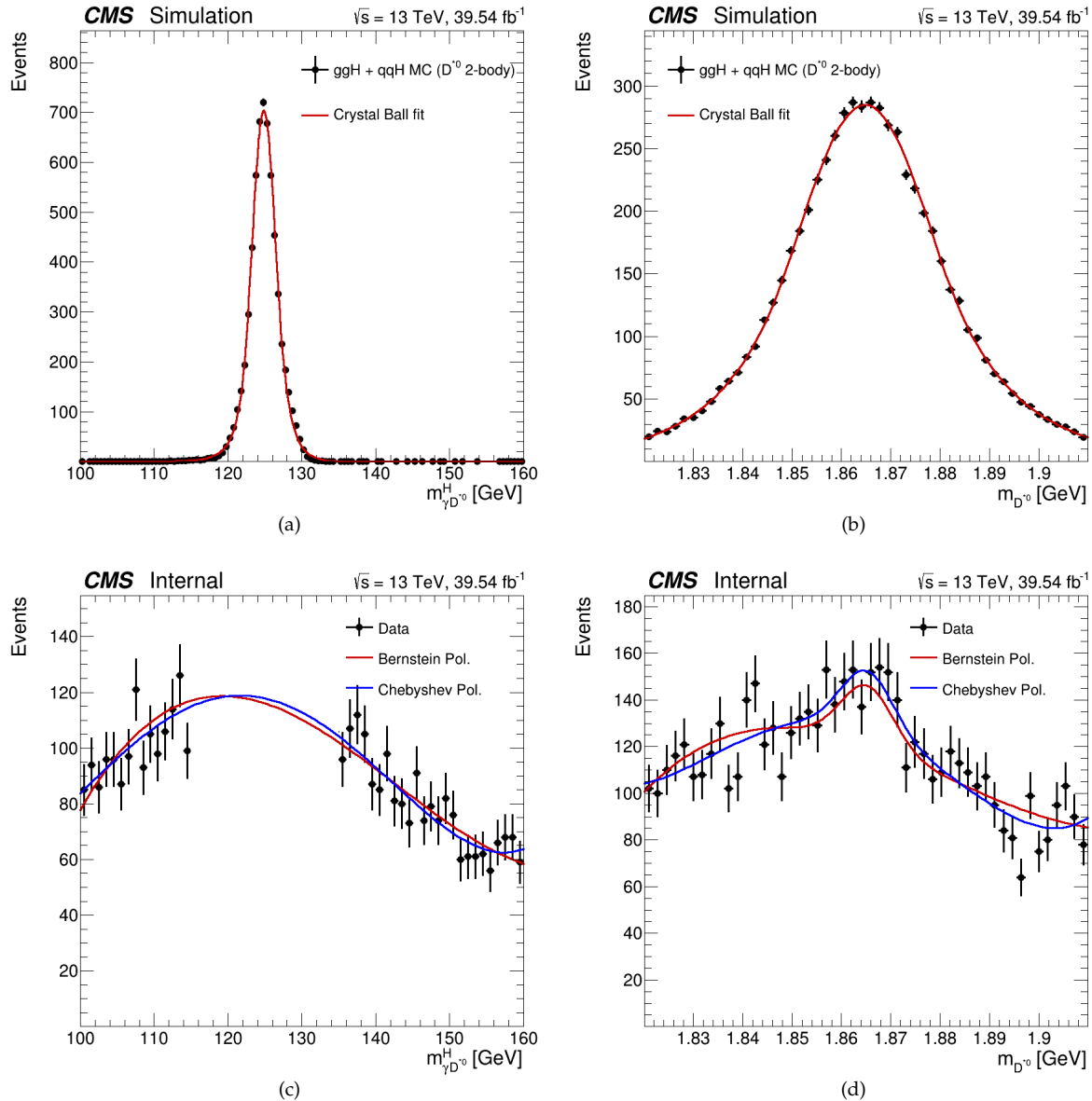
**Figure 29:** Signal and background fit projections for the  $\phi$  decay channel. (a) signal,  $m_{\gamma\phi}^H$  projection, (b) signal,  $m_\phi$  projection, (c) background,  $m_{\gamma\phi}^H$  projection, (d) background,  $m_\phi$  projection. The data is blinded in the region of interest.

A similar situation occurs with the  $\omega$  decay mode, as seen in Figure 30. Both Figure 30 (a) and (b) display distinct peaks for the signal, and the Crystal Ball fit effectively models both kinematic variables. The polynomials used to model the background accurately fit the data, although the meson's mass polynomials could be improved. Figure 30 (d) presents a maximum around the real mass of the  $\omega$  meson,  $m_\omega = 783$  MeV [25], coming from real  $\omega$  mesons in the background. This will in turn make the improvement of the two-dimensional fit not as good as in the  $\phi$  decay channel, where the meson's mass distribution was flatter (see Figure 29 (d)).



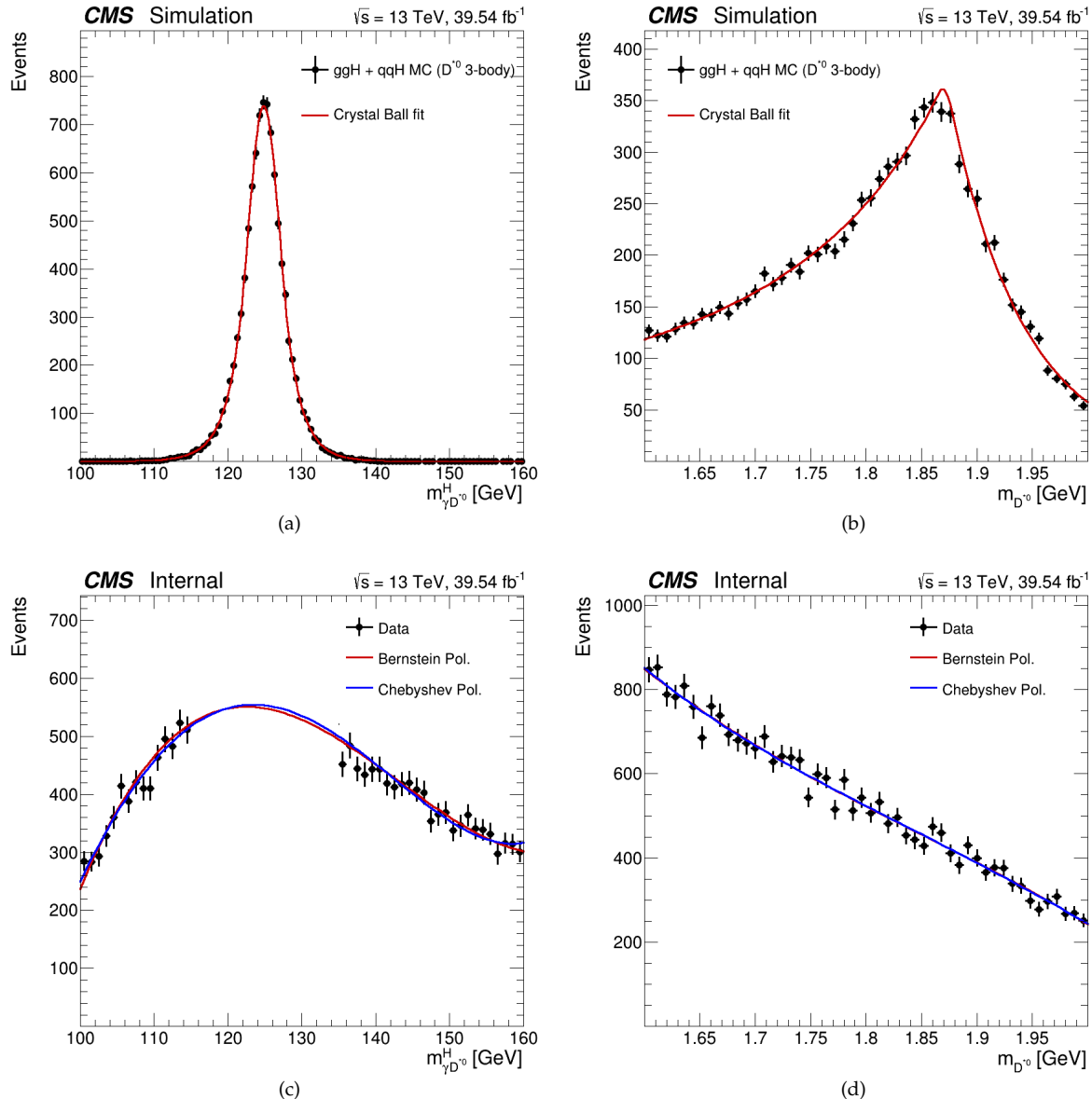
**Figure 30:** Signal and background fit projections for the  $\omega$  decay channel. (a) signal,  $m_{\gamma\omega}^H$  projection, (b) signal,  $m_\omega$  projection, (c) background,  $m_{\gamma\omega}^H$  projection, (d) background,  $m_\omega$  projection. The data is blinded in the region of interest.

Figure 31 shows the models used for the  $D^{*0}$  two-body decay channel. Figure 31 (a) presents the narrowest photon-meson invariant mass peak among all the studied decay modes, as it is the one with the best reconstructed transverse momentum (see Table 14). Additionally, the addition of the sharp ditrack's mass from the real  $D^0$  meson in the two-dimensional fit will enhance the final results significantly. The background polynomials for the photon-meson invariant mass appear to successfully model the data, in contrast to the meson's mass (Figures 31 (c) and (d)). The clear peak around the real mass of the  $D^0$ ,  $m_{D^0} = 1865$  MeV [25], in Figure 31 (d) comes from real  $D^0$  mesons in the background.



**Figure 31:** Signal and background fit projections for the  $D^{*0}$  2-body decay channel. (a) signal,  $m_{\gamma D^{*0}}^H$  projection, (b) signal,  $m_{D^{*0}}$  projection, (c) background,  $m_{\gamma D^{*0}}^H$  projection, (d) background,  $m_{D^{*0}}$  projection. The data is blinded in the region of interest.

Finally, Figure 32 displays the models used for the  $D^{*0}$  three-body decay channel. Both Crystal Ball functions fitted to  $m_{\gamma D^{*0}}^H$  and  $m_{D^{*0}}$  correctly describe the signal, as shown in Figures 32 (a) and (b). Furthermore, the background polynomials accurately model both kinematic variables depicted in Figures 32 (c) and (d). The falling, almost linear behaviour of the  $m_{D^{*0}}$  distribution in Figure 32 (d) will provide an important improvement to the final result compared to the one-dimensional fit.



**Figure 32:** Signal and background fit projections for the  $D^{*0}$  3-body decay channel. (a) signal,  $m_{\gamma D^{*0}}^H$  projection, (b) signal,  $m_{D^{*0}}$  projection, (c) background,  $m_{\gamma D^{*0}}^H$  projection, (d) background,  $m_{D^{*0}}$  projection. The data is blinded in the region of interest.

## 3.8 Estimated results

The upper limit is computed by performing a statistical test. Two hypotheses are defined: the null hypothesis  $H_0$  describes the model with signal plus background, while the alternative hypothesis  $H_1$  represents the background-only hypothesis. Maximum-likelihood 2D-fits to the photon-meson invariant mass  $m_{\gamma,M}^H$  and the meson mass  $m_M$  of the signal plus background MC (or to the data, after unblinding) are done for both hypotheses. The upper limit is then defined as the value of the branching fraction at which we can reject the alternative hypothesis with a certain  $p$ -value. The modified frequentist construction  $CL_s$  [90, 91] is used with the asymptotic approximation [92] to compute 95% confidence level (CL) upper limits on the branching fractions. The statistic  $CL_s$  is determined from the ratio

$$CL_s = \frac{p_0}{1 - p_1},$$

where  $p_0$  and  $p_1$  are the  $p$ -values of the signal-plus-background and background-only hypotheses, respectively [25]. For this computation, the Combine tool is employed with the `AsymptoticLimits` method [93].

The shape of the signal model is determined beforehand, as explained in Section 3.7, and in this new combined fit, only the normalization constant is allowed to vary. Intuitively, the value of the limit is related to the area under the fitted curves, making it approximately inversely proportional to the significance,  $S/\sqrt{S+B}$ , where  $S$  and  $B$  are the areas under the signal and background modelled curves, respectively. Additional information can be found in Ref. [92].

Table 20 reports the expected upper limits on the branching ratios for each studied decay mode. There are several points worth mentioning when comparing the obtained results to

| Decay channel                       | Expected $\mathcal{B}$ | ATLAS $\mathcal{B}$  | SM $\mathcal{B}$                 |
|-------------------------------------|------------------------|----------------------|----------------------------------|
| $H \rightarrow \phi\gamma$          | $2.40 \times 10^{-2}$  | $4.2 \times 10^{-4}$ | $(2.31 \pm 0.11) \times 10^{-6}$ |
| $H \rightarrow \omega\gamma$        | $3.27 \times 10^{-3}$  | $3.0 \times 10^{-4}$ | $(1.48 \pm 0.08) \times 10^{-6}$ |
| $H \rightarrow D^{*0}\gamma$ 2-body | $6.50 \times 10^{-3}$  | -                    | -                                |
| $H \rightarrow D^{*0}\gamma$ 3-body | $1.29 \times 10^{-2}$  | -                    | -                                |

**Table 20:** The expected upper limit on the branching fractions for the four studied decay channels is shown in the first column. The second column presents the corresponding expected upper limits measured by the ATLAS collaboration, when available [17, 18]. The third column displays the Standard Model predictions of the branching fractions, when available [43].

existent measurements by the ATLAS collaboration.

As mentioned previously, it is important to note that the results obtained are preliminary estimates, not actual measurements, which should be conducted after unblinding. This analysis serves as an initial approach, and many optimization techniques can and must be used in the future to enhance these results. Some of them are addressed in the following section.

For the  $H \rightarrow \phi\gamma$  decay, for which an estimated result of  $\mathcal{B}(H \rightarrow \phi\gamma) < 2.40 \times 10^{-2}$  at 95% CL was obtained, the further three-body decay  $\phi \rightarrow \pi^+\pi^-\pi^0$  was used. The presence of a neutral pion here is differential, as it makes the reconstruction of the  $\phi$  meson more

challenging than in the two-body decay  $\phi \rightarrow K^+K^-$ , thus worsening the resolution of photon-meson invariant mass  $m_{\gamma,\phi}^H$ .

The upper limit on the  $H \rightarrow \phi\gamma$  decay by the ATLAS collaboration used the subsequent two-body decay  $\phi \rightarrow K^+K^-$  [17], with a branching ratio of  $49.1 \pm 0.5\%$ , more than three times larger than the three-body decay  $\phi \rightarrow \pi^+\pi^-\pi^0$ , which is  $15.4 \pm 0.4\%$  [25]. Integrated luminosities are similar, with  $35.6 \text{ fb}^{-1}$  for ATLAS and  $39.54 \text{ fb}^{-1}$  in this analysis. Therefore, the differences in both results mainly lie in the meson decay mode used. Utilizing a meson decay with a higher branching fraction and the absence of neutral particles results in a better upper limit. This three-body decay mode is useful as it can be combined with existing results, like the ones in Ref. [17], to further constrain the total branching fraction upper limits.

For the  $H \rightarrow \omega\gamma$  decay, for which an estimated result of  $\mathcal{B}(H \rightarrow \phi\gamma) < 3.27 \times 10^{-3}$  at 95% CL was obtained, the further three-body decay  $\phi \rightarrow \pi^+\pi^-\pi^0$  was studied. The upper limit on the  $H \rightarrow \omega\gamma$  decay by the ATLAS collaboration also relied on the same subsequent three-body decay, reporting expected and measured upper limits of  $3.0 \times 10^{-4}$  and  $1.5 \times 10^{-4}$ , respectively [18]. However, the integrated luminosities available for both analyses differ significantly, with  $89.5 \text{ fb}^{-1}$  for ATLAS and  $39.54 \text{ fb}^{-1}$  in this analysis. The disparity in both results lies on the difference in available luminosities, and could be reduced optimizing the used techniques, as discussed in Section 3.9.

For the  $H \rightarrow D^{*0}\gamma$  decays, two different subsequent  $D^{*0}$  meson decays were explored. Although the analysis explicitly targets only  $H \rightarrow D^{*0}\gamma$ , the charge conjugate is implicit, as the analysis is entirely symmetric under charge conjugation. Therefore, accounting for both  $D^{*0}$  and  $\bar{D}^{*0}$  implies reconstructing twice the number of signal and background events. Since the upper limit is approximately inversely proportional to the significance, including the  $\bar{D}^{*0}$  decay introduces a factor of  $\frac{1}{\sqrt{2}}$  to the final result. Note that this is only valid under SM assumptions and for the expected upper limits, as for the actual measurement no prior SM assumptions must be made.

For the  $H \rightarrow D^{*0}\gamma$  decay with subsequent meson decays  $D^{*0} \rightarrow D^0\pi^0/\gamma$  and  $D^0 \rightarrow K^-\pi^+$ , an estimated result of  $\mathcal{B}(H \rightarrow D^{*0}\gamma) < 6.50 \times 10^{-3}$  at 95% CL was obtained. For the other channel, the  $H \rightarrow D^{*0}\gamma$  decay with subsequent meson decays  $D^{*0} \rightarrow D^0\pi^0/\gamma$  and  $D^0 \rightarrow K^-\pi^+\pi^0$  an estimated result of  $\mathcal{B}(H \rightarrow D^{*0}\gamma) < 1.29 \times 10^{-2}$  at 95% CL was obtained.

It is worth emphasizing that, even though  $\mathcal{B}(D^0 \rightarrow K^-\pi^+\pi^0) = 14.4 \pm 0.5\%$  is over three times greater than  $\mathcal{B}(D^0 \rightarrow K^-\pi^+) = 3.947 \pm 0.030\%$  [25], the upper limit obtained in the first case is higher. This is because in the two-body subsequent decay, although less frequent, it consists only of a ditrack charged system, which can be reconstructed with a better resolution. This, in turn, allows for more background event rejection, thus enhancing the final result.

Table 21 compares the expected upper limit on the branching fractions for the four studied decay channels, using a one or two-dimensional fit. In all decay modes, the expected upper limit is improved using the two-dimensional fit by around 20%.

| Decay channel                       | $\mathcal{B}$ with 1D fit | $\mathcal{B}$ with 2D fit    |
|-------------------------------------|---------------------------|------------------------------|
| $H \rightarrow \phi\gamma$          | $2.78 \times 10^{-2}$     | $2.40 \times 10^{-2}$ (-14%) |
| $H \rightarrow \omega\gamma$        | $3.55 \times 10^{-3}$     | $3.27 \times 10^{-3}$ (-8%)  |
| $H \rightarrow D^{*0}\gamma$ 2-body | $7.82 \times 10^{-3}$     | $6.50 \times 10^{-3}$ (-17%) |
| $H \rightarrow D^{*0}\gamma$ 3-body | $1.53 \times 10^{-2}$     | $1.29 \times 10^{-2}$ (-16%) |

**Table 21:** The expected upper limit on the branching fractions for the four studied decay channels using the 1D fit is shown in the first column. The second column shows the final results using the 2D fit, along with the improvement compared to the 1D fit.

## 3.9 Future potential improvements

This analysis provides an initial estimation of the upper limits on the branching ratios of the selected Higgs boson rare decays. Before unblinding and obtaining actual measurements, several improvements, corrections, and cross-checks are necessary. This section will briefly address some of these, although the list is not exhaustive.

**Multivariate analysis signal/background discriminant:** The most important discriminating variable between signal and background processes in this search is the photon-meson invariant mass, which forms a sharp peak around 125 GeV for the signal, as opposed to the background in which it decreases monotonically within the same mass range. Nonetheless, additional kinematic variables can enhance the signal-to-background separation.

To improve the sensitivity, a multivariate discriminant (using BDTs, for example) can be constructed, taking as input several variables that capture the distinct kinematic characteristics of both the signal and the background. To better isolate the Higgs boson signal from the SM background, MVA discriminants should be individually trained for each decay mode.

These MVA discriminants have shown to improve the exclusion limits by around 44% - 49% in similar analyses, like the one the CMS collaboration is currently conducting on similar Higgs rare decays.

**Additional Higgs boson production modes:** The Higgs boson is produced through various processes, as discussed in Section 1.2.2. This analysis does not target any specific production mode of the Higgs boson, and thus works with the dominant channels, which are ggH and VBF. However, it may be interesting to explicitly and exclusively study other production channels such as VBF, WH, ZH, or even associated production with heavy quarks. While some of these channels may be more pure than ggH due to the presence of leptons (that might help reduce background contamination), they would be less restrictive in the upper limit of the branching fraction due to lower cross sections. A non-trivial combination of results from all production modes could further reduce the branching fraction's upper limit.

**Study both  $D^{*0}$  and  $\overline{D}^{*0}$  decay channels separately:** Before unblinding, it is necessary to categorize  $H \rightarrow D^{*0}\gamma$  and  $H \rightarrow \overline{D}^{*0}\gamma$  exclusively. Analysing both samples separately may increase the signal acceptance and enhance the final results. Furthermore, no Standard Model assumptions should be made, as there might be asymmetries in the conjugate decay not previously expected.

**Polarization of the meson:** Pythia generates the samples with no polarization, assuming a flat distribution of the meson’s polarization. In reality, mesons are produced with a certain transverse polarization, resulting in some helicities being preferred over others. This leads to a correlation between the transverse polarization of the meson candidate and the daughter’s helicity. These discrepancies can be addressed by either generating the samples correctly at generation-level with Pythia or by reweighting the events to account for these relationships. This may ultimately increase the signal acceptance.

**Improve meson candidate reconstruction:** As mentioned earlier, the quality of the result strongly depends on the resolution of the photon-meson invariant mass  $m_{\gamma,M}^H$ , which, in turn, relies mainly on the accuracy of the transverse momenta of both particles. Since  $\gamma_H$  already undergoes a reconstruction algorithm developed by CMS (as discussed in Section 3.3.2), the efforts should focus on improving the meson reconstruction efficiency. This analysis has used BDTs, but exploring other machine learning techniques may further enhance the reconstructed meson’s transverse momentum.

Additionally, accurately reconstructing neutral particles will, in turn, improve the resolution of the meson’s  $p_T$ . When reconstructing the neutral particles, certain photons collimated with the ditrack system are considered (see Section 3.4.4). These photons, which typically carry very low momentum, are difficult to detect. This could be improved using their conversion to  $e^+e^-$  pairs in the silicon tracker, as demonstrated in [94]. This technique is already applied by default to the photons originating from the Higgs boson decay  $\gamma_H$ . Additionally, an mvaID like the one applied in the reconstruction of  $\gamma_H$  could also be developed.

**Data - MC corrections:** Simulated signal and background samples should be adjusted for various effects to closely match real data. Some corrections have already been applied in this analysis — scaling and resolution corrections for the photon originating from the Higgs boson decay  $\gamma_H$  —, but additional corrections should be considered. These include trigger, pileup, meson identification and neutral meson correction factors. This is relevant because the signal is used in the final fit estimation, while the background MC can be used to train the previously mentioned MVA discriminant.

**Improve background models:** Figures 29 (d), 30 (d), and 31 (d) show subtle peaks in the same position as the signal, arising from real mesons present in the background. In fact, the background consists of two contributions: on the one hand, there are purely combinatorial pairs of ditracks that coincidentally form the meson’s mass, and on the other hand, there are real mesons being detected. A more complex model would involve the sum of two analytical functions to account for both contributions: one polynomial for the combinatorial and one Gaussian-like function to model the real mesons.

**Bias study of the background polynomials:** The potential bias arising from the background parametrization choice can be estimated by fitting alternative functions to the  $m_{\gamma,M}^H$  sidebands and analysing the differences between them. The resulting uncertainties from this study must be included as systematic uncertainties.

**Systematics:** Every analysis must consider uncertainties, such as those arising from incomplete knowledge of the models or experimental resolutions. In this analysis, the true

model of the QCD background is unknown, representing one of the main sources of systematic uncertainties. Additionally, the low number of background events in the signal regions implies that a small fluctuation can lead to a significant variation in the upper limit computation. Both of these aspects need to be accounted for.

There are also theoretical and experimental uncertainties related to the signal. The theoretical uncertainties include the QCD scale and PDF variations (which can be taken from Ref. [24]). Experimental uncertainties, on the other hand, may include photon energy scale, jet energy scale, tracking efficiency, luminosity uncertainty and pileup uncertainty, among others.

# Conclusions

A search for the exclusive decays of the Higgs boson to a photon and either a  $\phi(1020)$ ,  $\omega(782)$  or  $D^*(2007)^0$  meson, with subsequent decays into a charged pair and neutral particles, has been presented. These decays have been suggested as a probe of the Higgs boson couplings to light quarks and as a test of potential deviations from the Standard Model prediction in these flavour interactions. The four decay channels explored are:  $H \rightarrow \phi\gamma$  with further  $\phi \rightarrow \pi^+\pi^-\pi^0$ ,  $H \rightarrow \omega\gamma$  with further  $\omega \rightarrow \pi^+\pi^-\pi^0$ ,  $H \rightarrow D^{*0}\gamma$  with further  $D^{*0} \rightarrow D^0\pi^0/\gamma$ ,  $D^0 \rightarrow K^-\pi^+$  and  $H \rightarrow D^{*0}\gamma$  with further  $D^{*0} \rightarrow D^0\pi^0/\gamma$ ,  $D^0 \rightarrow K^-\pi^+\pi^0$ . The analysis is performed with a pp collision data sample corresponding to an integrated luminosity of 39.54  $\text{fb}^{-1}$  collected at  $\sqrt{s} = 13$  TeV with the CMS detector at the LHC in 2018 during Run 2. The background model is derived using a fully data driven approach, and thus is MC independent.

The final expected upper limits on the branching ratio of the studied decays are reported in Table 20, and are:

$$\begin{aligned}\mathcal{B}(H \rightarrow \phi\gamma) &< 2.40 \times 10^{-2} \\ \mathcal{B}(H \rightarrow \omega\gamma) &< 3.27 \times 10^{-3} \\ \mathcal{B}(H \rightarrow D^{*0}\gamma) &< 6.50 \times 10^{-3} \\ \mathcal{B}(H \rightarrow D^{*0}\gamma) &< 1.29 \times 10^{-2}\end{aligned}$$

where the first  $H \rightarrow D^{*0}\gamma$  corresponds to the channel where  $D^{*0} \rightarrow D^0\pi^0/\gamma$ ,  $D^0 \rightarrow K^-\pi^+$ .

The first upper limit relies on a different meson decay mode than the one used in Ref. [17]. Combining both channels will further constrain this upper bound. Conversely, upper limits on the decay mode  $H \rightarrow D^{*0}\gamma$  have never been computed before. This initial approach can be improved and optimized to further constrain the branching ratio of this decay.

This analysis has applied new approaches in the context of these searches. These include the Boosted Decision Tree regression for the transverse momentum of each meson, as well as other techniques attempted to reconstruct the  $\pi^0$ . Additionally, the two-dimensional fit has proved to significantly reduce the limit, thereby opening the door to more applications in similar studies.

# Appendix

## BDT regression models

In Section 3.4 the Boosted Decision Trees used to improve the reconstruction of each full meson’s transverse momentum were introduced. The hyperparameters for these models are shown in Table 22, for each channel.

| Hyperparameter       | $\phi$    | $\omega$  | $D^{*0}$ 2-body | $D^{*0}$ 3-body |
|----------------------|-----------|-----------|-----------------|-----------------|
| VarTransform         | G, N, P   | G, P, D   | D, G            | -               |
| NTrees               | 1300      | 1500      | 1500            | 2200            |
| BoostType            | Grad      | Grad      | Grad            | Grad            |
| Shrinkage            | 0.055     | 0.095     | 0.043           | 0.094           |
| MaxDepth             | 5         | 4         | 7               | 5               |
| nCuts                | 35        | 37        | 28              | 36              |
| UseRandomisedTrees   | False     | True      | False           | False           |
| UseNvars             | 73        | 23        | 55              | 64              |
| UseBaggedBoost       | False     | True      | False           | True            |
| BaggedSampleFraction | 1.056     | 1.080     | 1.365           | 1.414           |
| PruneMethod          | NoPruning | NoPruning | ExpectedError   | NoPruning       |
| PruneStrength        | -         | -         | 17              | -               |
| PruningValFraction   | -         | -         | 0.705           | -               |

**Table 22:** Hyperparameters of the BDTs regressing the transverse momentum of each meson. These parameters are available options for the TMVA::Types::kBDT regressor. Each option is described in detail in Ref. [85].

# References

- [1] D.H. Perkins, “*Introduction to High Energy Physics*”, Addison-Wesley, Reading, USA (1982).
- [2] M.E. Peskin and D.V. Schroeder, “*An Introduction to Quantum Field Theory*”, Westview Press, Reading, USA (1995).
- [3] M.D. Schwartz, “*Quantum Field Theory and the Standard Model*”, Cambridge University Press (3, 2014).
- [4] S.L. Glashow, “*Partial Symmetries of Weak Interactions*”, *Nucl. Phys.* **22** (1961) 579.
- [5] A. Salam and J.C. Ward, “*Electromagnetic and weak interactions*”, *Phys. Lett.* **13** (1964) 168.
- [6] S. Weinberg, “*A Model of Leptons*”, *Phys. Rev. Lett.* **19** (1967) 1264.
- [7] P.W. Higgs, “*Broken Symmetries and the Masses of Gauge Bosons*”, *Phys. Rev. Lett.* **13** (1964) 508.
- [8] F. Englert and R. Brout, “*Broken Symmetry and the Mass of Gauge Vector Mesons*”, *Phys. Rev. Lett.* **13** (1964) 321.
- [9] G.S. Guralnik, C.R. Hagen and T.W.B. Kibble, “*Global Conservation Laws and Massless Particles*”, *Phys. Rev. Lett.* **13** (1964) 585.
- [10] UA1 collaboration, “*Experimental Observation of Isolated Large Transverse Energy Electrons with Associated Missing Energy at  $\sqrt{s} = 540 \text{ GeV}$* ”, *Phys. Lett. B* **122** (1983) 103.
- [11] UA2 collaboration, “*Observation of Single Isolated Electrons of High Transverse Momentum in Events with Missing Transverse Energy at the CERN anti- $p\ p$  Collider*”, *Phys. Lett. B* **122** (1983) 476.
- [12] CMS collaboration, “*Observation of a New Boson at a Mass of 125 GeV with the CMS Experiment at the LHC*”, *Phys. Lett. B* **716** (2012) 30 [[1207.7235](#)].
- [13] ATLAS collaboration, “*Observation of a new particle in the search for the Standard Model Higgs boson with the ATLAS detector at the LHC*”, *Phys. Lett. B* **716** (2012) 1 [[1207.7214](#)].
- [14] CMS collaboration, “*A portrait of the Higgs boson by the CMS experiment ten years after the discovery*”, *Nature* **607** (2022) 60 [[2207.00043](#)].

- [15] ATLAS collaboration, “*Searches for exclusive Higgs and Z boson decays into a vector quarkonium state and a photon using  $139\text{ fb}^{-1}$  of ATLAS  $\sqrt{s} = 13\text{ TeV}$  proton–proton collision data*”, *Eur. Phys. J. C* **83** (2023) 781 [[2208.03122](#)].
- [16] CMS collaboration, “*Search for rare decays of Z and Higgs bosons to  $J/\psi$  and a photon in proton-proton collisions at  $\sqrt{s} = 13\text{ TeV}$* ”, *Eur. Phys. J. C* **79** (2019) 94 [[1810.10056](#)].
- [17] ATLAS collaboration, “*Search for exclusive Higgs and Z boson decays to  $\phi\gamma$  and  $\rho\gamma$  with the ATLAS detector*”, *JHEP* **07** (2018) 127 [[1712.02758](#)].
- [18] ATLAS collaboration, “*Search for exclusive Higgs and Z boson decays to  $\omega\gamma$  and Higgs boson decays to  $K^*\gamma$  with the ATLAS detector*”, (2023) [[2301.09938](#)].
- [19] CMS collaboration, “*Search for Higgs boson decays into Z and  $J/\psi$  and for Higgs and Z boson decays into  $J/\psi$  or Y pairs in pp collisions at  $s=13\text{ TeV}$* ”, *Phys. Lett. B* **842** (2023) 137534 [[2206.03525](#)].
- [20] CMS collaboration, “*Search for decays of the 125 GeV Higgs boson into a Z boson and a  $\rho$  or  $\phi$  meson*”, *JHEP* **11** (2020) 039 [[2007.05122](#)].
- [21] G. Gabrielse, “*The standard model’s greatest triumph*”, *Physics Today* **66** (2013) .
- [22] A. Wongel, “*Search for Heavy Resonances in Four-Top-Quark Final States in pp Collisions at  $\sqrt{s} = 13\text{ TeV}$  With the ATLAS Detector*”, Ph.D. thesis, Staats-und Universitätsbibliothek Hamburg Carl von Ossietzky, 2022.
- [23] A. Djouadi, “*The Anatomy of electro-weak symmetry breaking. I: The Higgs boson in the standard model*”, *Phys. Rept.* **457** (2008) 1 [[hep-ph/0503172](#)].
- [24] LHC HIGGS CROSS SECTION WORKING GROUP collaboration, “*Handbook of LHC Higgs Cross Sections: 4. Deciphering the Nature of the Higgs Sector*”, (2016) [[1610.07922](#)].
- [25] PARTICLE DATA GROUP collaboration, “*Review of Particle Physics*”, *PTEP* **2022** (2022) 083C01.
- [26] CMS collaboration, “*Observation of Higgs boson decay to bottom quarks*”, *Phys. Rev. Lett.* **121** (2018) 121801 [[1808.08242](#)].
- [27] CMS collaboration, “*Measurements of the Higgs boson production cross section and couplings in the W boson pair decay channel in proton-proton collisions at  $\sqrt{s} = 13\text{ TeV}$* ”, *Eur. Phys. J. C* **83** (2023) 667 [[2206.09466](#)].
- [28] CMS collaboration, “*Observation of the Higgs boson decay to a pair of  $\tau$  leptons with the CMS detector*”, *Phys. Lett. B* **779** (2018) 283 [[1708.00373](#)].
- [29] CMS collaboration, “*Search for Higgs Boson Decay to a Charm Quark-Antiquark Pair in Proton-Proton Collisions at  $s=13\text{ TeV}$* ”, *Phys. Rev. Lett.* **131** (2023) 061801 [[2205.05550](#)].
- [30] CMS collaboration, “*Measurements of Higgs boson production cross sections and couplings in the diphoton decay channel at  $\sqrt{s} = 13\text{ TeV}$* ”, *JHEP* **07** (2021) 027 [[2103.06956](#)].

- [31] CMS collaboration, “*Search for Higgs boson decays to a Z boson and a photon in proton-proton collisions at  $\sqrt{s} = 13$  TeV*”, *JHEP* **05** (2023) 233 [2204.12945].
- [32] CMS collaboration, “*Evidence for Higgs boson decay to a pair of muons*”, *JHEP* **01** (2021) 148 [2009.04363].
- [33] G.-y. Huang and S. Zhou, “*Precise Values of Running Quark and Lepton Masses in the Standard Model*”, *Phys. Rev. D* **103** (2021) 016010 [2009.04851].
- [34] ATLAS collaboration, “*Search for the Decay of the Higgs Boson to Charm Quarks with the ATLAS Experiment*”, *Phys. Rev. Lett.* **120** (2018) 211802 [1802.04329].
- [35] CMS collaboration, “*A search for the standard model Higgs boson decaying to charm quarks*”, *JHEP* **03** (2020) 131 [1912.01662].
- [36] ATLAS collaboration, “*Direct constraint on the Higgs-charm coupling from a search for Higgs boson decays into charm quarks with the ATLAS detector*”, *Eur. Phys. J. C* **82** (2022) 717 [2201.11428].
- [37] ATLAS collaboration, “*Search for the Higgs boson decays  $H \rightarrow ee$  and  $H \rightarrow e\mu$  in pp collisions at  $\sqrt{s} = 13$  TeV with the ATLAS detector*”, *Phys. Lett. B* **801** (2020) 135148 [1909.10235].
- [38] CMS collaboration, “*Search for the Higgs boson decay to a pair of electrons in proton-proton collisions at  $s=13$ TeV*”, *Phys. Lett. B* **846** (2023) 137783 [2208.00265].
- [39] CMS collaboration, “*Search for lepton-flavor violating decays of the Higgs boson in the  $\mu\tau$  and  $e\tau$  final states in proton-proton collisions at  $\sqrt{s} = 13$  TeV*”, *Phys. Rev. D* **104** (2021) 032013 [2105.03007].
- [40] CMS collaboration, “*Search for flavor-changing neutral current interactions of the top quark and the Higgs boson decaying to a bottom quark-antiquark pair at  $\sqrt{s} = 13$  TeV*”, *JHEP* **02** (2022) 169 [2112.09734].
- [41] A.L. Kagan, G. Perez, F. Petriello et al., “*Exclusive Window onto Higgs Yukawa Couplings*”, *Phys. Rev. Lett.* **114** (2015) 101802 [1406.1722].
- [42] G.T. Bodwin, H.S. Chung, J.-H. Ee et al., “*Addendum: New approach to the resummation of logarithms in Higgs-boson decays to a vector quarkonium plus a photon [Phys. Rev. D 95, 054018 (2017)]*”, *Phys. Rev. D* **96** (2017) 116014 [1710.09872].
- [43] M. König and M. Neubert, “*Exclusive Radiative Higgs Decays as Probes of Light-Quark Yukawa Couplings*”, *JHEP* **08** (2015) 012 [1505.03870].
- [44] J.I. Aranda, G. González-Estrada, J. Montaño et al., “*Revisiting the rare  $H \rightarrow q_i q_j$  decays in the standard model*”, *J. Phys. G* **47** (2020) 125001 [2009.07166].
- [45] FCC collaboration, “*FCC Physics Opportunities: Future Circular Collider Conceptual Design Report Volume 1*”, *Eur. Phys. J. C* **79** (2019) 474.
- [46] J. Ellis and T. You, “*Sensitivities of Prospective Future e+e- Colliders to Decoupled New Physics*”, *JHEP* **03** (2016) 089 [1510.04561].

- [47] D. d'Enterria, "Physics case of FCC-ee", *Frascati Phys. Ser.* **61** (2016) 17 [1601.06640].
- [48] FCC collaboration, "FCC-hh: The Hadron Collider: Future Circular Collider Conceptual Design Report Volume 3", *Eur. Phys. J. ST* **228** (2019) 755.
- [49] GARGAMELLE NEUTRINO collaboration, "Observation of Neutrino Like Interactions Without Muon Or Electron in the Gargamelle Neutrino Experiment", *Phys. Lett. B* **46** (1973) 138.
- [50] ALEPH collaboration, "Determination of the Number of Light Neutrino Species", *Phys. Lett. B* **231** (1989) 519.
- [51] NA48 collaboration, "A New measurement of direct CP violation in two pion decays of the neutral kaon", *Phys. Lett. B* **465** (1999) 335 [hep-ex/9909022].
- [52] L. Evans and P. Bryant, "LHC Machine", *JINST* **3** (2008) S08001.
- [53] CERN, "Facts and figures about the LHC", URL: <https://home.cern/resources/faqs/facts-and-figures-about-lhc>. Last accessed: October 10<sup>th</sup> 2023.
- [54] ATLAS collaboration, "ATLAS: Technical proposal for a general-purpose  $p\ p$  experiment at the Large Hadron Collider at CERN", (1994) Geneva: CERN, 1994. - 272p. URL: <https://cds.cern.ch/record/290968>.
- [55] CMS collaboration, "CMS, the Compact Muon Solenoid: Technical proposal", (1994) Geneva: CERN, 1994. - 254p. URL: <https://cds.cern.ch/record/290969>.
- [56] ALICE collaboration, "ALICE: Technical proposal for a large ion collider experiment at the CERN LHC", (1995) Geneva: CERN, 1995. - 237p. URL: <https://cds.cern.ch/record/293391>.
- [57] LHCb collaboration, "LHCb technical proposal: A Large Hadron Collider Beauty Experiment for Precision Measurements of CP Violation and Rare Decays", (1998) Geneva: CERN, 1998. - 170p. URL: <https://cds.cern.ch/record/622031>.
- [58] E. Mobs, "The CERN accelerator complex in 2019. Complexe des accélérateurs du CERN en 2019", URL: <https://cds.cern.ch/record/2684277>, 2019. General Photo.
- [59] CMS collaboration, "CMS Luminosity - Public Results", URL: <https://twiki.cern.ch/twiki/bin/view/CMSPublic/LumiPublicResults>, 2023. Last accessed: October 10<sup>th</sup> 2023.
- [60] CMS collaboration, "The CMS Experiment at the CERN LHC", *JINST* **3** (2008) S08004.
- [61] T. Sakuma and T. McCauley, "Detector and Event Visualization with SketchUp at the CMS Experiment", *J. Phys. Conf. Ser.* **513** (2014) 022032 [1311.4942].
- [62] CMS collaboration, G.L. Bayatian et al., "CMS Physics: Technical Design Report Volume 1: Detector Performance and Software", Technical design report. CMS, CERN, Geneva (2006).
- [63] D. Barney, "CMS Detector Slice", 2016. CMS Collection. URL: <https://cds.cern.ch/record/2120661>.

- [64] A. Buckley, C. White and M. White, “*Practical Collider Physics*”, IOP (12, 2021), 10.1088/978-0-7503-2444-1.
- [65] CERN, “The CERN Experimental Programme - CMS”, URL: <https://greybook.cern.ch/experiment/detail?id=CMS>. Last accessed: October 11<sup>th</sup> 2023.
- [66] ALEPH, CDF, D0, DELPHI, L3, OPAL, SLD, LEP ELECTROWEAK WORKING GROUP, TEVATRON ELECTROWEAK WORKING GROUP, SLD ELECTROWEAK, HEAVY FLAVOUR GROUPS collaboration, “*Precision Electroweak Measurements and Constraints on the Standard Model*”, (2010) [1012.2367].
- [67] LEP WORKING GROUP FOR HIGGS BOSON SEARCHES, ALEPH, DELPHI, L3, OPAL collaboration, “*Search for the standard model Higgs boson at LEP*”, *Phys. Lett. B* **565** (2003) 61 [hep-ex/0306033].
- [68] CERN collaboration, “*ROOT: Data Analysis Framework*”, URL: <https://root.cern/>, 2023. Last accessed: October 16<sup>th</sup> 2023.
- [69] CMS collaboration, “*The CMS NanoAOD data tier*”, URL: <https://twiki.cern.ch/twiki/bin/view/CMSPublic/WorkBookNanoAOD>, 2023. Last accessed: October 16<sup>th</sup> 2023.
- [70] J. Alwall, R. Frederix, S. Frixione et al., “*The automated computation of tree-level and next-to-leading order differential cross sections, and their matching to parton shower simulations*”, *JHEP* **07** (2014) 079 [1405.0301].
- [71] S. Alioli, P. Nason, C. Oleari et al., “*A general framework for implementing NLO calculations in shower Monte Carlo programs: the POWHEG BOX*”, *JHEP* **06** (2010) 043 [1002.2581].
- [72] T. Sjöstrand, S. Ask, J.R. Christiansen et al., “*An introduction to PYTHIA 8.2*”, *Comput. Phys. Commun.* **191** (2015) 159 [1410.3012].
- [73] NNPDF collaboration, “*Parton distributions from high-precision collider data*”, *Eur. Phys. J. C* **77** (2017) 663 [1706.00428].
- [74] CMS collaboration, “*Extraction and validation of a new set of CMS PYTHIA8 tunes from underlying-event measurements*”, *Eur. Phys. J. C* **80** (2020) 4 [1903.12179].
- [75] CMS collaboration, “*CMS track reconstruction performance during Run 2 and developments for Run 3*”, *PoS ICHEP2020* (2021) 733 [2012.07035].
- [76] CERN collaboration, “*Cross Section DB Tool (XSecDB)*”, URL: <https://xsdb-temp.app.cern.ch/>, 2023. Last accessed: October 16<sup>th</sup> 2023.
- [77] CMS collaboration, “*Measurement of differential cross sections for inclusive isolated-photon and photon+jets production in proton-proton collisions at  $\sqrt{s} = 13$  TeV*”, *Eur. Phys. J. C* **79** (2019) 20 [1807.00782].
- [78] K. Hamilton, P. Nason and G. Zanderighi, “*MINLO: Multi-Scale Improved NLO*”, *JHEP* **10** (2012) 155 [1206.3572].

- [79] D. Contardo, M. Klute, J. Mans et al., “*Technical Proposal for the Phase-II Upgrade of the CMS Detector*”, CERN, Geneva (2015), DOI.
- [80] CMS collaboration, “*Electron and photon reconstruction and identification with the CMS experiment at the CERN LHC*”, *JINST* **16** (2021) P05014 [2012.06888].
- [81] CMS collaboration, “*CMS Electron and Photon Performance at 13 TeV*”, *J. Phys. Conf. Ser.* **1162** (2019) 012008.
- [82] CMS collaboration, “*Description and performance of track and primary-vertex reconstruction with the CMS tracker*”, *JINST* **9** (2014) P10009 [1405.6569].
- [83] CMS collaboration, “*CMSSW on GitHub*”, URL: <https://cms-sw.github.io/>, 2023. Last accessed: October 18<sup>th</sup> 2023.
- [84] K. Prokofiev and T. Speer, “*A kinematic and a decay chain reconstruction library*”, in *14th International Conference on Computing in High-Energy and Nuclear Physics*, pp. 411–414, 2005, DOI.
- [85] A. Hoecker, P. Speckmayer, J. Stelzer et al., “*TMVA - Toolkit for Multivariate Data Analysis*”, (2007) [[physics/0703039](#)].
- [86] Y. Coadou, “*Boosted decision trees*”, (2022) [[2206.09645](#)].
- [87] A2 collaboration, “*A2 Detector System - Crystal Ball*”, URL: <https://www.a2.kph.uni-mainz.de/a2detector-system/crystal-ball/>, 2023. Last accessed: October 23<sup>rd</sup> 2023.
- [88] CERN collaboration, “*ROOT Reference Guide: RooCrystalBall Class Reference*”, URL: <https://root.cern/doc/master/classRooCrystalBall.html>, 2023. Last accessed: October 23<sup>rd</sup> 2023.
- [89] CERN collaboration, “*ROOT: RooFit*”, URL: <https://root.cern/manual/roofit/>, 2023. Last accessed: October 23<sup>rd</sup> 2023.
- [90] A.L. Read, “*Presentation of search results: The CL<sub>s</sub> technique*”, *J. Phys. G* **28** (2002) 2693.
- [91] T. Junk, “*Confidence level computation for combining searches with small statistics*”, *Nucl. Instrum. Meth. A* **434** (1999) 435 [[hep-ex/9902006](#)].
- [92] G. Cowan, K. Cranmer, E. Gross et al., “*Asymptotic formulae for likelihood-based tests of new physics*”, *Eur. Phys. J. C* **71** (2011) 1554 [[1007.1727](#)], [Erratum: *Eur.Phys.J.C* 73, 2501 (2013)].
- [93] CMS collaboration, “*Higgs Analysis - Combined Limit*”, URL: <https://cms-analysis.github.io/HiggsAnalysis-CombinedLimit/>, 2023. Last accessed: October 23<sup>rd</sup> 2023.
- [94] CMS collaboration, “*Observation of the  $\chi_{b1}(3P)$  and  $\chi_{b2}(3P)$  and measurement of their masses*”, *Phys. Rev. Lett.* **121** (2018) 092002 [[1805.11192](#)].